DEVELOPMENT OF CHLORIDE-FREE ELECTROLYTE FOR RECHARGEABLE MAGNESIUM BATTERY

RAYMOND HORIA

SCHOOL OF MATERIALS SCIENCE AND ENGINEERING

2022

DEVELOPMENT OF CHLORIDE-FREE ELECTROLYTE FOR RECHARGEABLE MAGNESIUM BATTERY

RAYMOND HORIA

SCHOOL OF MATERIALS SCIENCE AND ENGINEERING

A thesis submitted to the Nanyang Technological University
in partial fulfilment of the requirement for the degree of
Master of Engineering

2022

Statement of Originality

I hereby certify that the work embodied in this thesis is the result of original research, is free of plagiarised materials, and has not been submitted for a higher degree to any other University or Institution.

NTU NTU NTU NTU NTU NTU NTU

25 January 2022

. . . .
Date

. . . .
Raymond Horia

Supervisor Declaration Statement

I have reviewed the content and presentation style of this thesis and declare it is free of plagiarism and of sufficient grammatical clarity to be examined. To the best of my knowledge, the research and writing are those of the candidate except as acknowledged in the Author Attribution Statement. I confirm that the investigations were conducted in accord with the ethics policies and integrity standards of Nanyang Technological University and that the research data are presented honestly and without prejudice.

25 January 2022

. . . .

Date

Qingyu Yan

. . . .

Prof Alex Yan Qingyu

Authorship Attribution Statement

This thesis contains material from one paper published in the following peer-reviewed journal.

Chapter 5 is published as Horia, R.; Nguyen, D.-T.; Eng, A. Y. S.; Seh, Z. W., Using a Chloride-Free Magnesium Battery Electrolyte to Form a Robust Anode–Electrolyte Nanointerface. *Nano Lett.* **2021,** *21*, 8220-8228.

The contributions of the co-authors are as follows:

- Prof Seh Zhi Wei and Dr. Dan Thien Nguyen provided the initial project direction and edited the manuscript draft.
- I prepared the manuscript, performed the electrochemical measurements and data analysis.
- Post-mortem SEM analysis was conducted by me in the A*STAR FE-SEM JSM 6700F laboratory.
- Post-mortem EDS analysis was conducted by Dr. Alex Eng in the A*STAR FE-SEM JSM 7600F laboratory.
- Sulfur cathodes were synthesized and the sulfur content was analyzed with the help of Dr. Alex Eng.
- Dr. Dan Thien Nguyen conducted the Raman, XRD, and XPS measurements discussed in this report.
- Single Crystal X-ray Diffraction measurement and crystal structure determination were conducted by Dr. Li Yongxin of NTU Division of Chemistry and Biological Chemistry.

25 January 2022

. . . .
Date

. . . .
Raymond Horia

Abstract

A primary challenge in developing rechargeable magnesium battery electrolytes is to create a chloride-free electrolyte with a facile fabrication process. The chloride-based additive is generally added to conventional magnesium electrolytes to improve their compatibility with the magnesium anode. The additive, however, tends to induce corrosion on the current collector of the cathode. This side effect increases the parasitic reaction and cell degradation rate during the battery operation. Although several novel magnesium electrolytes have been reported to be compatible with the magnesium anode, even in a chloride-free electrolyte formulation, the mass scale production viability of these electrolytes is low. To create a chloride-free simple to produce electrolyte formulation, the thesis seeks to explore various combinations of commercially available magnesium salts, additives, and solvents. The report shows that by using the appropriate combination of non-passivating magnesium salt, moisture scavenging additive, and ether-based solvent, a chloride-free electrolyte with good compatibility with the magnesium metal anode can be created. The electrolyte was also found to have high anodic stability on stainless steel and was also found to be compatible with the copper sulfide cathode material at high temperature.

Lay Summary

One of the most prominent research fields on next-generation post-lithium-ion rechargeable batteries is the field of rechargeable magnesium batteries. The primary focus of the field is to implement magnesium metal as the negative electrode for novel rechargeable batteries. Magnesium metal anode is desirable due to its high natural abundance on the earth's crust, high volumetric charge capacity, and its low reduction potential. In other words, a rechargeable magnesium battery has the potential to achieve a high energy density and to be used for a high-demand purpose (for example as EV energy storage devices).

The primary focus of this thesis is to develop a new chloride-free rechargeable magnesium battery electrolyte with good stability at a high electric potential using commercial magnesium salt. Commercial-based substances are desirable electrolyte constituents as their production can be done on a large scale. Furthermore, the chloride-free approach is utilized in this research as chloride-based chemicals are known to corrode the battery components (especially during the battery charging process). However, removing chloride from the electrolyte comes with its challenge as the magnesium metal anode tends to become inactive due to a passivation effect of most chloride-free electrolytes. This thesis shows that a passivation-free magnesium electrolyte formulation made from a commercial magnesium salt ($Mg(HMDS)_2$) does not require a chloride additive. This formulation was further shown to have high anodic stability against stainless steel and aluminum. The electrolyte also does not induce corrosion on the surface of the electrode.

Acknowledgments

I would like to express my gratitude to the Institute of Materials Research and Engineering (IMRE), Agency for Science, Technology and Research (A*STAR), and National Research Foundation (NRF), for supporting me during these two years through a Research Scholarship (NRF-NRFF2017-04). My gratitude also goes to my supervisor and co-supervisor Prof Alex Yan Qingyu and Prof Seh Zhi Wei for their guidance during my graduate study. I am also grateful to Dr. Dan Thien Nguyen and Dr. Alex Eng, both of whom have guided me and helped me with my research.

Table of Contents

Table Captions

Figure Captions

Abbreviations

APC	All Phenyl Complex
BESS	Battery Energy Storage System
CE	Columbic Efficiency
DCC	Di-Chloro Complex
Diglyme	1-methoxy-2-(2-methoxyethoxy)ethane
EDS	Energy Dispersive X-ray Spectroscopy
EV	Electric Vehicle
LiB	Lithium-ion Battery
LSV	Linear Sweep Voltammetry
MACC	Magnesium Aluminum Chloride Complex
$Mg(Al(HFIP)_4)_2$	magnesium tetrakis-(2H-hexafluoroisopropyloxy) aluminate
MBA	magnesium bis-(diisopropylamide)
$Mg(B(HFIP)_4)_2$	magnesium tetrakis-(2H-hexafluoroisopropyl) borate
$Mg(B(PFPINA)_2)_2$	magnesium bis-(perflouropinacolato) borate
$Mg(HMDS)_2$	magnesium bis(hexamethyldisilazide)
DME	1,2-dimethoxyethane (or DME)
$Mg(OTF)_2$	magnesium trifluoromethanesulfonate
$Mg(TFSI)_2$	magnesium bis(trifluoromethanesulfonimide)
NMP	N-methyl-2-pyrrolidone
OMBB	Organic Magnesium Borate-Based electrolyte
PVDF	poly-vinylidene difluoride
SEI	Solid Electrolyte Interphase
SEM	Scanning Electron Microscope
S/MC	Sulfur in Microporous carbon composite
S-PAN	Sulfur-Polyacrylonitrile cathode
RE	Reference Electrode
RMB	Rechargeable Magnesium Battery
$TBABH_4$	tetrabutylammonium borohydride
Tetraglyme	bis(2-(2-methoxyethoxy)ethyl)ether
Triglyme	1,2-bis(2-methoxyethoxy)ethane

THF	tetrahydrofuran
THFPB	tris-(2H-hexafluoroisopropyl) borate
WE	Working Electrode
XRD	X-Ray Diffraction
SCXRD	Single Crystal X-Ray Diffraction

Chapter 1

Introduction

This chapter begins by outlining the current problem faced in the development of rechargeable magnesium battery electrolytes. Mainly, the issue involves the use of corrosive chloride which limits the potential window of the electrolyte. It then briefly describes the hypothesis of this research regarding the relationship between the electrolyte constituents and the electrolyte potential window. A brief description of the research objective and scope is then given, followed by a thorough overview of the thesis content. The chapter ends with a list of major research findings in this report.

1.1 Problem Statement

Currently, most of the Rechargeable magnesium battery (RMB) electrolytes that have been invented contains chloride constituent.[1] Due to the existence of this component, rechargeable magnesium battery electrolytes tend to be corrosive to non-noble current collectors.[2] Since high energy density magnesium battery typically requires a wide operating potential that can reach up to more than 3 V vs Mg,[3] the corrosion issue makes the creation of a high-energy-density battery more challenging as the cathode current collectors would degrade at such a high potential. While state-of-the-art chloride-free electrolytes with non-corrosive property, wide potential window, high plating/stripping Coulombic efficiency, and high ionic conductivity exist;[4-7] they are not commercially available and thus have questionable industrial production viability.

This thesis tests the hypothesis that a wide potential window electrolyte can be made by proper electrolyte constituents engineering (magnesium salt, additive, and solvent). An investigation was also conducted to ascertain if the anodic stability of the electrolyte can be maintained at a high potential by using a relatively small concentration of chloride-based additives. The results of this thesis indicate that prudent magnesium salt selection is crucial to achieving a highly reversible magnesium plating and stripping process. Furthermore, the additives' amount required in the electrolyte depends on the type of magnesium salt used in the electrolyte. A wide-potential window electrolyte, therefore, could be made by tuning the composition of the electrolyte. Evidence of corrosion in the chloride-containing (10 mM Cl^-) is also provided, further establishing the need to remove chloride from rechargeable magnesium batteries.

1.2 Objective and Scope

This thesis investigates various electrolyte formulations which can be made by a one-step dissolution process from commercial substances with (1) high magnesium plating and stripping Coulombic efficiency, (2) long cycle life, and (3) large potential window. The current target in this thesis is to achieve an electrolyte potential window of more than 2.6 V vs Mg on a stainless-steel or aluminum current collector, with a magnesium plating and stripping Coulombic efficiency of 99%. The magnesium cell should also be cyclable for about 1000 cycles.

The scope of the report includes:

1. Electrochemical characterizations of the electrolytes such as magnesium plating and stripping overpotential and Coulombic efficiency measurement, anodic stability measurement, electrolyte's ionic conductivity measurement, and full cell cycling.

2. Electrolyte electrochemical species investigations by Raman spectroscopy and single-crystal X-ray Diffraction spectroscopy of the crystal from the saturated electrolyte solution.
3. Chemical analyses of the magnesium deposit from the electrolyte such as Magnesium metal identification using XRD, Chemical composition analysis using EDS.

4. Morphology analysis of the magnesium deposit from the electrolyte by SEM.

5. XPS analysis of the anode-electrolyte interphase.

1.3 Dissertation overview

Chapter 1 describes the current problem in magnesium battery electrolytes which the author intends to address. Furthermore, the objective and scope of the thesis are described, and the structure of the thesis is also elaborated in this chapter.

Chapter 2 expounds on the literature review needed to understand the background behind the research. It begins with the motivation behind the current research in rechargeable magnesium batteries, followed by the working principle of the battery. Some of the critical requirements needed to be achieved by the battery cell for functional use are then described. Afterward, a more in-depth discussion on the prerequisite for a functional electrolyte, along with a review on the development of the rechargeable magnesium battery electrolyte from its inception until now are laid. The chapter ends with a summary of the performance of various electrolytes that had been discovered.

Chapter 3 elaborates on the experimental procedures used in this thesis, such as:

- The rationale behind the electrolyte formulation.
- The fabrication process of battery components such as electrolyte, electrode, and coin cell.

- Working mechanism and experimental procedure of the characterizations conducted in the thesis report.

Chapter 4 discusses the preliminary study conducted in the thesis report, which includes:

- Comparative study of various commercial magnesium salts ($Mg(OTF)_2$, $Mg(TFSI)_2$, $Mg(ClO_4)_2$, and $Mg(HMDS)_2$) solubility and capability for reversible magnesium plating and stripping process. This section primarily shows two potential salts to be used: (1) $Mg(HMDS)_2$ which has the highest Coulombic efficiency and relatively higher magnesium plating and stripping overpotential, and (2) $Mg(OTF)_2$-based electrolyte, which has the second-best Coulombic efficiency amongst the salt and relatively low overpotential for plating and stripping.

- Optimization of magnesium triflate-based electrolyte using borohydride and chloride-based additives.

- Limitation of $Mg(OTF)_2$-based electrolytes in terms of poor Coulombic efficiency and limited potential window.

- Indication of corrosion upon the addition of minuscule content of $MgCl_2$ into the $Mg(OTF)_2$- and $Mg(HMDS)_2$-based electrolytes.

Chapter 5 discusses the optimization and performance characterization of $Mg(HMDS)_2$-based electrolyte, including:

- Evaluation of the effects of $TBABH_4$ and $MgCl_2$ on the anodic stability and half-cell performance of the magnesium cell.

- Evaluation of various solvents for the $Mg(HMDS)_2$-based electrolyte and the optimization of the $Mg(HMDS)_2$-concentration in the electrolyte.

- Characterization of the electrolyte plating and stripping capability in various current densities and areal capacity.

- Identification of the chemical structure of the magnesium complex in the electrolyte.

- Morphology and chemical analyses of the magnesium crystal deposited from the electrolyte.
- Chemical analysis of the anode electrolyte interphase of the cycled magnesium anode.
- Full-cell performance of various cathodes using the $Mg(HMDS)_2$-based electrolyte.

Chapter 6 summarizes the findings of the result and analysis chapter, followed by a discussion on the implication of the research and suggestion for future works on electrolyte development.

1.4 Outcomes

Several outcomes are established in this report:

- Regardless of the magnesium salt types, moisture-induced passivation seems to be a major hindrance that needs to be overcome. In a chloride-free system, borohydride salt is an important additive to prevent moisture-induced passivation from happening. However, the borohydride salt concentration negatively correlates with the anodic stability limit potential of the electrolyte. This means that minimization of the borohydride content in the electrolyte must be done.

- The identity of the magnesium salt in the electrolyte determines several crucial aspects of the electrolyte. Firstly, salt stability determines the magnesium plating-stripping Coulombic efficiency and cell lifetime. Stable magnesium salt (i.e. $Mg(HMDS)_2$) also allows for decent magnesium anode compatibility without the need for chloride-based additives. Furthermore, magnesium deposit morphology is also dictated by the identity of the magnesium salt employed.

- By optimizing the electrolyte formulation of $Mg(HMDS)_2$-based electrolyte, the reported electrolyte is able to achieve a magnesium plating-stripping Coulombic Efficiency of 98.3%, anodic stability of 2.7 V on stainless-steel and 2.8 V on Aluminium, as well as good compatibility with CuS cathode.

References

1. Mohtadi, R.; Tutusaus, O., CHAPTER 2 Non-aqueous Electrolytes for Mg Batteries. In *Magnesium Batteries: Research and Applications*, The Royal Society of Chemistry: 2020; pp 17-59.

2. Mohtadi, R.; Mizuno, F., Magnesium Batteries: Current State of the Art, Issues and Future Perspectives. *Beilstein J. Nanotechnol.* **2014,** *5*, 1291-1311.

3. Yoo, H. D.; Shterenberg, I.; Gofer, Y.; Gershinsky, G.; Pour, N.; Aurbach, D., Mg Rechargeable Batteries: An on-Going Challenge. *Energy Environ. Sci.* **2013,** *6*, 2265-2279.

4. Tutusaus, O.; Mohtadi, R.; Arthur, T. S.; Mizuno, F.; Nelson, E. G.; Sevryugina, Y. V., An Efficient Halogen-Free Electrolyte for Use in Rechargeable Magnesium Batteries. *Angew. Chem. Int. Ed.* **2015,** *54*, 7900-7904.

5. Herb, J. T.; Nist-Lund, C. A.; Arnold, C. B., A Fluorinated Alkoxyaluminate Electrolyte for Magnesium-Ion Batteries. *ACS Energy Lett.* **2016,** *1*, 1227-1232.

6. Luo, J.; Bi, Y.; Zhang, L.; Zhang, X.; Liu, T. L., A Stable, Non-Corrosive Perfluorinated Pinacolatoborate Mg Electrolyte for Rechargeable Mg Batteries. *Angew. Chem. Int. Ed.* **2019,** *58*, 6967-6971.

7. Zhao-Karger, Z.; Gil Bardaji, M. E.; Fuhr, O.; Fichtner, M., A New Class of Non-Corrosive, Highly Efficient Electrolytes for Rechargeable Magnesium Batteries. *J. Mater. Chem. A* **2017,** *5*, 10815-10820.

Chapter 2

Literature Review

The proceeding text will describe the motivation behind the development of rechargeable magnesium battery electrolytes. This includes the applications of rechargeable batteries in society and the potential capability of rechargeable magnesium batteries to fulfill future demands in energy storage technology. The literature review then covers the working principles of rechargeable magnesium batteries and critical requirements that the battery needs to fulfill. In particular, a comprehensive review of the fundamental criterion the electrolyte needs to achieve will be given. Then, a thorough description of the development of rechargeable magnesium battery electrolytes will be given along with a benchmark table of the current electrolytes' capability.

2.1 The motivation behind the research in rechargeable magnesium battery

The world is facing a climate change issue that will continue to worsen unless significant mitigation is done to reduce human carbon emissions. According to The Intergovernmental Panel for Climate Change, various sectors with a major contribution to global green-house gas production include the energy sector (35%), transportation (14%), industry (21%), and land uses such as agriculture and forestry (24%).[1] Thus, reducing our fossil-fuel reliance on energy production and transportation will significantly limit our greenhouse gas emissions.

In both transportation and the energy sector, energy storage technologies have been increasingly used. The battery storage system will likely play an important role for our grid infrastructure as it allows for distributed energy storage, along with its cost-effectiveness, pollution-free nature, and considerable service life.[2] Rechargeable battery usage in Electric vehicles (EV) has also grown.[3] In particular, Lithium-Ion Batteries has been the primary choice for EV power source due to their affordable price, high energy density, and long cycle-life.[4, 5] In fact, Lithium-ion Battery (LiB) performance has been considered the most superior battery chemistry available due to its high specific power and specific energy density.[2]

However, dependency on LiB for future EV deployment is not sustainable due to the limited lithium resource currently known.[6] Moreover, metal anodes such as zinc, magnesium, or aluminum provide higher theoretical capacity compared to LIB anode.[7] In particular, Rechargeable Magnesium Battery (RMB) may be a prospective energy storage system that can be assembled from cheap and abundant magnesium with high anode capacity. The theoretical anode capacity of Magnesium is 3832 mAh cm^{-3}, larger than the theoretical capacity of LiB anode (LiC_6) as well as monovalent metal anodes currently in development such as lithium, sodium, and potassium metal.[2] Magnesium is also 10^4 times more abundant than lithium in the earth's crust.[8]

Nevertheless, various challenges in the field have to be addressed before rechargeable magnesium batteries can be commercialized. They include the sluggish diffusion of magnesium ion into high-voltage intercalation oxide cathodes[9], large capacity fade exhibited by sulfur conversion cathode,[10] and limited potential window due to current collector corrosion induced by the electrolyte[7, 10]. Arguably, the limited capability of the electrolyte has become the bottleneck in RMB research. Since electrolyte interacts with various parts of the battery, its compatibility with the anode, cathode, and current collector is crucial.

As will be described later, a wide potential window and chloride-free electrolytes have been synthesized for the Mg battery. Nevertheless, the magnesium salts used in these electrolytes are not commercially available. Since these salts need to be synthesized before use, the production method of the electrolyte may be complex and not scalable to industrial manufacturing. A huge quantity of expensive reagents may be needed too. Hence, the current formulation for chloride-free magnesium electrolytes limits the commercialization of RMB. Moreover, a novel formulation of wide potential window electrolytes should be scalable to industrial manufacturing practice and minimize the use of costly substances while fulfilling the battery requirement such as long cycle life, large potential window, high plating/stripping Coulombic efficiency, low reaction overpotential, non-dendritic metal deposition, adequate ionic conductivity, and non-nucleophilic nature.

2.2 Working principles of a rechargeable magnesium battery

In general, the rechargeable magnesium battery consists of a magnesium metal anode (negative electrode), an electrolyte-soaked separator layer, and lastly the cathode (positive electrode). During the discharge process, the magnesium metal anode oxidizes to magnesium ions. Accompanying this oxidation process is the chemical reduction of the cathode wherein the chemical species in the cathode accepts electrons while also reacting with the magnesium ion in the electrolyte to achieve charge neutrality. To sustain the reactions that are happening in both electrodes, the flow of electrons must happen through the electrical connection from the anode to the cathode, while the flow of magnesium ions (from the anode side to the cathode side) is maintained by the electrolyte solutions.

Once the chemical energy of the battery has been discharged, a charging process will be required to revert the chemical reactions that have happened during the battery discharge. In essence, the reduction of magnesium ions will happen on the anode side to reproduce magnesium metal and an oxidation process will occur on the cathode side, releasing magnesium ions to the electrolyte and free electrons. Both processes are also accompanied by the flow of electrons from the cathode side to the anode as well as the flow of magnesium ions from the cathode, through the electrolyte, to the anode.

2.3 General requirements of a rechargeable magnesium battery

Firstly, there is a need to sustain a highly conductive pathway for the magnesium ions to travel from one electrode to the other. Therefore, this entails, not only the need for highly conductive electrolyte,[11] but also the prevention of passivating (i.e. non-conductive) surface film formation on the anode and cathode sides[12].

For safety consideration, an even more important aspect of the battery operation is the magnesium anode deposition morphology during the charging process.[7] Prevalently, it has been observed that various metal anodes (Li, Na, K, Mg, Zn) produce various morphologies such as highly packed crystal, mossy structure, tree-like dendrite, and porous agglomerates of metal spheres.[7, 13] Generally, non-homogeneous metal growth such as dendrites and spherical aggregates is undesirable.[7] During the deposition process of the metal, certain structures previously mentioned tends to grow away from the anode and tend to penetrate to the separator. If allowed to develop unconstrained, an internal electrical connection between both electrodes will be formed, resulting in a short circuit of the battery.[7] Subsequently, electrical current flowing through this internal-short circuit connection will heat the volatile electrolyte solution inside the battery and may cause a thermal run-away failure.[14]

Besides these requirements, parasitic side reactions need to be prevented as these reactions are generally irreversible and compete with the redox reaction that is supposed to happen in the electrodes. Such reaction, therefore, reduces the reversibility (or Coulombic Efficiency) of the cell [12, 15] and causes capacity decay[16]. Besides this main point, side reactions could also lead to the formation of passivating films on both electrodes and increase the internal resistance of the battery. [15, 17] Cathode performance is also a crucial aspect of the battery. These include (1) cathode resistance to dissolution into the electrolyte, (2) the diffusion barrier of Mg^{2+} into the cathode crystal, and (3) the reversibility of the cathode redox reaction.[9, 18, 19] Cathode dissolution into the electrolyte, for example, could lead to a self-discharge reaction, while high diffusion barrier of Mg^{2+} into the cathode would lead to a low discharge capacity.

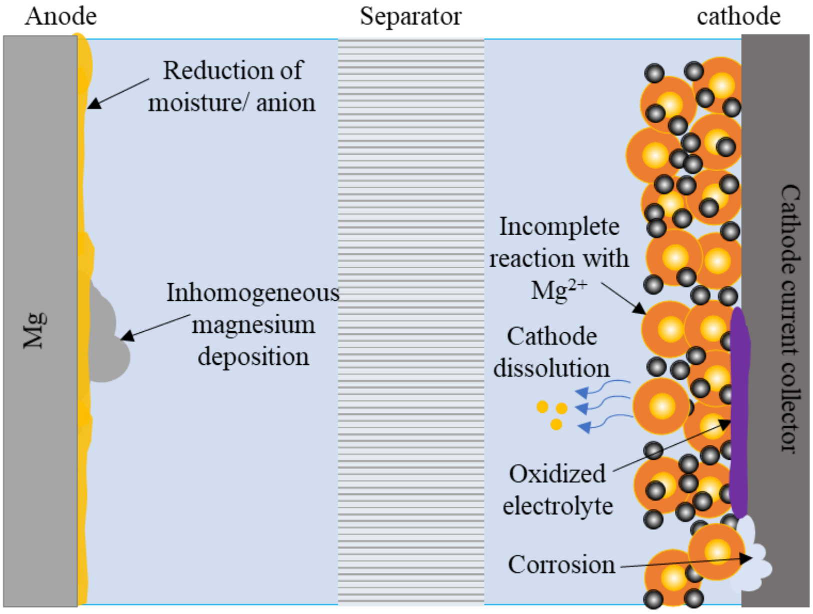

Figure 2.3.1: Degradation process of rechargeable magnesium battery.

2.4 Cathodes for rechargeable magnesium battery

Few active materials are suitable for magnesium battery cathode. The main challenge in finding a suitable cathode lies in the fact that the high charge density of Mg^{2+} reduces the diffusion capability of the ion into the active material crystal structure.[19] Moreover, since most electrolytes are ether-based, there is a natural limit of the electrolyte anodic stability of up to ~3.3 V vs Mg/Mg^{2+}.[20] Hence, the natural limitation to the cathode electrochemical potential has to be compensated with high capacity to achieve a significantly high energy density. Most of the cathode materials are chalcogenides material which has a lower Mg^{2+} solid-state diffusion barrier (in comparison to common oxide cathodes used in LIB).[9, 21]

In this thesis, two types of cathode material are used as cathode materials, Sulfur and CuS. CuS undergoes two steps electrochemical reduction in the battery discharge process as described below[22]

$$\text{Step 1: } 2CuS + Mg \rightarrow Cu_2S + MgS$$

$$\text{Step 2: } 2Cu_2S + MgS \rightarrow 4Cu + MgS$$

From the reaction described above, it can be seen that the S^{2-} ions of the CuS lattice ideally have no electrochemical activity. However, the S^{2-} lattice lowers the magnesium ion diffusion barrier (as compared to the oxide analogue CuO) as the lower charge density of S^{2-} minimizes the electrostatic interaction between S^{2-} and Mg^{2+}.[9, 21]

Meanwhile, the reaction mechanism of sulfur reduction is more complicated as it consists of multiple reaction steps. In a typically S_8 cathode, the sulfur molecule is reduced into polysulfide species (MgS_x, $x \leq 8$). With each reaction step, the S-S bonds in the polysulfides species are broken down, leading to the reduction in the polysulfide chain length until the material is converted to MgS.[18]

2.5 Requirements of a rechargeable magnesium battery electrolyte

As previously mentioned, electrodes passivation, dendritic growth, and side reactions are general failure mechanisms that need to be avoided in a rechargeable magnesium battery. As these problems are heavily intertwined with the chemical nature of the electrolyte, there is a need to discuss common electrolyte parameters that are important for the RMB.

Due to the highly reductive nature of magnesium metal, most types of magnesium electrolytes are not compatible with rechargeable magnesium batteries. This is because most organic solvents (besides ether) and common commercial magnesium salts (such as $Mg(TFSI)_2$, $Mg(OTF)_2$, $Mg(BF_4)_2$, etc.) will undergo electrochemical reduction when in contact with the magnesium metal. [11, 23] Generally, this decomposition process leads to the formation of a passivating film which prevents reversible magnesium deposition and dissolution from happening. The ability of the electrolyte to resist being chemically reduced by the anode is an important parameter called the reductive stability of the electrolyte. Usually, Molecular Orbital energy understanding the electrolytes' species are needed to predict the reductive stability of the electrolyte. In particular, for the electrolyte to resist decomposition by the magnesium anode, its Lowest Unoccupied Molecular Orbital (LUMO) energy level must be well above that of the magnesium metal chemical potential.[14, 15, 24] The electrolyte purity is also an important aspect as any traces of oxygen, water, and protic species tends to passivate the magnesium anode.[25, 26]

Naturally, electrolyte decomposition may also occur through the oxidation process of the electrolyte. This can happen either by the reaction of the electrolyte with the cathode or through the electrolysis of the electrolyte when the battery is charged at a high potential. Anodic stability, therefore, is an important factor that has to be considered as well. Generally, the anodic stability of the electrolyte can be determined by the energy level of the Highest Occupied Molecular Orbitals (HOMO) of the electrolyte species.[14]

Lower HOMO level will lead to a wider electrolyte potential window as it prevents the electrolyte from decomposing at high potential. It is important to mention that the potential window of the electrolyte is also determined by the cathode's current collector (the metal foil which serves as the cathode film's substrate) and other metallic parts of the cell. A pervasive problem in rechargeable batteries is the corrosion of the metallic current collectors of the battery electrode.[10, 16, 19] As metal corrosion tends to happen at high electrical potential, corrosion becomes another pervasive side reaction that tends to occur during the battery charging process. Although not a requirement, a non-nucleophilic characteristic is also desired in magnesium battery electrolytes. This is due to the current interest in developing Mg/S batteries with a significantly larger capacity than other cathodes materials.[27] Elemental sulfur, however, tends to react with nucleophilic species, rendering them incompatible for Mg/S battery use.[27]

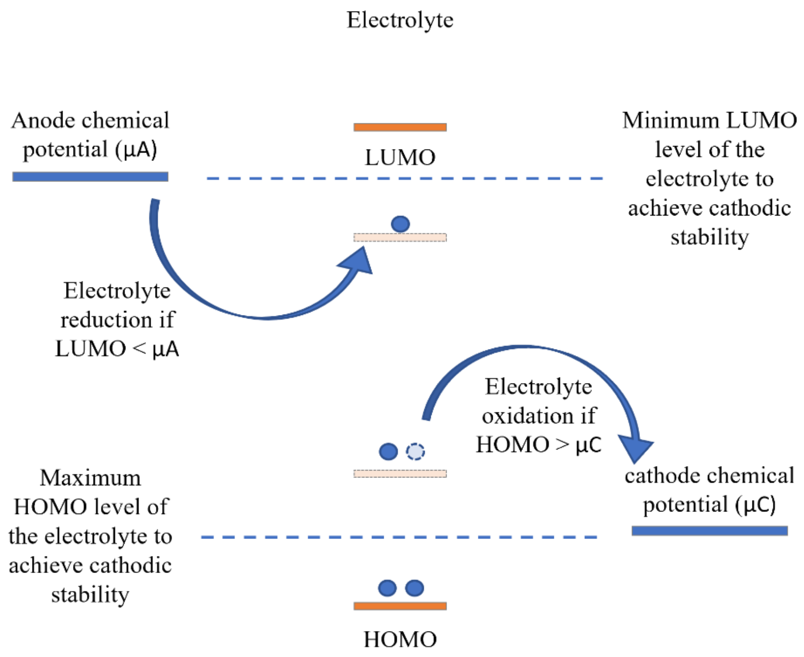

Figure 2.5.1: Stability requirement of rechargeable magnesium battery electrolyte.

For safety concerns previously mentioned in § 2.1., dendritic or inhomogenous metal deposition needs to be avoided during the battery charging process. Although it was ascertained that magnesium has a lesser tendency to form dendrite due to its high surface self-diffusivity[28], dendritic growth of magnesium has been demonstrated in various conditions[29, 30]. In theory, dendrite tends to form when there is a high mass transport limitation of magnesium ion flow from the electrolyte to the anode.[14] Thus, the ionic conductivity of the electrolyte is an important factor to prevent dendritic growth from happening. Other relevant considerations are the anode/electrolyte interphase wherein inhomogeneity in the interphase conductivity and electrode smoothness could lead to preferential magnesium deposition in localized region[28].

Finally, to attain high energy efficiency during the charge and discharge cycle, it is also important to maintain a low overpotential for the cathode and anode electrochemical reactions. Generally, overpotential refers to the shift in the potential of an electrochemical reaction from its equilibrium potential.[14] Such shifts arise from the existence of an activation energy barrier for the electrochemical reaction or mass transport limitation to sustain the chemical reaction.[31] Naturally as the electrodes' reactions involve magnesium ion solvation and de-solvation process, the chemical complex formed by the magnesium ion in the electrolyte determines the energy barrier of the electrochemical reactions.[32, 33]

2.6 Development of RMB electrolyte

Initially, only a few compounds were known to have high reductive stability against magnesium metal. One of the earliest magnesium compounds known for reversible magnesium deposition and dissolution are Grignard reagents (MgRX; X: halide ion, R: alkyl group).[10, 19] Other compounds known to enable reversible magnesium deposition and are $Mg(B(C_4H_9)_4)_2$[34] and magnesium borohydride ($Mg(BH_4)_2$)[35]. However, as these compounds tend to have low anodic stability (primarily due to their highly reductive nature), they are not suitable for high voltage battery applications.[11, 12, 19] Thus, subsequently, various methods to extend the anodic stability of the electrolyte were explored.

Mainly by combining the organomagnesium salts with Lewis acid, higher stability was achieved.[12, 19, 36] Through this method, an electrolyte with magnesium plating and stripping Coulombic efficiency of 100 % and oxidative stability of 2.2 V was created by the combination of $MgBu_2$ and $AlCl_2Et$ at a 1:2 ratio.[10, 19] Later on, it was further discovered by Aurbach *et al.* that the weak Al-C bond in the anion species can be broken due to beta-hydrogen elimination.[10, 36, 37] This prevents the electrolyte from achieving high anodic stability. Hence, by substituting the alkyl chains of the organometallic reagents with phenyl groups, the electrolytes' anodic stability was further increased up to 3.3 V vs Mg. This electrolyte formulation is commonly known as APC (All Phenyl Complex, made from PhMgCl and $AlCl_3$ at 2:1 ratio). However, the organometallic reagent is a strong reducing agent which will react with water molecules and thus is sensitive to moisture-containing air.[38] This means that the electrolyte would severely degrade if it comes into contact with air. The nucleophilic nature of such reagent also does not permit the use of Sulfur cathode which has high charge capacity but is reactive toward nucleophilic substances.[27, 39]

Due to the limitation of Grignard-based compounds, other salts with non-nucleophilic characteristics were explored. Usually, these electrolytes are made by mixing commercial magnesium salts with chloride-based compounds ($AlCl_3$, $MgCl_2$, or $CrCl_3$).[40-45] Chloride compounds are added to these electrolytes mainly to increase the reversibility of the deposition and dissolution process of the magnesium anode[46], alleviate passivation, improve the Coulombic efficiency, and reduce the plating and stripping overpotential[47]. The exact mechanism by which chloride ion gives an improvement in the electrolyte is not clearly understood. Nevertheless, there are several proposals for its functionality. It is argued that chloride ions adsorb on the surface of magnesium and prevent the reduction of trace water which would have passivated the Mg metal by forming $Mg(OH)_2$/MgO layer.[16] Several sources also indicate that chloride reduces the stability of the oxide layer or passivation layer on the magnesium metal. This effect is beneficial as it effectively removes the pacifying film on the magnesium surface.[16, 48] It is also hypothesized that Mg-Cl clusters in the magnesium electrolyte have reduced desolvation energy due to reduced charge density of the ion cluster compared to Mg^{2+} ion. Thus, Mg-Cl complexes have a lower deposition overpotential when chloride is added to the electrolyte.[26]

It is important to note, however, that chloride limits the potential window of the electrolyte by inducing corrosion in non-noble current collectors.[49] Often, the primary mode of current collector degradation in a chloride-containing electrolyte is pitting corrosion,[16] a form of accelerated metal dissolution induced by the breakdown of the passivation film (native oxide film) on the surface of the metal surface.[50] As reported in previous studies, the corrosion process contributes to the parasitic reaction of the cell and leads to faster battery capacity degradation.[51, 52]

Besides the addition of chloride, a common approach to extend the potential window of the electrolyte is to use novel magnesium salts. Recently, there is a surge in interest in novel boron-based magnesium electrolytes due to their high anodic stability. A critical achievement in magnesium electrolyte research is the discovery of

$Mg(CB_{11}H_{12})_2$ electrolytes with Coulombic efficiency of 99% and anodic stability beyond 3.8 V vs Mg.[53] However, $Mg(CB_{11}H_{12})_2$-based electrolyte is unlikely to be utilized in a commercial battery as its production method is highly complicated.[54] Following this discovery, other high-performance electrolytes with simpler synthesis methods were discovered. These include $Mg(Al(HFIP)_4)_2$[55], $Mg(B(HFIP)_4)_2$[56], and $Mg(B(PFPINA)_2)_2$.[57] Due to the anions' weakly coordinating nature, these salts tend to be highly conductive.[57, 58] Moreover, they allow for a highly reversible magnesium plating and stripping (CE of 98%) and enable the use of Sulfur cathode and stainless-steel current collector with anodic stability of 3 V or above.

Currently, boron-based electrolytes (e.g. $Mg(B(HFIP)_4)_2$) are more favored than aluminum-based electrolytes (e.g. $Mg(Al(HFIP)_4)_2$) as boron-based electrolytes are more resistant towards air-induced decomposition.[56] State-of-the-Art borate-based electrolytes such as $Mg(CB_{11}H_{12})_2$ and $Mg(B(HFIP)_4)_2$ are appealing for battery electrolytes as their solution has high ionic conductivity, wide potential window, and great stability against the magnesium metal. The great capability of the electrolytes most likely arises due to the highly delocalized charge distribution of the electrolyte anion.[53, 59] The delocalized charge distribution reduces the cation-anion interaction of the magnesium salt and eases the cation and anion separation in the electrolyte. This property, therefore, improves the solubility of the salt, leading to higher ionic conductivity. In the case of $Mg(B(HFIP)_4)_2$, the highly fluorinated structure of the anion makes the HOMO level of the anion low, thereby preventing the oxidation of the anion.[59] Similarly, the high stability of $Mg(CB_{11}H_{12})_2$, owing to the aromaticity of the anion,[60] increases its potential window.

The great compatibility of borate-based electrolytes with the anode is also one of their appealing characteristics. In the case of $Mg(CB_{11}H_{12})_2$, the salt seems to be reductively stable against magnesium anode as no signs of anion decomposition are observed in the anode electrolyte interphase[61]. On the other hand, salts such as $Mg(B(HFIP)_4)_2$ decomposes during the cell operation as indicated through XPS analysis by Tang *et al.* The ability of the electrolyte to conduct magnesium plating and stripping may, therefore, relates to the decomposition rate of the electrolyte or the structure of the SEI that is formed.[62] It was also suggested in previous publications that the increased anodic stability of these salts may be due to their weakly coordinating nature with Mg^{2+}. With strong Mg^{2+}-anion interaction, cation-anion clusters are formed, and these clusters may have reduced cathodic stability as compared to the free anion species[32, 59]. This is due to the reduced LUMO energy level of the anion upon complexing with Mg^{2+}. Nevertheless, $Mg(B(HFIP)_4)_2$ is still a moisture-sensitive compound and would decompose if the electrolyte contains a trace amount of water.[37] Issues regarding short-circuit formation, unstable cycling, unreliable batch-to-batch performance has also been associated with the $Mg(B(HFIP)_4)_2$ electrolyte.[62, 63]

It is important to note that other magnesium electrolytes were made by mixing Tetrakis-hexafluoroisopropylborate anion with unique cationic species. Generally, they are made by combining magnesium salts (e.g. $MgCl_2$, MgF_2, MgO and $Mg(BH_4)_2$) with Tris-(2H hexaflouroisopropyl) borate (THFPB).[64-66] These electrolytes exhibit high magnesium deposition/dissolution Coulombic efficiency (potentially due to the inherent compatibility of the anion with magnesium metal) and varying ionic conductivity. MgF_2- and MgO-based electrolytes seem to have low ionic conductivity[64, 66] while $Mg(BH_4)_2$ and $MgCl_2$ based electrolytes have a high ionic conductivity[65, 67]. This may suggest that the ionic conductivity depends on the solubility of the magnesium salt used.

2.7 Summary of Current Electrolyte Characteristics

Table 2.6.1 shows the performance metric of various electrolytes based on plating and stripping overpotentials, the magnesium plating and stripping Coulombic efficiency in the electrolyte, the anodic stability of the electrolyte, and the ionic conductivity of the electrolyte. The table presents three types of magnesium battery electrolytes: chloride-based non-nucleophilic electrolytes (No. 1-14), chloride-free weakly coordinated anion-based electrolytes (No. 15-18), and chloride-free THFPB-based electrolytes (No. 19-21).

In general, chloride-based electrolytes can be fabricated by mixing various commercially available chemicals. Thus, their fabrication process tends to be simple. The drawback of using these electrolytes, generally, is their low anodic stability against non-noble current collector (≤2.65 V vs Mg on Stainless-steel and ≤2.5 V vs Mg on Aluminium). On the other hand, chloride-free electrolytes (No. 15-21) tend to have high anodic stability (>3V vs Mg) on aluminium and stainless steel. The weakly coordinated anion-based electrolytes (No. 15-18) have a complicated fabrication procedure due to the need to pre-synthesize the magnesium salt while the THFPB-based electrolytes (No.

19-21) are simpler to make. However, it is worth noting that THFPB is costly ($497/5 g, TCI America).

Interestingly, several notable chloride-based electrolytes seem to show high anodic stability on non-noble current collectors. These include OMBB (Mg-$MgCl_2$-THFPB, no. 11) electrolyte with anodic stability of ~3 V on Aluminium,[67] Mg-$CrCl_3$-THFPB-based electrolyte (no.14) with anodic stability of 3.46 V on Aluminium,[68] MBA-[C_2mim] [$AlCl_4$] electrolyte (no. 12) with anodic stability of 3 V on Stainless-steel, [69] and [Mg_2Cl_3] [$Al(PFPINA)_2(THF)$] (no. 13) with anodic stability of more than 3 V[70]. In the case of OMBB electrolyte, this observation was explained by the passivation process of the aluminium electrode after the anodic reaction has happened on the electrode. Ha *et al.* in their study of Mg-$CrCl_3$-THFPB-based electrolytes also attributed the anodic stability of their electrolyte due to the less corrosive nature of chloride-free anion in the electrolyte.[68] It is important to highlight, however, that the anodic stability of most of these electrolytes (except for MBA-[C_2mim] [$AlCl_4$] electrolyte[68]) are not investigated by long-duration chronoamperometry measurement. As will be shown in chapter 5, LSV may overestimate the corrosion onset potential of the electrolyte as the timescale of LV experiments tends to be small.

Table 2.7.1: Summary table of current electrolyte characteristics.

	Electrolyte	Overpotential (V)	CE (%)	Anodic stability vs. Mg (V)	Conductivity (mS cm^{-1})	Remarks
1	MACC (Ref[41])	<0.2 (0.5 mA cm^{-2})	98.8	3.1 (Pt)	~2	Corrosive but non-nucleophilic.
2	$Mg(HMDS)_2$-$AlCl_3$/Diglyme (Ref[40])	< 0.2 (0.5 mA cm^{-2})	99	3.9 (Pt), **2.6 (SS)**	1.7	
3	$Mg(HMDS)_2$-$4MgCl_2$/THF(Ref[71])	N.A.	99	2.8 (Pt)	0.7	
4	$Mg(TFSI)_2$-$MgCl_2$ (Ref[43])	N.A.	93	3 (Pt), **2.5 (SS)**	N.A.	
5	$Mg(OTF)_2$-$MgCl_2$-$AlCl_3$-Anthracene (Ref[44])	0.1 (0.088 mA cm^{-2})	>95 (0.088 mA cm^{2}), 98.5 (1 mA cm^{-2})	3.25 (Pt), **2.5 (SS),** **1.85 (Al)**	1.8	
6	$Mg(OTF)_2$-$MgCl_2$-$AlCl_3$ (Ref[45])	0.25 (0.05 mA cm^{-2})	99.1	3 (Pt), **1.75 (SS),** **2.5 (Al)**	N.A.	
7	MBA-$AlCl_3$ (Ref[72])	<0.2 [plate], < 0.1 [strip] (0.088 mA cm^{-2})	>97	2.25 (Pt), **2.35 (Al),** **2.65 (SS)**	0.947	
8	MBA-$MgCl_2$-$AlCl_3$ (Ref[73])	<0.1 (0.088 mA cm^{-2})	98	2.56 (Pt), **1.46 (Al),** **2.1 (SS)**	N.A.	
9	MMAC/DME (Ref[42])	N.A.	100	3.3 (Pt), **2.2 (SS),** **0.8 (Al)**	N.A.	
10	MaCC/THF (Ref[74])	N.A.	100	3.1 (Pt), **2.5 (SS)**	0.23	
11	OMBB (Ref[67])	N.A.	98.5 (0.1 mA cm^{-2})	3.3 (Pt), **3 (Al),** **2.5 (SS)**	5.58	
12	MBA/$[C_2mim][AlCl_4]$ (Ref[69])	N.A.	95-98	**>3 (SS)**	N.A.	N.A.
13	$[Mg_2Cl_3][Al(PFPINA)_2(THF)]$/THF (Ref[70])	~0.18 (0.5 mA cm^{-2})	~99	**>3 (SS)**	N.A.	N.A.
14	Mg-THFPB-$CrCl_3$/DME (Ref[68])	0.05 (15 µA cm^{-2})	92	**~3.5 (Al)**	4	N.A.
15	$Mg(CB_{11}H_{12})_2$/G4	0.25 [plate], 0.01 [strip] (1 mA cm^{-2}) (Ref[61])	99 (Ref[53]), 97 (Ref[61])	3.8-4.0 V (Al, SS, Pt) (Ref[53])	1.8	Complicated synthesis procedure.
16	$Mg(Al(HFIP)_4)_2$ (Ref[55])	<0.5 (0.5 mA cm^{-2})	99.3	**< 3 (Al, SS)**	6.5	sensitive to moisture.
17	$Mg(B(HFIP)_4)_2$ (Ref[56])	<0.2 (0.5 mA cm-^{2})	>98	3.5 (Pt), **4.3 (SS, Al)**	11 (Ref[75])	Commercially unavailable.

18	$Mg(B(PFPINA)_2)_2$ (Ref[57])	0.09 (1 mA cm^{-2})	95	**4.0 (SS, Al)**	3.95	
19	THFPB + MgF_2 (Ref[64])	N.A.	99.8	**>3.5 (SS), 3.8 (Al)**	1.1	N.A.
20	THFPB + MgO (Ref[66])	<0.1 (0.05 mA cm^{-2})	N.A.	**>4.0 (SS), 4.2 (Al)**	0.174	N.A.
21	THFPB + $Mg(BH_4)_2$ (Ref[65])		99	**2.8 (SS), 1.6 (Al)**	3.72	N.A.

References

1. Intergovernmental Panel on Climate, C., *Climate Change 2014: Mitigation of Climate Change: Working Group III Contribution to the IPCC Fifth Assessment Report*. Cambridge University Press: Cambridge, 2015.

2. Gür, T. M., Review of electrical energy storage technologies, materials and systems: challenges and prospects for large-scale grid storage. *Energy Environ. Sci.* **2018,** *11*, 2696-2767.

3. Tie, S. F.; Tan, C. W., A review of energy sources and energy management system in electric vehicles. *Renew. Sustain. Energy Rev.* **2013,** *20*, 82-102.

4. Cano, Z. P.; Banham, D.; Ye, S.; Hintennach, A.; Lu, J.; Fowler, M.; Chen, Z., Batteries and fuel cells for emerging electric vehicle markets. *Nat. Energy* **2018,** *3*, 279-289.

5. Feng, X.; Ouyang, M.; Liu, X.; Lu, L.; Xia, Y.; He, X., Thermal runaway mechanism of lithium ion battery for electric vehicles: A review. *Energy Storage Mater.* **2018,** *10*, 246-267.

6. Weil, M.; Ziemann, S.; Peters, J., The Issue of Metal Resources in Li-Ion Batteries for Electric Vehicles. In *Behaviour of Lithium-Ion Batteries in Electric Vehicles: Battery Health, Performance, Safety, and Cost*, Pistoia, G.; Liaw, B., Eds. Springer International Publishing: Cham, 2018; pp 59-74.

7. Liang, Y.; Dong, H.; Aurbach, D.; Yao, Y., Current Status and Future Directions of Multivalent Metal-Ion Batteries. *Nat. Energy* **2020,** *5*, 646-656.

8. Liu, F.; Wang, T.; Liu, X.; Fan, L. Z., Challenges and Recent Progress on Key Materials for Rechargeable Magnesium Batteries. *Adv. Energy Mater.* **2020,** *11*, 2000787.

9. Canepa, P.; Sai Gautam, G.; Hannah, D. C.; Malik, R.; Liu, M.; Gallagher, K. G.; Persson, K. A.; Ceder, G., Odyssey of Multivalent Cathode Materials: Open Questions and Future Challenges. *Chem. Rev.* **2017,** *117*, 4287-4341.

10. Song, J.; Sahadeo, E.; Noked, M.; Lee, S. B., Mapping the Challenges of Magnesium Battery. *J. Phys. Chem. Lett.* **2016,** *7*, 1736-1749.

11. Yoo, H. D.; Shterenberg, I.; Gofer, Y.; Gershinsky, G.; Pour, N.; Aurbach, D., Mg Rechargeable Batteries: An on-Going Challenge. *Energy Environ. Sci.* **2013,** *6*, 2265-2279.

12. Li, M.; Lu, J.; Ji, X.; Li, Y.; Shao, Y.; Chen, Z.; Zhong, C.; Amine, K., Design strategies for nonaqueous multivalent-ion and monovalent-ion battery anodes. *Nat. Rev. Mater.* **2020,** *5*, 276-294.

13. Davidson, R.; Verma, A.; Santos, D.; Hao, F.; Fincher, C. D.; Zhao, D.; Attari, V.; Schofield, P.; Van Buskirk, J.; Fraticelli-Cartagena, A.; Alivio, T. E. G.; Arroyave, R.; Xie, K.; Pharr, M.; Mukherjee, P. P.; Banerjee, S., Mapping mechanisms and growth regimes of magnesium electrodeposition at high current densities. *Mater. Horiz.* **2020,** *7*, 843-854.

14. Bonnick, P.; Muldoon, J., A Trip to Oz and a Peak Behind the Curtain of Magnesium Batteries. *Adv. Funct. Mater.* **2020,** *30*, 1910510.

15. Gao, T.; Hou, S.; Huynh, K.; Wang, F.; Eidson, N.; Fan, X.; Han, F.; Luo, C.; Mao, M.; Li, X.; Wang, C., Existence of Solid Electrolyte Interphase in Mg Batteries: Mg/S Chemistry as an Example. *ACS Appl. Mater. Interfaces* **2018,** *10*, 14767-14776.

16. Zhao, X.; Zhao-Karger, Z.; Fichtner, M.; Shen, X., Halide-Based Materials and Chemistry for Rechargeable Batteries. *Angew. Chem. Int. Ed.* **2020,** *59*, 5902-5949.

17. Mohtadi, R., Beyond Typical Electrolytes for Energy Dense Batteries. *Molecules* **2020,** *25*.

18. Nguyen, D.; Horia, R.; Eng, A. Y. S.; Song, S.-W.; Seh, Z., Material design strategies to improve the performance of rechargeable magnesiu• sulfur batteries. *Mater. Horiz.* **2021**.

19. Bucur, C. B.; Gregory, T.; Oliver, A. G.; Muldoon, J., Confession of a Magnesium Battery. *J. Phys. Chem. Lett.* **2015,** *6*, 3578-3591.

20. Kar, M.; Tutusaus, O.; MacFarlane, D. R.; Mohtadi, R., Novel and versatile room temperature ionic liquids for energy storage. *Energy Environ. Sci.* **2019,** *12*, 566-571.

21. Regulacio, M. D.; Nguyen, D.-T.; Horia, R.; Seh, Z. W., Designing Nanostructured Metal Chalcogenides as Cathode Materials for Rechargeable Magnesium Batteries. *Small* **2021,** *17*, 2007683.

22. Ren, W.; Xiong, F.; Fan, Y.; Xiong, Y.; Jian, Z., Hierarchical Copper Sulfide Porous Nanocages for Rechargeable Multivalent-Ion Batteries. *ACS Appl. Mater. Interfaces* **2020,** *12*, 10471-10478.

23. Shi, J.; Zhang, J.; Guo, J.; Lu, J., Interfaces in rechargeable magnesium batteries. *Nanoscale Horiz.* **2020,** *5*, 1467-1475.

24. Liu, C.; Neale, Z. G.; Cao, G., Understanding electrochemical potentials of cathode materials in rechargeable batteries. *Mater. Today* **2016,** *19*, 109-123.

25. Connell, J. G.; Genorio, B.; Lopes, P. P.; Strmcnik, D.; Stamenkovic, V. R.; Markovic, N. M., Tuning the Reversibility of Mg Anodes via Controlled Surface Passivation by H_2O/Cl^- in Organic Electrolytes. *Chem. Mater.* **2016,** *28*, 8268-8277.

26. Attias, R.; Salama, M.; Hirsch, B.; Goffer, Y.; Aurbach, D., Anode-Electrolyte Interfaces in Secondary Magnesium Batteries. *Joule* **2019,** *3*, 27-52.

27. Zhao-Karger, Z.; Fichtner, M., Magnesium–sulfur battery: its beginning and recent progress. *MRS Commun.* **2017,** *7*, 770-784.

28. Hao, F.; Verma, A.; Mukherjee, P. P., Electrodeposition stability of metal electrodes. *Energy Storage Mater.* **2019,** *20*, 1-6.

29. Davidson, R.; Verma, A.; Santos, D.; Hao, F.; Fincher, C.; Xiang, S.; Van Buskirk, J.; Xie, K.; Pharr, M.; Mukherjee, P. P.; Banerjee, S., Formation of Magnesium Dendrites during Electrodeposition. *ACS Energy Lett.* **2019,** *4*, 375-376.

30. Ding, M. S.; Diemant, T.; Behm, R. J.; Passerini, S.; Giffin, G. A., Dendrite Growth in Mg Metal Cells Containing Mg(TFSI)2/Glyme Electrolytes. *J. Electrochem. Soc.* **2018,** *165*, A1983-A1990.

31. Bard, A. J.; Faulkner, L. R., *Electrochemical Methods: Fundamentals and Applications*. Second Edition ed.; John Wiley & Sons, Inc.: New York, 2001; p 864.

32. Tuerxun, F.; Yamamoto, K.; Mandai, T.; Tateyama, Y.; Nakanishi, K.; Uchiyama, T.; Watanabe, T.; Tamenori, Y.; Kanamura, K.; Uchimoto, Y., Effect of Interaction among Magnesium Ions, Anion, and Solvent on Kinetics of the Magnesium Deposition Process. *J. Phys. Chem. C* **2020,** *124*, 28510-28519.

33. Attias, R.; Bublil, S.; Salama, M.; Goffer, Y.; Aurbach, D., How solution chemistry affects the electrochemical behavior of cathodes for Mg batteries, a classical electroanalytical study. *Electrochim. Acta* **2020,** *334*, 135614.

34. Gregory, T. D., Nonaqueous Electrochemistry of Magnesium: Applications to Energy Storage. *J. Electrochem. Soc.* **1990,** *137*, 775.

35. Mohtadi, R.; Matsui, M.; Arthur, T. S.; Hwang, S.-J., Magnesium Borohydride: From Hydrogen Storage to Magnesium Battery. *Angew. Chem. Int. Ed.* **2012,** *51*, 9780-9783.

36. Mohtadi, R.; Mizuno, F., Magnesium Batteries: Current State of the Art, Issues and Future Perspectives. *Beilstein J. Nanotechnol.* **2014,** *5*, 1291-1311.

37. Wang, H.; Ryu, J.; Shao, Y.; Murugesan, V.; Persson, K.; Zavadil, K.; Mueller, K. T.; Liu, J., Advancing Electrolyte Solution Chemistry and Interfacial Electrochemistry of Divalent Metal Batteries. *ChemElectroChem* **2021,** *n/a*.

38. Muldoon, J.; Bucur, C. B.; Oliver, A. G.; Sugimoto, T.; Matsui, M.; Kim, H. S.; Allred, G. D.; Zajicek, J.; Kotani, Y., Electrolyte roadblocks to a magnesium rechargeable battery. *Energy Environ. Sci.* **2012,** *5*, 5941-5950.

39. Zhang, Z.; Dong, S.; Cui, Z.; Du, A.; Li, G.; Cui, G., Rechargeable Magnesium Batteries using Conversion-Type Cathodes: A Perspective and Minireview. *Small Methods* **2018,** *2*, 1800020.

40. Zhao-Karger, Z.; Zhao, X.; Fuhr, O.; Fichtner, M., Bisamide Based Non-Nucleophilic Electrolytes for Rechargeable Magnesium Batteries. *RSC Adv.* **2013,** *3*, 16330-16335.

41. Doe, R. E.; Han, R.; Hwang, J.; Gmitter, A. J.; Shterenberg, I.; Yoo, H. D.; Pour, N.; Aurbach, D., Novel, electrolyte solutions comprising fully inorganic salts with high anodic stability for rechargeable magnesium batteries. *Chem. Commun.* **2014,** *50*, 243-245.

42. Luo, J.; He, S.; Liu, T. L., Tertiary Mg/MgCl2/AlCl3 Inorganic Mg2+ Electrolytes with Unprecedented Electrochemical Performance for Reversible Mg Deposition. *ACS Energy Lett.* **2017,** *2*, 1197-1202.

43. Gao, T.; Hou, S.; Wang, F.; Ma, Z.; Li, X.; Xu, K.; Wang, C., Reversible S^0/MgS_x Redox Chemistry in a $MgTFSI_2/MgCl_2$/DME Electrolyte for Rechargeable Mg/S Batteries. *Angew. Chem. Int. Ed.* **2017,** *56*, 13526-13530.

44. Yang, Y.; Wang, W.; Nuli, Y.; Yang, J.; Wang, J., High Active Magnesium Trifluoromethanesulfonate-Based Electrolytes for Magnesium–Sulfur Batteries. *ACS Appl. Mater. Interfaces* **2019,** *11*, 9062-9072.

45. Huang, D.; Tan, S.; Li, M.; Wang, D.; Han, C.; An, Q.; Mai, L., Highly Efficient Non-Nucleophilic $Mg(CF_3SO_3)_2$-Based Electrolyte for High-Power Mg/S Battery. *ACS Appl. Mater. Interfaces* **2020,** *12*, 17474-17480.

46. Connell, J. G.; Zorko, M.; Agarwal, G.; Yang, M.; Liao, C.; Assary, R. S.; Strmcnik, D.; Markovic, N. M., Anion Association Strength as a Unifying Descriptor for the Reversibility of Divalent Metal Deposition in Nonaqueous Electrolytes. *ACS Appl. Mater. Interfaces* **2020,** *12*, 36137-36147.

47. Liang, Z.; Ban, C., Strategies to Enable Reversible Magnesium Electrochemistry: From Electrolytes to Artificial Solid-Electrolyte Interphases. *Angew. Chem. Int. Ed. Engl.* **2021,** *60*, 11036-11047.

48. Kim, S. S.; Bevilacqua, S. C.; See, K. A., Conditioning-Free Mg Electrolyte by the Minor Addition of Mg(HMDS)2. *ACS Appl. Mater. Interfaces* **2020,** *12*, 5226-5233.

49. Soltis, J., Passivity breakdown, pit initiation and propagation of pits in metallic materials – Review. *Corros. Sci.* **2015,** *90*, 5-22.

50. Frankel, G. S., Pitting Corrosion of Metals: A Review of the Critical Factors. *J. Electrochem. Soc.* **1998,** *145*, 2186-2198.

51. Ha, J. H.; Cho, J.-H.; Kim, J. H.; Cho, B. W.; Oh, S. H., 1-Butyl-1-methylpyrrolidinium chloride as an effective corrosion inhibitor for stainless steel current collectors in magnesium chloride complex electrolytes. *J. Power Sources* **2017,** *355*, 90-97.

52. Yamada, Y.; Chiang, C. H.; Sodeyama, K.; Wang, J.; Tateyama, Y.; Yamada, A., Corrosion prevention mechanism of aluminum metal in superconcentrated electrolytes. *ChemElectroChem* **2015,** *2*, 1687-1694.

53. Tutusaus, O.; Mohtadi, R.; Arthur, T. S.; Mizuno, F.; Nelson, E. G.; Sevryugina, Y. V., An Efficient Halogen-Free Electrolyte for Use in Rechargeable Magnesium Batteries. *Angew. Chem. Int. Ed.* **2015,** *54*, 7900-7904.

54. Kong, L.; Yan, C.; Huang, J.-Q.; Zhao, M.-Q.; Titirici, M.-M.; Xiang, R.; Zhang, Q., A Review of Advanced Energy Materials for Magnesium–Sulfur Batteries. *ENERGY & ENVIRONMENTAL MATERIALS* **2018,** *1*, 100-112.

55. Herb, J. T.; Nist-Lund, C. A.; Arnold, C. B., A Fluorinated Alkoxyaluminate Electrolyte for Magnesium-Ion Batteries. *ACS Energy Lett.* **2016,** *1*, 1227-1232.

56. Zhao-Karger, Z.; Gil Bardaji, M. E.; Fuhr, O.; Fichtner, M., A New Class of Non-Corrosive, Highly Efficient Electrolytes for Rechargeable Magnesium Batteries. *J. Mater. Chem. A* **2017,** *5*, 10815-10820.

57. Luo, J.; Bi, Y.; Zhang, L.; Zhang, X.; Liu, T. L., A Stable, Non-Corrosive Perfluorinated Pinacolatoborate Mg Electrolyte for Rechargeable Mg Batteries. *Angew. Chem. Int. Ed.* **2019,** *58*, 6967-6971.

58. Krossing, I.; Raabe, I., Noncoordinating Anions—Fact or Fiction? A Survey of Likely Candidates. *Angew. Chem. Int. Ed.* **2004,** *43*, 2066-2090.

59. Lau, K.-C.; Seguin, T. J.; Carino, E. V.; Hahn, N. T.; Connell, J. G.; Ingram, B. J.; Persson, K. A.; Zavadil, K. R.; Liao, C., Widening Electrochemical Window of Mg Salt by Weakly Coordinating Perfluoroalkoxyaluminate Anion for Mg Battery Electrolyte. *J. Electrochem. Soc.* **2019,** *166*, A1510-A1519.

60. Chen, Z.; King, R. B., Spherical Aromaticity: Recent Work on Fullerenes, Polyhedral Boranes, and Related Structures. *Chem. Rev.* **2005,** *105*, 3613-3642.

61. Jay, R.; Tomich, A. W.; Zhang, J.; Zhao, Y.; De Gorostiza, A.; Lavallo, V.; Guo, J., Comparative Study of Mg(CB11H12)2 and Mg(TFSI)2 at the Magnesium/Electrolyte Interface. *ACS Appl. Mater. Interfaces* **2019,** *11*, 11414-11420.

62. Tang, K.; Du, A.; Dong, S.; Cui, Z.; Liu, X.; Lu, C.; Zhao, J.; Zhou, X.; Cui, G., A Stable Solid Electrolyte Interphase for Magnesium Metal Anode Evolved from a Bulky Anion Lithium Salt. *Adv. Mater.* **2020,** *32*, 1904987.

63. Mandai, T., Critical Issues of Fluorinated Alkoxyborate-Based Electrolytes in Magnesium Battery Applications. *ACS Appl. Mater. Interfaces* **2020,** *12*, 39135-39144.

64. Zhang, Z.; Cui, Z.; Qiao, L.; Guan, J.; Xu, H.; Wang, X.; Hu, P.; Du, H.; Li, S.; Zhou, X.; Dong, S.; Liu, Z.; Cui, G.; Chen, L., Novel Design Concepts of Efficient Mg-Ion Electrolytes toward High-Performance Magnesium–Selenium and Magnesium–Sulfur Batteries. *Adv. Energy Mater.* **2017,** *7*, 1602055.

65. Xu, H.; Zhang, Z.; Li, J.; Qiao, L.; Lu, C.; Tang, K.; Dong, S.; Ma, J.; Liu, Y.; Zhou, X.; Cui, G., Multifunctional Additives Improve the Electrolyte Properties of Magnesium Borohydride Toward Magnesium–Sulfur Batteries. *ACS Appl. Mater. Interfaces* **2018,** *10*, 23757-23765.

66. Xu, H.; Zhang, Z.; Cui, Z.; Du, A.; Lu, C.; Dong, S.; Ma, J.; Zhou, X.; Cui, G., Strong anion receptor-assisted boron-based Mg electrolyte with wide electrochemical window and non-nucleophilic characteristic. *Electrochem. Commun.* **2017,** *83*, 72-76.

67. Du, A.; Zhang, Z.; Qu, H.; Cui, Z.; Qiao, L.; Wang, L.; Chai, J.; Lu, T.; Dong, S.; Dong, T.; Xu, H.; Zhou, X.; Cui, G., An efficient organic magnesium borate-based electrolyte with non-nucleophilic characteristics for magnesium–sulfur battery. *Energy Environ. Sci.* **2017,** *10*, 2616-2625.

68. Ha, J. H.; Lee, B.; Lee, M.; Yim, T.; Oh, S. H., Al-compatible boron-based electrolytes for rechargeable magnesium batteries. *Chem. Commun.* **2020,** *56*, 14163-14166.

69. Chellappan, L. K.; Kvello, J.; Tolchard, J. R.; Dahl, P. I.; Hanetho, S. M.; Berthelot, R.; Fiksdahl, A.; Jayasayee, K., Non-Nucleophilic Electrolyte Based on Ionic Liquid and Magnesium Bis(diisopropyl)amide for Rechargeable Magnesium-Ion Batteries. *ACS Appl. Energy Mater.* **2020,** *3*, 9585-9593.

70. Tang, K.; Du, A.; Du, X.; Dong, S.; Lu, C.; Cui, Z.; Li, L.; Ding, G.; Chen, F.; Zhou, X.; Cui, G., A Novel Regulation Strategy of Solid Electrolyte Interphase Based on Anion-Solvent Coordination for Magnesium Metal Anode. *Small* **2020,** *16*, 2005424.

71. Liao, C.; Sa, N.; Key, B.; Burrell, A. K.; Cheng, L.; Curtiss, L. A.; Vaughey, J. T.; Woo, J.-J.; Hu, L.; Pan, B.; Zhang, Z., The Unexpected Discovery of the $Mg(HMDS)_2/MgCl_2$ Complex as a Magnesium Electrolyte for Rechargeable Magnesium Batteries. *J. Mater. Chem. A* **2015,** *3*, 6082-6087.

72. Zhao, X.; Yang, Y.; NuLi, Y.; Li, D.; Wang, Y.; Xiang, X., A new class of electrolytes based on magnesium bis(diisopropyl)amide for magnesium–sulfur batteries. *Chem. Commun.* **2019,** *55*, 6086-6089.

73. Yang, Y.; Qiu, Y.; NuLi, Y.; Wang, W.; Yang, J.; Wang, J., A novel magnesium electrolyte containing a magnesium bis(diisopropyl)amide–magnesium chloride complex for rechargeable magnesium batteries. *J. Mater. Chem. A* **2019,** *7*, 18295-18303.

74. Ha, J. H.; Adams, B.; Cho, J.-H.; Duffort, V.; Kim, J. H.; Chung, K. Y.; Cho, B. W.; Nazar, L. F.; Oh, S. H., A conditioning-free magnesium chloride complex electrolyte for rechargeable magnesium batteries. *J. Mater. Chem. A* **2016,** *4*, 7160-7164.

75. Zhao-Karger, Z.; Liu, R.; Dai, W.; Li, Z.; Diemant, T.; Vinayan, B. P.; Bonatto Minella, C.; Yu, X.; Manthiram, A.; Behm, R. J.; Ruben, M.; Fichtner, M., Toward Highly Reversible Magnesium–Sulfur Batteries with Efficient and Practical $Mg[B(hfip)_4]_2$ Electrolyte. *ACS Energy Lett.* **2018,** *3*, 2005-2013.

Chapter 3

Experimental Methodology

This chapter discusses the rationale behind selecting the electrolyte components to be investigated in the research project as well as details on the electrolytes' base materials. The chapter then explores the fabrication process of various battery components such as the electrolyte and the magnesium battery cathode. Then, the chapter covers the fabrication process of the coin cells and how various characterization methods are conducted. Detailed explanations of the working principles of each characterization method are also discussed.

3.1 The rationale for Electrolyte Design

As indicated in table 3.1.1, the electrolyte consists of a magnesium source, solvent, and additives. The magnesium salts indicated in the table serve as the main source of Mg^{2+} for the electrolytes. Magnesium trifluoromethanesulfonate ($Mg(OTF)_2$, Solvionics, 99.5%), magnesium bis(trifluoromethanesulfonimide) ($Mg(TFSI)_2$, solvionics, 99.5%) and magnesium bis(hexamethyldisilazide) ($Mg(HMDS)_2$, Sigma Aldrich, 97%) are common magnesium salts that has been used to create rechargeable magnesium battery electrolytes. Magnesium perchlorate ($Mg(ClO_4)_2$, Sigma Aldrich, 99%) is known to passivate the magnesium anode but is nevertheless chosen as a point of comparison with other electrolytes. These salts are selected for their commercial availability, making them suitable for mass-scale electrolyte production. Other magnesium compounds such as Grignard reagent or organomagnesium salts are also available in the market but issues such as low oxidative stability and moisture sensitiveness make these compounds unattractive for the magnesium source of magnesium battery electrolyte[1]. The salts explored in this thesis also have appreciably high anodic stability, which is suitable for a high voltage window electrolyte.[2, 3] Table 3.1.2 shows the thermal stability of the salts (except for $Mg(HMDS)_2$). According to the table, the salts are thermally stable for battery application.

THF (Sigma Aldrich, 99.9%, anhydrous), DME (Sigma Aldrich, 99.5%, anhydrous), Diglyme (Sigma Aldrich, 99.5%, anhydrous), Triglyme (Sigma Aldrich, 99%) and Tetraglyme (Sigma Aldrich, 99%) are chosen due to their stability against magnesium metal, high purity. No BHT-inhibitor (alcohol impurities) is in the solvents. As indicated in Table 3.1.3, Diglyme, Triglyme, and Tetraglyme are of primary interest due to their high thermal stability (high boiling point and flash point). Chemical properties such as dielectric constant and viscosity of the solvents affect their ionic conductivity. Generally, viscous solvent inhibits ion mobility in the electrolyte while a high dielectric constant facilitates salt solvation[4, 5]. Hence an ideal electrolyte solvent to achieve high ionic conductivity would be one with high dielectric constant and low viscosity. Therefore, THF may be the most appropriate solvent for increasing the ionic conductivity of the electrolyte due to its high dielectric constant and low viscosity. Glyme-based solvents, however, are more likely to be desirable based on their thermal stability.

$TBABH_4$ (Sigma Aldrich, 95%) is selected due to the ability of BH_4^- to react with H_2O contaminants in the electrolyte. This reaction is expected to prevent the passivation of the anode during the battery cycling process. TBA^+ cation is also known to be stable against the magnesium metal anode.[6] Secondary additives were also included in this study to empirically test their functionality in improving electrolyte performance. $MgCl_2$ (Sigma Aldrich, 99% anhydrous) is selected as a chloride source used to study the effect of chloride on the magnesium plating-stripping electrochemistry and corrosion potential of the current collector. Although the solubility of $MgCl_2$ is low in ether solvents,[7, 8] it is well known that $MgCl_2$ solubility improves upon the addition of other Mg salts such as $Mg(TFSI)_2$,[7] $Mg(OTF)_2$,[9] and $Mg(HMDS)_2$[10].

Table 3.1.1: Various components of the electrolytes and their functions.

Compounds	**Functions**
$Mg(OTF)_2$	Magnesium ion sources
$Mg(ClO_4)_2$	
$Mg(TFSI)_2$	
$Mg(HMDS)_2$	
DME	solvents
THF	
Diglyme	
Triglyme	
Tetraglyme	
$TBABH_4$	Primary additive (moisture scavenger)
$MgCl_2$	Secondary additive (improve electrochemical performance)

Table 3.1.2: Thermal stability of the magnesium salts utilized.

Compounds	Thermal decomposition temperature
$Mg(TFSI)_2$ (ref[11])	> 300°C
$Mg(OTF)_2$(ref[11])	>400°C

$Mg(HMDS)_2$	~
$Mg(ClO_4)_2$(ref[11])	400°C

Table 3.1.3: Physical property of the solvents.

Compounds	**Boiling point**	**Flash point**	**Dielectric constant (20 °C)**	**Dynamic viscosity (mPa s)**
THF	66°C	-15°C	7.6	0.45 (25 °C)
DME (ref.[12])	85°C	5°C	7.2	0.42 (20 °C)
Diglyme (ref.[12])	162°C	51°C	7.4	0.98 (20 °C)
Triglyme (ref.[12])	218°C	111°C	7.62	1.96 (20 °C)
Tetraglyme (ref.[12])	275°C	141°C	-	4.1 (20 °C)

3.2 Electrolyte Fabrication

Before being used, all solvents were dehydrated using zeolite beads (pore size 0.3 nm, size 4-8 mesh) for at least 12 hours to remove water contaminants which are known to passivate magnesium anode in the solvent, thus minimizing the use of any hydride material in the next step. To make the electrolytes, the predetermined amount of magnesium salt and additives are mixed in the dehydrated solvent. Electrolytes were then stirred for at least 12 hours at 40-50 °C before the electrolytes were ready for galvanostatic cycling. All electrolytes were fabricated inside a glovebox with maintained moisture and oxygen contents of $\leq$ 1 ppm and $\leq$ 2.3 ppm respectively.

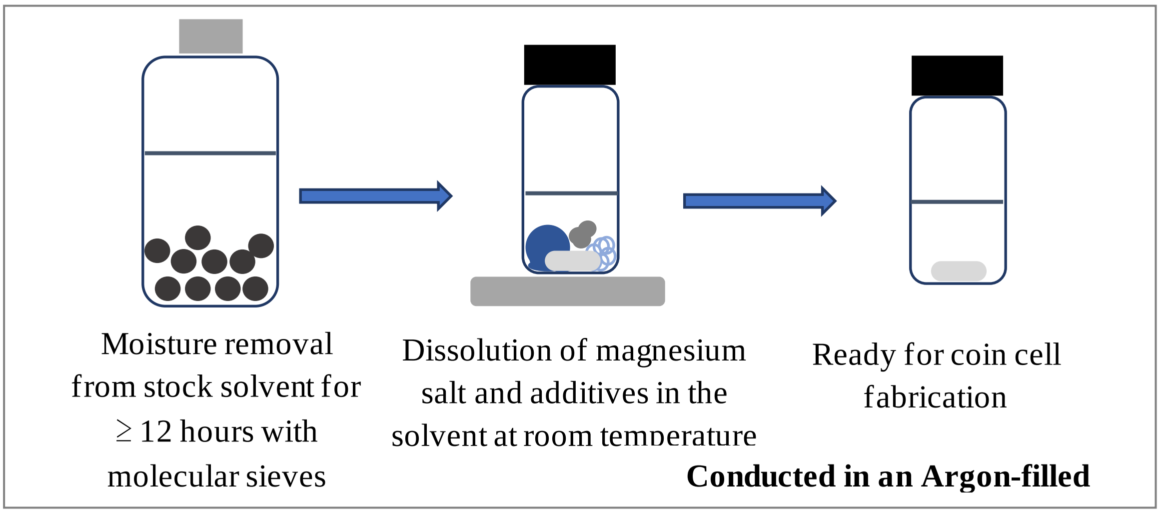

Figure 3.2.1: Electrolyte fabrication steps.

3.3 Cathode fabrication

3.3.1 Short-chain Sulfur/microporous carbon composite cathode

Short-chain sulfur in microporous carbon composite (S/MC) cathode is chosen as a candidate cathode for the battery as it mitigates polysulfide diffusion and has a reduced electrophilicity, thereby making it more compatible with $TBABH_4$ containing electrolyte.[13, 14]

Short-chain sulfur species is generated by a melt-diffusion process into microporous carbon with a pore size smaller than the dimension of S_8 ring.[14, 15] In this thesis, the microporous carbon is generated from ZIF-8 metal-organic framework as previously used in other report[15]. The first step to synthesize the composite is to create the precursor material for the carbon host. Zeolitic Imidazolate Framework 8 (ZIF-8) is used as the precursor, and it was synthesized by a wet chemical method. 30 grams of 2-methyl imidazole was firstly dissolved in 250 mL of methanol. Then, a solution of $Zn(NO_3)_2.6H_2O$ (12.6 gram in 150 mL methanol) was added to the 2-methyl imidazole solution. After being left overnight, the ZIF-8 material was washed and centrifuged four times in methanol before being dried overnight in a vacuum. The ZIF-8 was then carbonized by heat treatment in an argon-filled furnace (argon flow rate of 200 sccm) at 800 °C for 4 hours. During this process, the Zinc in the ZIF-8 material was evaporated out of the material, leaving behind the microporous carbon structure.

To sulfurize the carbon framework, S_8 was mixed thoroughly with the microporous powder (3:1 ratio). The mixed substance was then transferred into an autoclave vial and heated to 160 °C for 16 hours. Excess sulfur was then removed from the fabricated S/MC composite by heating the mixture in an argon-flowed heat furnace at 250 °C for 3 hours. By elemental analysis measurement, the sulfur content of the fabricated composite was determined to be 33.71%.

Sulfur cathode (80% wt. S/MC, 10% wt. Carbon black (CB), 10% wt. poly-vinylidene difluoride (PVDF)) was fabricated by mixing 200 mg of the S/MC composite with 25 mg of Carbon black and PVDF solution (25 mg of PVDF in 1215 mg of N-methyl-2-pyrrolidone (NMP)). The cathode mixture was homogenized twice using Thinky mixer by stirring at 2000 rpm for 3 minutes each time. Defoaming was also conducted using the Thinky mixer for 25 seconds after each homogenization process. The slurry was then coated on carbon-coated aluminium with a controlled slurry thickness of 100 µm. The slurry was then dried off the NMP solvent by heating the foil in a 60 °C oven and was then further dried overnight in a 60 °C vacuum oven to remove any water contamination in the cathode slurry.

3.3.2 S-PAN cathode preparation

S-PAN cathode is also an interesting candidate cathode. The cathode material consists of Sulfur chain species that are chemically bonded to a polyacrylonitrile (PAN) backbone.[16] The chemical bonding of the sulfur in the cathode prevents or mitigates polysulfide drift, thereby improving the capacity retention of S-PAN. [17] Moreover, the previous report indicates that the S-PAN cathode is compatible with nucleophilic BH_4^-,[17] unlike S_8. Thus, the S-PAN cathode is a prospective cathode to explore.

The cathode material was synthesized according to a previously published work.[16] S_8 was mixed with polyacrylonitrile polymer (PAN) in a weight ratio of 5:1. The mixture was then ground and heated to 450 °C to facilitate the chemical reaction between S_8 and PAN. The heating process was conducted by applying a heat ramp from room temperature to 450 °C with a ramp rate of 10 °C min^{-1}. The heating process at 450 °C was conducted for 6 hours before the material was cooled down to room temperature.

The S-PAN composite was then made into a slurry to be coated on a carbon-coated aluminium foil. The slurry is made by mixing S-PAN active material (70% wt), carbon black (20% wt), and CMC binder (10% wt) in an NMP solvent. The carboxymethyl cellulose (CMC) binder was firstly dissolved in water (5%wt solution) before being mixed with THE NMP slurry. The slurry was then coated on a carbon-coated aluminium foil and dried in a 70 °C oven.

3.3.3 Copper Sulfide nanomaterial cathode

Copper (II) Sulfide is chosen as a candidate cathode material due to its high theoretical capacity and generally high activity with magnesium electrolytes. CuS cathode material was synthesized by a wet-chemical process. 2.33 g of $Cu(NO_3)_2.2.5H_2O$ was firstly dissolved in 80 mL of Ethylene Glycol: DI water solution (3:1 volume ratio). While the $Cu(NO_3)_2$ solution was heated to 60 °C, 1.29495 g of $Na_2S_2O_3.5H_2O$ was dissolved in 80 ml of Ethylene Glycol: DI water solution (3:1 volume ratio). $Na_2S_2O_3$ solution was then added to the heated $Cu(NO_3)_2$ solution and the reaction was let to occur for 30 minutes at 60°C. The solution was then let to cool down and after 3 hours, the CuS product was separated from the mixture by centrifugation. The product was then washed 3 times with DI water and once more with ethanol. The CuS powder was then let to dry in a 60 °C vacuum oven for at least 12 hours.

The cathode slurry (80% wt. CuS, 10% wt. CB, 10% wt. PVDF) was fabricated by mixing 204.6 mg of CuS with 25.575 mg of Carbon black and PVDF solution (25.575 mg of PVDF in 1088 mg in NMP). The CuS cathode slurry was then homogenized using a Thinky mixer by stirring at 2000 rpm for 3 minutes (twice) followed by a 25 seconds defoaming process at 2000 rpm for 25 seconds after each homogenization process. The slurry was then coated on a carbon-coated aluminium foil with a controlled thickness of 100 μm. The slurry was then dried off the NMP solvent a 60 °C. The film was then vacuum dried a 60 °C for at least 12 hours. The average loading of the CuS cathode is 1.18 mg cm^{-2}.

3.3.4 Mo_6S_8 cathode

Mo_6S_8 is a commonly used material active material for rechargeable magnesium battery cathode due to high magnesium ion mobility in the crystal structure. This is due to the existence of Mo_6 clusters which are able to screen the highly charge dense Mg^{2+} ion. Hence, despite its low gravimetric capacity (129 mAh g^{-1}) and low operating potential

(1.1 V vs. Mg/Mg^{2+}), it is still commonly used to test rechargeable magnesium battery electrolytes.

Mo_6S_8 was produced from $Cu_2Mo_6S_8$ from a copper leaching process. The process was conducted by mixing the $Cu_2Mo_6S_8$ into a 6 M HCl solution. The solution suspension was then stirred (200 rpm) for 24 hours while being aerated by flowing air into the suspension during the whole process. The Mo_6S_8 product is then centrifuged from the suspension and washed several times with DI water until the waste liquid used to wash the material has a neutral pH. Then, the solid product was washed once more with ethanol and dried for 24 hours in an oven. The active material is then mixed with CNF to increase the conductivity of the cathode material using a ball-milling method. The Mo_6S_8: CNF ratio is 80:20 by weight.

The cathode slurry was coated on prepared on two types of current collectors (stainless-steel or aluminium). The cathode slurry (64% wt. Mo_6S_8, 16% CNF, 10% wt. CB, 10% wt. PVDF) was made by mixing 500 mg of Mo_6S_8-CNF mixture and 62.5 mg of carbon black into a PVDF solution in NMP (62.5 mg of PVDF in 2600 mg of NMP). The mixture was then homogenized using a thinky mixer for 3 minutes at 2000 rpm, followed by 10 seconds of slurry defoaming process. The slurry was then coated on carbon-coated aluminium and stainless-steel foils. The electrodes were then dried for 24 overnight in a vacuum oven.

3.4 Coin Cells Preparation

Each cell is composed of Mg foil as the counter and the reference electrode, a glass fiber separator, and a cathode (for a full-cell), carbon-coated aluminium (for an asymmetric half-cell configuration), or another magnesium foil (for a symmetric half-cell configuration). Coin cell 2032 parts were used to construct all half-cell configurations for galvanostatic tests. They were sonicated in an acetone bath before being dried to clean the cell parts.

Before cell assembly, both surfaces of the magnesium foil were polished inside the glovebox with moisture and O_2 content of ≤ 1 ppm and ≤ 1 ppm respectively before being cut into a circular electrode with a diameter of 12.7 mm (⌀12.7 mm). This was done to prevent anode passivation and ensure good electrical contact with the cell casing.

To prepare the aluminum electrode for the asymmetric half-cell, an aluminum-coated carbon foil was cut into circular disk electrodes (⌀11.28 mm), which were then dried of moisture in a 60 °C vacuum oven for 24 hours before use.

Glass fiber separators were prepared by cutting a glass fiber sheet into circular separators (⌀16 mm). These separator disks were then dried at 150°C for 4 hours before being transferred to the glovebox to be used. Graphene oxide-coated separators are prepared for full-cell galvanostatic cycling. Graphene oxide was added to the Mg//CuS cell mainly to combat several issues that were found in the cell if graphene oxide was not added in. These issues include battery overcharge (which is likely due to electrolyte oxidation) and capacity fade (potentially due to Cu ion dissolution in the electrolyte). Previous publications indicate that CuS may produce polysulfide species that could potentially dissolve into the electrolyte and cause capacity fading.[18, 19] [19]The functional groups of Graphene oxide have been shown to bind to polysulfide species and may prevent cathode dissolution in the electrolyte.[20]

The separator was prepared by coating graphene oxide suspension (Graphenea, 0.4%wt in water) on the glass fiber. The separator is then dried for several minutes at 80 °C to dry. Then the glass fiber separator is further dried in a vacuum oven at 60 ℃ for overnight before being used. The average loading of the graphene oxide coating is 0.2 mg cm^{-2}. For each cell, 75 microliters of electrolytes are used.

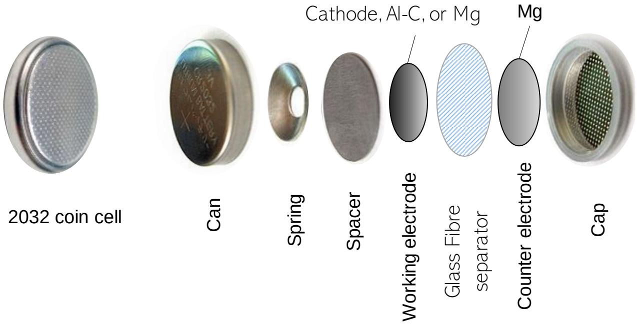

Figure 3.4.1: Internal structure of the coin cell.

3.5 Characterization Method

Table 3.5.1: Various characterization utilized in this project, along with their types and purposes.

Characterization methods	types	Purpose

Galvanostatic cycling	Electrochemical characterization	To measure full-cell and half-cell overpotential and Coulombic efficiency.
Ionic conductivity	Electrochemical characterization	To measure the resistance of the electrolyte.
LSV	Electrochemical characterization	Utilized to measure the onset potential of the current collector corrosion or electrolyte oxidation.
Multistep Chronoamperometry	Electrochemical characterization	Utilized to measure the onset potential of the current collector corrosion or electrolyte oxidation.
XRD	Material characterization	Crystal structure characterization of electrochemically deposited substance.
SEM	Material characterization	Characterization of magnesium deposit morphology on copper and aluminium electrode.
EDS	Chemical Analysis	Chemical identification of deposit on copper electrode.
XPS	Chemical analysis	Identification of chemical species on the magnesium anode surface.
CHNS Elemental analysis	Chemical analysis	Identification of Sulfur %wt. content in the S/MC composite
Raman	Chemical structure analysis	Identification of chemical bonds in the electrolyte solution.
SCXRD	Chemical structure analysis	Identification of magnesium complex in the electrolyte solution.

3.5.1 Galvanostatic cycling

3.5.1.1 Mg deposition and dissolution reversibility measurement

To characterize the Coulombic efficiency of magnesium deposition and dissolution of each electrolyte, galvanostatic cycling of asymmetric half-cell (Mg//Al-C) made with the electrolyte of interest was done. The galvanostatic method is chosen due to its higher accuracy in determining Coulombic efficiency, as compared to the commonly used Cyclic voltammetry method.[21] After assembly, the coin cells were rested at room temperature for 3 hours to ensure the electrodes and separator inside the cells are fully wetted with the electrolyte. The galvanostatic cycling started with a negative constant current of 0.5 mA cm^{-2} for a period until the desired plating magnesium plating capacity was reached (0.5 mAh cm^{-2}), followed by magnesium stripping from the working electrode that was stopped once the electrode reached a cut-off potential of 1.2 V. The magnesium deposition and dissolution processes were repeated for 1000 cycles for each coin cell unless an internal short-circuit occurred. The Coulombic efficiency in each cycle number "n" is calculated based on the formula:

$$\text{CE (n)}=\frac{\text{magnesium stripping capacity (n)}}{\text{magnesium deposition capacity (n)}}\times 100\%$$

On the other hand, the overpotential of magnesium deposition/dissolution on the working electrode can be derived by measuring the stabilized potential shift against the magnesium counter electrode for each deposition/dissolution process.

3.5.1.2 Mg deposition and dissolution overpotential measurement

To characterize the overpotential of magnesium deposition and dissolution of each electrolyte, galvanostatic cycling in a symmetric half-cell (Mg//Mg configuration) was used. After assembly, the coin cell was rested at room temperature for 3 hours to ensure the electrodes and separator inside the cells are fully wetted with the electrolyte. Each test cycle started with a negative constant current of 0.5 mA cm^{-2} for 1 hour, followed by the application of a positive constant current of 0.5 mA cm^{-2} for 1 hour. The galvanostatic cycling proceeds until the 1000 cycle was finished or when the cell has short-circuited.

3.5.1.3 Full-cell galvanostatic cycling

To test if the electrolyte could be used in an actual battery, galvanostatic cycling is also conducted for the electrolytes using Mg//CuS, Mg//S-MC, and Mg//Mo_6S_8 full-cells. Before being cycled, the cells are rested for 6 hours at OCV before being cycled using the galvanostatic method between a low and high cut-off potential. Details of the cycling process are shown on the full-cell data presented. To calculate the Coulombic Efficiency of the full-cell in each cycle number "n" is calculated by the formula:

$$\text{CE (cycle number n)}=\frac{\text{discharge capacity(n)}}{\text{charge capacity (n-1)}}\times 100\%$$

The Coulombic efficiency of the cell is used to measure the amount of discharge capacity that is retained in proportion to the initial charge capacity. Since the battery tested is in the charged state after fabrication. The charge process is not present in the first cycle and the Coulombic efficiency of the full-cell is not calculated for the first cycle.

3.5.2 Potential window measurement

Potential window measurements were done in a three-electrodes setup. Polished magnesium strips are used as the reference and counter electrode while a thick aluminium plate (Alfa Aesar) or stainless-steel foil (SS316, MTI) was used for the working electrode. To measure the anodic stability of an electrolyte, about 1 ml of the electrolyte solution was used to dip all three electrodes into it. After it was ensured that there is no short circuit between the electrodes. Open circuit potential was measured for each cell before linear sweep voltammetry (LSV) measurement or multi-step chronoamperometry measurement.

3.5.2.1 Linear sweep voltammetry measurement

Linear Sweep Voltammetry measurement was conducted using a Gamry potentiostat and a Gamry instrument program. After 5 seconds of equilibration time, the working electrode potential was increased from its open circuit potential at a constant increment of 5 mV per second until its potential reaches 5 V against the magnesium reference electrode. During this potential sweep, the current applied to the working electrode was measured. After the experiment, the active surface of the working electrode was measured by measuring the area of the electrode that has changed due to residue of electrolyte decomposition and the corrosion process.

3.5.2.2 Multi-step chronoamperometry measurement

Once the onset of corrosion or electrolyte decomposition was determined, chronoamperometry measurement can be done to determine the anodic limit of the electrolyte more accurately. To conduct the measurement process in a 3-electrodes cell, several constant potential steps were applied to the working electrode for a fixed duration while the current applied to the working electrode was measured. After the experiment, the active surface of the working electrode was measured by measuring the area of the electrode that has changed due to residue of electrolyte decomposition and the corrosion process.

3.5.3 Ionic conductivity measurement

3.5.3.1 Working principle of ionic conductivity measurement

The measurement of the ionic conductivity of an electrolyte, typically, employs a similar method as that for EIS measurement. Generally, a high-frequency AC voltage perturbation is applied to the electrolyte. As the impedance contribution of charge transfer processes is negligible at high AC frequency, most of the resistance in the cell is attributed to the electrolyte resistance, which is inversely proportional to the conductivity of the electrolyte. Moreover, AC current also prevents any change in the chemical composition of the electrolyte due to electrolyte oxidation or reduction reaction.[5] Generally, the relationship between ionic conductivity (σ), Electrode polarization potential (V), Current (I), and the cell constant (K, determined by the probe geometry) is:[5]

$$\sigma = K\frac{I}{V}$$

The conductivity of the electrolyte, therefore, can be determined based on the relationship between the AC current and the voltage difference of the electrodes. The ionic conductivity probe used in this study was a 4-electrode probe. The device set-up minimizes inaccuracy in conductivity measurement by eliminating the polarization effect on the ionic conductivity measurement. Polarization happens due to charge transfer reactions that happen on the electrodes when current is applied to the electrodes. The probe minimizes this effect by separating the perturbing electrode and the measurement electrode. By doing so, the polarization on the perturbing electrode does not affect the potential measurement associated with the electrolyte resistance.

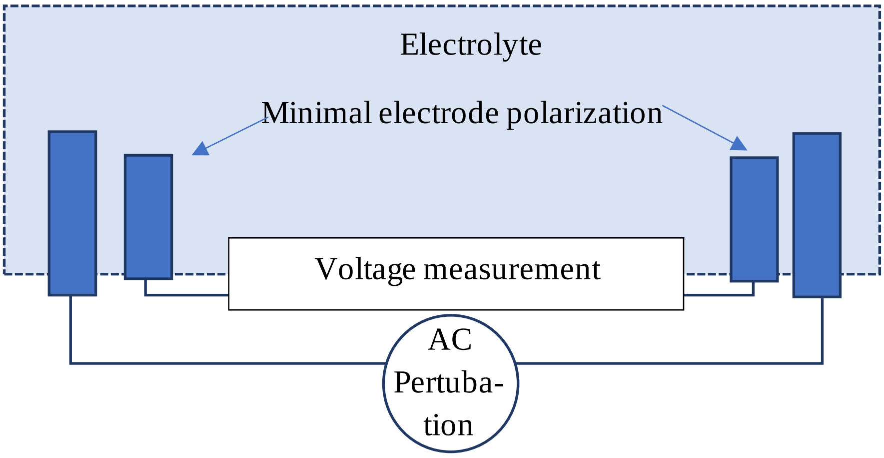

Figure 3.5.3.1: Electrode structure for ionic conductivity measurement.

3.5.3.2 Ionic conductivity measurement method

The ionic conductivity of the electrolyte was measured by using Fisherbrand Accumet AB200 with a 4-cell ionic conductivity probe. Measurement was done inside the glovebox and the probe was firstly washed with DME before and after the measurement of electrolyte. Conductivity measurements were conducted three times and the average measurement was taken as the electrolyte conductivity.

3.5.4 EIS measurement

3.5.4.1 Working principle of the EIS characterization

EIS characterization was conducted on symmetric magnesium cells to characterize the electrochemical processes in the battery. In particular, the method is able to separate the internal resistance of the cell into various components such as electrolyte resistance, interfacial resistance, charge-transfer resistance of the electrodes, and diffusional impedance of the electroactive species.[22] The method generally relies on measuring the current response of an electrochemical cell upon the application of a low amplitude AC voltage. By measuring the current amplitude and phase shift of the current response, the impedance of the electrochemical cell at each specific frequency can be determined. The impedance is a complex function analogue of the cell resistance, and it can be represented as

$$Z(\omega)=\frac{|V|e^{i\omega t}}{|I|e^{i\omega t-\theta}}$$

Wherein $|V|\,e^{i\omega t}$ and $|I|e^{i\omega t-\theta}$ is the complex function representation of the perturbing AC voltage and the corresponding AC current response wave respectively[22]. For the characterization of battery electrochemistry, it is useful to represent the impedance measurement across various frequencies as a bode plot, wherein the real and imaginary components of the impedance are plotted from low to high frequency. The figure below exemplifies a typical Nyquist plot that can be obtained after an EIS measurement of an electrode.

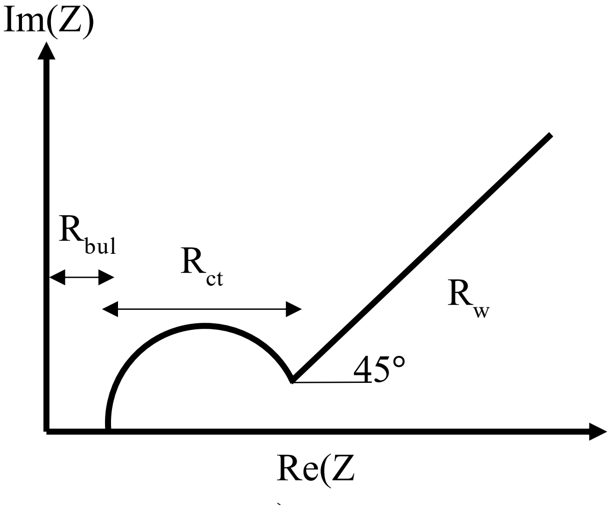

Figure 3.5.4.1: Idealized Nyquist plot of an electrode.

Typically, the Nyquist plot of the EIS measurement will provide several important characteristics of the cell. This includes the bulk resistance of the cell at high frequency, which constitutes the electrolyte, current collector, and separator resistance[22, 23]. The Nyquist plot would also show a semicircle profile which represents the contribution of the electrode double-layer capacitance and charge transfer resistance along with a linear profile which represents the contribution of the diffusion impedance of the electroactive species.[22, 23]

3.5.4.2 EIS characterization method

EIS measurement was conducted to observe changes in the cell impedance after a given number of cycles magnesium plating and stripping in the cell. The electrochemical cell used for the characterization is a symmetric Mg//Mg cell. Each EIS measurement was conducted with alternating current with a frequency range of 10 MHz to 1 mHz with a perturbation potential of 7 mV (V_{rms} 5 mV) in the OCV state. Before the first EIS measurement, which was conducted before magnesium plate and strip cycling, the cell is rested for three hours to allow the OCV potential to stabilize. Subsequently, 10 minutes of cell rest was implemented before additional EIS measurements to observe the cell impedance after cell cycling.

3.5.5 Material characterization

3.5.5.1 XRD

3.5.5.1.1 XRD working principle

X-ray diffraction characterization of material is a well-developed method to identify unknown material or to confirm the identity of a sample. The main component of the instrument consists of an X-ray source, sample stage, and X-ray detector. The characterization technique relies on the X-ray Bragg's diffraction phenomenon.[24] X-ray Bragg's diffraction happens when a coherent X-ray photon is reflected by the atomic planes of crystalline material. Each crystalline material has its own set of crystal planes, and each plane has a unique interplanar spacing. Bragg's diffraction is a constructive diffraction phenomenon in which the X-ray photons which are reflected by the crystal plane are in phase with one another. The figure helps in elaborating the geometric constraint of Bragg's diffraction in a crystalline material.

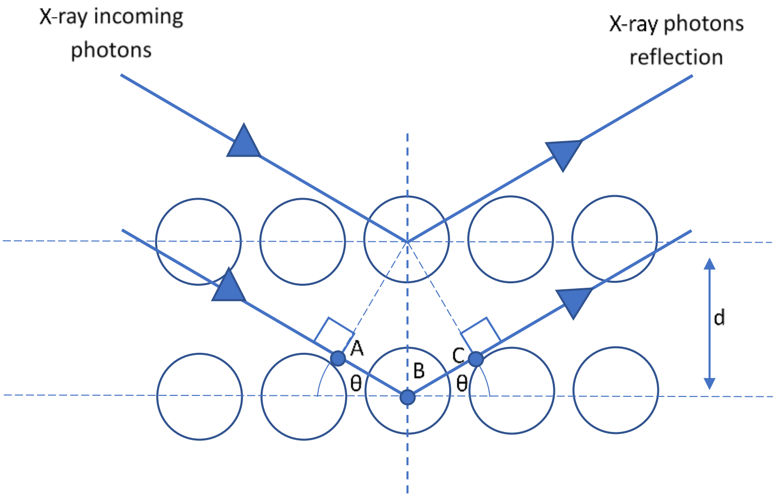

Figure 3.5.5.1.1: The geometric description of Bragg's diffraction.

For constructive interference to happen, the photons reflected by the upper and lower plane must be in phase. Due to this constraint, the length of path A to B to C must be equal to the multiple of the photon's wavelength. In other words, the equation stated below must hold for Bragg's diffraction to occur.

$$AB+BC=2d\sin(\theta)=n\times\lambda$$

θ (reflection angle)

d (interplanar distance)

n (integer numbers 1, 2, 3, …)

λ (photon wavelength)

Consequently, given that the wavelength of the photon source is fixed, Bragg's diffraction can only happen at specific series of θ (i.e. angle of reflection) values. Moreover, the series of θ values are dependent on the crystal structure and constituents of the material, as the interplanar distances of the plane are determined by both factors. Hence, by measuring the diffraction intensity of the X-ray radiation across various θ values, the identity of the material can be determined.

3.5.5.1.2 XRD characterization method

To corroborate that an electrolyte enables Mg crystal deposition, ex-situ material characterization (XRD) was done on a nickel foil. The nickel substrate was firstly deposited with magnesium using the magnesium battery electrolyte with a constant deposition current density of 0.5 mA cm^{-2} for 5.5 hours in the glovebox. The Nickel sample was then washed with DME, wrapped with Kapton tape (to prevent contact with oxygen) before being brought outside of the glovebox.

XRD was then conducted on Bruker D8 Advance diffractometer using Cu Kα X-Ray source (1.54 Å). Diffraction data were collected from 30 to 60° with a step size of 0.02°. X-Ray Diffraction spectrum of the sample was then fitted to that of nickel and magnesium crystal obtained from the JCPDS database. Confirmation of CuS successful synthesis was also done on the synthesized CuS nanomaterial using the same instrument.

3.5.5.2 SEM

3.5.5.2.1 SEM working principle

Electron microscopy and EDS analysis are conducted in a FE-SEM microscope. Electron microscopy is used to analyze the morphology of the sample. Electron microscope offers a better resolution power compared to an optical microscope and is better suited to study the morphology of nanomaterials or the crystal morphology at extremely high magnification. In this thesis, scanning electron microscopy is used. The sample is kept under a high vacuum environment during the analysis process. The instrument works by irradiating the sample with a primary highly accelerated electron beam. Upon colliding with the sample, the primary electron beam may collide with the outer electron of the sample. This collision results in an inelastic collision whereby some of the energy of the primary electron is transferred to the sample's electron. This process generates the secondary electron beam. By collecting the Secondary electron signal across the sample, surface contours of the sample can be generated.[25]

3.5.5.2.2 SEM characterization

SEM characterization was conducted to CuS and magnesium films to identify the morphology of the substance. The characterization was conducted inside FE-SEM JSM 6700F with an acceleration potential of 5 kV and a chamber pressure of 5.14 10^{-4} Pa.

3.5.6 Chemical characterization

3.5.6.1 EDS

3.5.6.1.1 EDS working principle

Energy-dispersive X-ray spectroscopy (EDS) is conducted by using an electron microscope. This characterization is conducted to identify the elemental composition of a sample. The characterization technique relies on the X-ray fluorescence phenomenon.[26] During the irradiation process of the sample with a high-energy primary electron beam. Sometimes, the primary electron beam transferred its energy to the core electron of the atoms of the sample. This process excites the electron, thereby freeing it from the atom, creating an empty orbital in the excited atom. The state of the atom, therefore, becomes unstable. To reach a lower energy state, one of the electrons at the outer shell of the atom undergoes a relaxation process to fill the empty core-level energy state. During this relaxation process, an X-ray photon is emitted. The X-ray photon energy equals the difference between the binding energy of the empty orbital with the binding energy of the initial state of the relaxing electron [B.E. (1)-B.E. (2)].

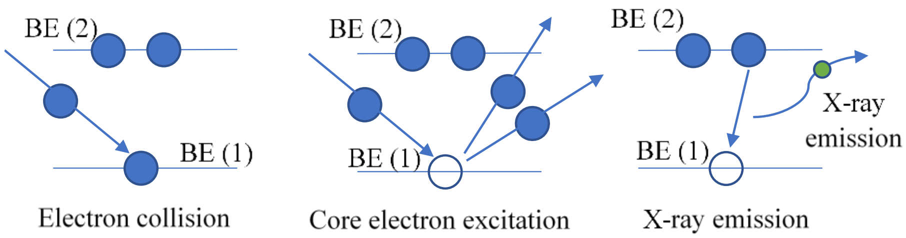

Figure 3.5.6.1.1: Mechanism of Characteristic X-ray generation.

As the emitted X-ray is dependent on the binding energy of the electrons in the atom, the emitted X-ray spectrum functions as a characteristic signal of the elements in the sample. EDS sample, therefore, serves as an elemental analysis method to identify the constituents of the sample. Furthermore, the intensity of a characteristic X-ray also correlates positively with the concentration of the source elements. Thus, EDS analysis also provides a quantitative analysis of the sample composition.

3.5.6.1.2 EDS characterization of magnesium film

EDS chemical analysis was done using FE-SEM JEOL 7600F (acceleration potential of 15 kV) coupled with Oxford Technologies X-ray detector. This analysis was conducted to gain information regarding the chemical identity of the deposit, thus giving additional evidence for magnesium crystal deposition. The samples were created by depositing 0.5 mAh cm^{-2} of magnesium on carbon-coated aluminium in asymmetric half-cells. A piece of Celgard film was placed between the analyte sample and the glass fiber separator to prevent the magnesium sample from sticking to the glass fiber separator. The aluminium foils were then extracted from the cell, washed with DME, and then dried inside an Argon-filled glovebox before being analyzed.

3.5.6.2 XPS

3.5.6.2.1 XPS working principle

XPS measurement is a surface analysis technique conducted to analyze the surface chemical composition of a conductive sample. The primary components of the XPS instrument are its monoenergetic X-ray Source, electron analyzer, and photoelectron energy detector.

The basic working principle of the XPS characterization is based on the photoelectron emission process.[27] The photoelectron emission process is initiated when the sample is irradiated with X-ray radiation. During the irradiation process, some of the X-ray photons will encounter electrons of the atom constituents of the sample. If the energy of the photon is larger than the binding energy of the electron, an excitation process will occur whereby the electron is freed from the atom. Some of the excited electrons will also escape the sample as it gains some kinetic energy from the photon. The XPS instrument determines the initial binding energy of the excited electrons by measuring the kinetic energy of the electron. By using the equation stated below, the initial binding energy of the photoelectron can be determined.

$$\text{K.E.} = \text{h.v.} - \text{B.E.} - \Phi$$

K.E. (Kinetic energy of the excited electron)

h.v. (photon energy)

B.E. (initial binding energy of the excited electron)

Φ (work function of the sample/ energy required to remove an electron from the sample to the vacuum outside of the sample)

The electron energy analyzer works by separating the photoelectron signals according to their kinetic energy or velocity. The analyzer employed a magnetic field to do this process. As the electron passes through the magnetic field, it will experience a Lorentz force perpendicular to its velocity. Due to this force, the photoelectron will move into a semicircular motion in the analyzer. Furthermore, the radius of the photoelectron's arching path will depend on its velocity (which in turn is determined by its kinetic energy). Thus, the analyzer is able to separate the photoelectron signal based on its kinetic energy. After passing through the analyzer, the photoelectron will then hit the detectors.

Based on the binding energy spectrum generated by the measurement, elemental constituents of the sample can be determined. Furthermore, the chemical bonds and oxidation state of the elements can also be inferred as the unique chemical state of an element determines its binding energy. The quantitative elemental composition of the sample can also be inferred from the intensity of the photoelectrons from each element.

3.5.6.2.2 XPS analysis of magnesium anode

In this thesis, XPS characterization is used to identify the chemical composition of the cycled magnesium anode. To create the magnesium anode-electrolyte interphase to be analyzed, a symmetric Mg//Mg cell was cycled 20 times with a current density of 0.5 mA cm^{-2}. A piece of Celgard film was placed between the analyte sample and the glass fiber separator to prevent the magnesium sample from sticking to the glass fiber separator. The magnesium foils were then extracted from the cell, washed with DME, and then dried inside an Argon-filled glovebox. Samples were then mounted on a sealed XPS holder and transferred to the XPS loading chamber. After vacuuming the samples in the loading chamber for ~4 hours to remove the solvent. The samples were characterized with the Thermo Scientific Theta Probe Angle-Resolved Spectrometer instrument. To analyze the chemical state of the elements at various thicknesses, Argon etching was done on the sample using a 2 μA argon beam accelerated using a 3 kV potential difference. The XPS spectrums are charged referenced to the Mg^0 peak at 49.8 eV and each peak is modeled using Gaussian/Lorentzian mixture of 70:30.

3.5.6.3 CHNS elemental analysis

Elemental CHNS analysis was conducted to analyze the sulfur content of S/MC and S-PAN cathode. The measurements are conducted using a Thermo Scientific Flash 2000 analyzer. The instrument was calibrated using sulphanilamide analytical standard (Elemental Microanalysis, UK). The cathode material was analyzed before being used for slurry fabrication. For the elemental analysis measurement, each sample was prepared in tin foil capsules.

3.5.6.4 Raman spectroscopy

3.5.6.4.1 Raman working principle

Raman spectroscopy is a characterization technique often used to assist in identifying chemical groups in a sample. Typically, a laser source is used to irradiate the sample during the measurement process. The basic principle of the characterization technique relies on the Raman-stokes and Raman anti-stokes scatterings of photons by molecules. Raman-stokes scattering happens due to an inelastic collision process between a molecule in its ground state and a photon.[28] The process happens when the energy of the photon is sufficiently high to induce vibrations of certain chemical bonds in the molecule. Upon collision, some of the photon energy is transferred to the molecule to excite a vibration mode. The scattered photon, therefore, would have reduced energy, and would therefore redshift its wavelength. Conversely, a Raman Anti-stokes scattering process may also happen when a photon collides with a molecule in its excited state. In this collision process, the vibration energy of the molecule will be transferred to the photon, thereby increasing its energy and blueshift its wavelength. By measuring the spectrum of the scattered laser lights, the energy shift (or wavenumber shift) of the scattered photons can be determined. This information leads to identification in the vibrational energy or wavenumber of the chemical bonds in the sample. Identification of the chemical bonds (chemical groups) in the sample can therefore be determined from the wavenumber of the chemical bonds. It is important to note that not all chemical bonds are Raman active. In particular, Raman spectroscopy is best used to excite symmetric vibration and non-polar bonds and may provide little information on unsymmetric vibration and polar groups in the molecules. [28]

3.5.6.4.2 Raman spectroscopy procedure

Electrolyte samples were analyzed by Raman Spectroscopy to identify the chemical bondings which exist in the electrolyte. This spectroscopy helps in identifying the chemical structure of the electroactive species in the electrolyte. Each electrolyte sample was made in the glovebox and then sealed in a small glass vial using parafilm to prevent the samples from being contaminated by the outside atmosphere. The samples were then analyzed using RENISHAW invia Raman microscope using a primary laser beam with a wavelength of 532 nm.

3.5.6.5 Single Crystal XRD analysis

The single-crystal XRD was conducted to analyze the chemical structure of the electroactive species in the electrolyte. The working principle of the instrument is described in §3.5.4.1.

The electrolyte firstly needs to be crystallized before being analyzed. The crystal was grown from a saturated $Mg(HMDS)_2$ solution. The solution is made in an argon-filled glovebox by mixing 577.4 mg of $Mg(HMDS)_2$ with 1 ml of DME (~1.67 M). After the dissolution process, the stir bar used during the stirring process was removed and the electrolyte was let to grow crystal for 1.5 months. The crystal vial was sealed with parafilm before being transferred to outside the glovebox.

The XRD spectrum of the crystal was obtained by using a Bruker D8 Quest diffractometer. The experiment is conducted at 100 K with a Mo Kα X-ray source. The collected diffraction frames were interpreted using the SAINT software and absorption correction is conducted using the SADABS software. The structure of the crystal was solved using the direct methods and refined with the full-matrix least-squares analyses on F2 (SHELXL-2018/3). Refinement of non-hydrogen atoms was conducted anisotropically. The positions of the hydrogen atoms were determined geometrically and allowed to ride on their respective parent carbon atoms before the final cycle of least-squares refinement.

References

1. Bucur, C. B.; Gregory, T.; Oliver, A. G.; Muldoon, J., Confession of a Magnesium Battery. *J. Phys. Chem. Lett.* **2015,** *6*, 3578-3591.
2. Lau, K.-C.; Seguin, T. J.; Carino, E. V.; Hahn, N. T.; Connell, J. G.; Ingram, B. J.; Persson, K. A.; Zavadil, K. R.; Liao, C., Widening Electrochemical Window of Mg Salt by Weakly Coordinating Perfluoroalkoxyaluminate Anion for Mg Battery Electrolyte. *J. Electrochem. Soc.* **2019,** *166*, A1510-A1519.
3. Zhao-Karger, Z.; Zhao, X.; Fuhr, O.; Fichtner, M., Bisamide Based Non-Nucleophilic Electrolytes for Rechargeable Magnesium Batteries. *RSC Adv.* **2013,** *3*, 16330-16335.
4. Bard, A. J.; Faulkner, L. R., *Electrochemical Methods: Fundamentals and Applications*. Second Edition ed.; John Wiley & Sons, Inc.: New York, 2001; p 864.
5. Girault, H. H., *Analytical and physical electrochemistry*. EPFL press: 2004.
6. Gofer, Y.; Chusid, O.; Gizbar, H.; Viestfrid, Y.; Gottlieb, H. E.; Marks, V.; Aurbach, D., Improved Electrolyte Solutions for Rechargeable Magnesium Batteries. *Electrochem. Solid-State Lett.* **2006,** *9*, A257.

7. Shterenberg, I.; Salama, M.; Yoo, H. D.; Gofer, Y.; Park, J.-B.; Sun, Y.-K.; Aurbach, D., Evaluation of $(CF_3SO_2)_2N^-$ (TFSI) Based Electrolyte Solutions for Mg Batteries. *J. Electrochem. Soc.* **2015,** *162,* A7118-A7128.

8. Küpers, V.; Weintz, D.; Mück-Lichtenfeld, C.; Bieker, P.; Winter, M.; Kolek, M., Approaching Electrochemical Limits of Mg x Cl y z+ Complex-Based Electrolytes for Mg Batteries by Tailoring the Solution Structure. *J. Electrochem. Soc.* **2020,** *167,* 160505.

9. Nguyen, D.-T.; Eng, A. Y. S.; Ng, M.-F.; Kumar, V.; Sofer, Z.; Handoko, A. D.; Subramanian, G. S.; Seh, Z. W., A High-Performance Magnesium Triflate-based Electrolyte for Rechargeable Magnesium Batteries. *Cell Rep. Phys. Sci.* **2020,** *1,* 100265.

10. Liao, C.; Sa, N.; Key, B.; Burrell, A. K.; Cheng, L.; Curtiss, L. A.; Vaughey, J. T.; Woo, J.-J.; Hu, L.; Pan, B.; Zhang, Z., The Unexpected Discovery of the $Mg(HMDS)_2/MgCl_2$ Complex as a Magnesium Electrolyte for Rechargeable Magnesium Batteries. *J. Mater. Chem. A* **2015,** *3,* 6082-6087.

11. Kubota, K.; Matsumoto, H., Preparation of Magnesium Salts Composed of Perfluoro Anions and These Electrochemical Behaviors in Molten Salts. *J. Electrochem. Soc.* **2020,** *167,* 020541.

12. Tang, S.; Zhao, H., Glymes as versatile solvents for chemical reactions and processes: from the laboratory to industry. *RSC Adv.* **2014,** *4,* 11251-11287.

13. Wang, W.; Yuan, H.; NuLi, Y.; Zhou, J.; Yang, J.; Wang, J., Sulfur@microporous Carbon Cathode with a High Sulfur Content for Magnesium–Sulfur Batteries with Nucleophilic Electrolytes. *J. Phys. Chem. C* **2018,** *122,* 26764-26776.

14. Du, H.; Zhang, Z.; He, J.; Cui, Z.; Chai, J.; Ma, J.; Yang, Z.; Huang, C.; Cui, G., A Delicately Designed Sulfide Graphdiyne Compatible Cathode for High-Performance Lithium/Magnesium–Sulfur Batteries. *Small* **2017,** *13,* 1702277.

15. Chen, Y.-M.; Liang, W.; Li, S.; Zou, F.; Bhaway, S. M.; Qiang, Z.; Gao, M.; Vogt, B. D.; Zhu, Y., A nitrogen doped carbonized metal–organic framework for high stability room temperature sodium–sulfur batteries. *J. Mater. Chem. A* **2016,** *4,* 12471-12478.

16. Eng, A. Y. S.; Nguyen, D.-T.; Kumar, V.; Subramanian, G. S.; Ng, M.-F.; Seh, Z. W., Tailoring binder–cathode interactions for long-life room-temperature sodium–sulfur batteries. *J. Mater. Chem. A* **2020,** *8,* 22983-22997.

17. Wang, P.; Trück, J.; Niesen, S.; Kappler, J.; Küster, K.; Starke, U.; Ziegler, F.; Hintennach, A.; Buchmeiser, M. R., High-Performance Magnesium-Sulfur Batteries Based on a Sulfurated Poly(acrylonitrile) Cathode, a Borohydride Electrolyte, and a High-Surface Area Magnesium Anode. *Batter. Supercaps* **2020,** *3*, 1239-1247.

18. Feng, C.; Zhang, L.; Yang, M.; Song, X.; Zhao, H.; Jia, Z.; Sun, K.; Liu, G., One-Pot Synthesis of Copper Sulfide Nanowires/Reduced Graphene Oxide Nanocomposites with Excellent Lithium-Storage Properties as Anode Materials for Lithium-Ion Batteries. *ACS Appl. Mater. Interfaces* **2015,** *7*, 15726-15734.

19. Wu, M.; Zhang, Y.; Wu, H.; Qin, A.; Li, X.; Shen, J.; Chen, Z.; Cao, S.-a.; Li, T.; Xu, F., Cu9S5 Nanoflower Cathode for Mg Secondary Batteries: High Performance and Reaction Mechanism. *Energy Technology* **2019,** *7*, 1800777.

20. Ji, L.; Rao, M.; Zheng, H.; Zhang, L.; Li, Y.; Duan, W.; Guo, J.; Cairns, E. J.; Zhang, Y., Graphene Oxide as a Sulfur Immobilizer in High Performance Lithium/Sulfur Cells. *J. Am. Chem. Soc.* **2011,** *133*, 18522-18525.

21. Dugas, R.; Forero-Saboya, J. D.; Ponrouch, A., Methods and Protocols for Reliable Electrochemical Testing in Post-Li Batteries (Na, K, Mg, and Ca). *Chem. Mater.* **2019,** *31*, 8613-8628.

22. Choi, W.; Shin, H.-C.; Kim, J. M.; Choi, J.-Y.; Yoon, W.-S., Modeling and Applications of Electrochemical Impedance Spectroscopy (EIS) for Lithium-ion Batteries. *J. Electrochem. Sci. Technol* **2020,** *11*, 1-13.

23. Allen J. Bard and Larry R. Faulkner, Electrochemical Methods: Fundamentals and Applications, New York: Wiley, 2001, 2nd ed. *Russ. J. Electrochem.* **2002,** *38*, 1364-1365.

24. Lifshin, E.; Lifshin, E., *X-ray Characterization of Materials*. Wiley Online Library: 1999; Vol. 38.

25. Akhtar, K.; Khan, S. A.; Khan, S. B.; Asiri, A. M., Scanning Electron Microscopy: Principle and Applications in Nanomaterials Characterization. In *Handbook of Materials Characterization*, Sharma, S. K., Ed. Springer International Publishing: Cham, 2018; pp 113-145.

26. Jenkins, R., X-Ray Fluorescence Analysis. In *X-ray Characterization of Materials,* 1999; pp 171-209.

27. Moulder, J. F.; Stickle, W. F.; Sobol, P. E.; Bomben, K. D., *Handbook of X-ray photoelectron spectroscopy*. Perkin-Elmer Corporation: Eden Praire (MN), 1992; Vol. 40, p 261.

28. Larkin, P., Chapter 2 - Basic Principles. In *Infrared and Raman Spectroscopy*, Larkin, P., Ed. Elsevier: Oxford, 2011; pp 7-25.

Chapter 4

Preliminary Studies

This chapter begins by studying the performance of various magnesium salts ($Mg(ClO_4)_2$, $Mg(TFSI)_2$, $Mg(OTF)_2$, $Mg(HMDS)_2$) along with its combination with additives such as moisture scavenger $TBABH_4$ and $MgCl_2$. This investigation primarily investigates the reversibility of the magnesium plating and stripping process along with the morphology of the magnesium crystal from each magnesium salt. After establishing that $Mg(HMDS)_2$-based electrolyte is most appropriate to create a high Coulombic efficiency electrolyte, the chapter further establishes the importance of non-passivating magnesium salt. This is done by showing that even a slightly passivating $Mg(OTF)_2$-based electrolyte would require corrosive $MgCl_2$ and a high concentration of $TBABH_4$ additive. This requirement is shown to limit the anodic stability of high-functioning $Mg(OTF)_2$-based electrolytes. Thus, to create a high-functioning wide potential window electrolyte, $Mg(HMDS)_2$ salt has to be used.

4.1 Solubility of Various Magnesium Salt and Their Capability for Reversible Magnesium Deposition and Dissolution

To ascertain which salt is appropriate as the base material for the electrolyte, several salts were explored. These salts are magnesium trifluoromethanosulfonate [$Mg(OTF)_2$], magnesium bis(trifluorosulfonylimide) [$Mg(TFSI)_2$], magnesium bis(hexamethyldisilazide) [$Mg(HMDS)_2$], and magnesium perchlorate [$Mg(ClO_4)_2$]. Figure 4.1.1a shows the solubility of all these salts when they are dissolved in 1,2-dimethoxyethane (DME) with an intended concentration of 0.1 M. It is seen that 0.1 M $Mg(OTF)_2$ and 0.1 M $Mg(ClO_4)_2$ were not able to fully dissolve in the DME solvent. Besides these salts, $Mg(TFSI)_2$ and $Mg(HMDS)_2$ are well dissolved. However, phase separation occurs inside the $Mg(TFSI)_2$ in DME solution, as indicated by the less transparent bottom layer in the solution. Such observation is consistent with the previously reported phase separation phenomenon in $Mg(TFSI)_2$ in DME solution[1].

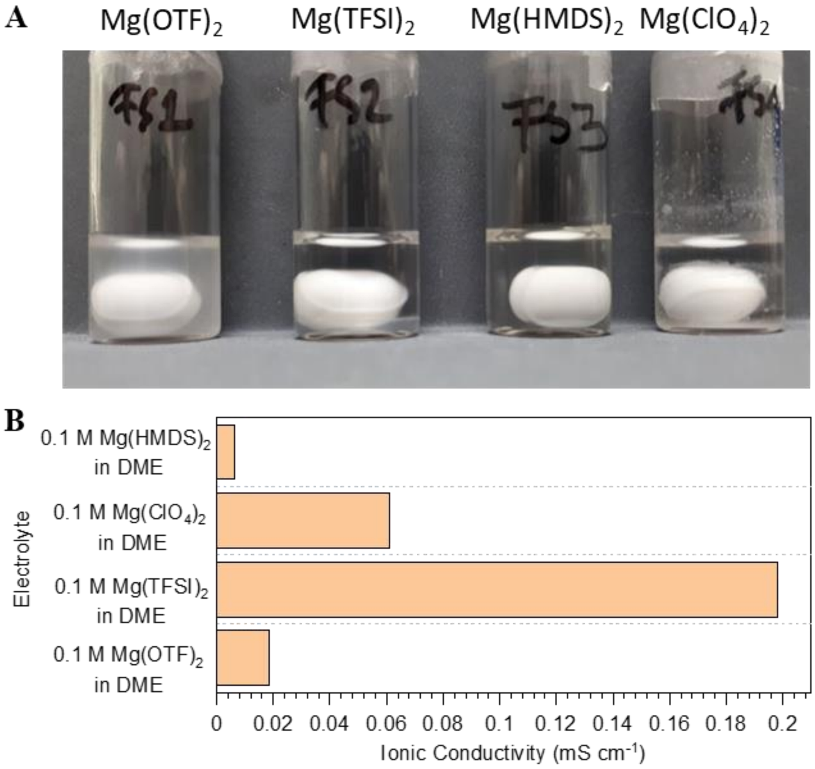

Figure 4.1.1: Visual Image of various magnesium electrolytes and ionic conductivities. (a) From left to right, images of 0.1 M $Mg(OTF)_2$, 0.1 M $Mg(TFSI)_2$, 0.1 M $Mg(HMDS)_2$ and 0.1 M $Mg(ClO_4)_2$. (b) Ionic conductivity of the electrolytes. All electrolytes were stirred at 40 °C for 2 days. The white oval substance in each vial is a stir bar.

The measured ionic conductivities of the salts are shown in figure 4.1.1b. The electrolyte with the highest ionic conductivity is 0.1 M $Mg(TFSI)_2$ with an ionic conductivity of 0.198 mS/cm. The other well solubilized electrolyte, 0.1 M $Mg(HMDS)_2$ in DME, has the lowest ionic conductivity of 6.28 μS/cm, indicating that the salt has an extremely low ionic dissociation in DME. The other salts with low solubility, $Mg(OTF)_2$ and $Mg(ClO_4)_2$, have ionic conductivities of 0.019 mS/cm and 0.061 mS/cm respectively.

To analyze the suitability of each electrolyte for a rechargeable magnesium battery, a magnesium plating and stripping experiment is conducted with each electrolyte. Figure 4.1.2 shows the galvanostatic cycling profile of these electrolytes at the controlled current density of 50 μA cm^{-2} and magnesium plating capacity of 50 μAh cm^{-2}. Figure 4.1.2 shows that the irreversible plating and stripping process occurs in $Mg(OTF)_2$ in DME, $Mg(TFSI)_2$ in DME, and $Mg(HMDS)_2$ in DME electrolytes in the first cycle of the plating and stripping process. Moreover, The cells containing the $Mg(HMDS)_2$ in DME electrolyte stopped operating during the plating process in the first cycle as the working electrode potential reached the cut-off potential during the plating process. Similarly, the cells that are cycled with $Mg(ClO_4)_2$ in DME electrolyte can be cycled for only 3 cycles as the working electrode potential during the plating process reached the cut-off potential in the 3rd cycle. Therefore, only $Mg(OTF)_2$ in DME and $Mg(TFSI)_2$ in DME can be cycled for a large number.

After the first plating and stripping cycle, the electrochemistry of the plating and stripping process in the $Mg(OTF)_2$ in DME electrolyte improves as indicated by the reduced working electrode overpotential and increased Coulombic efficiency as indicated in figure 4.1.2b. Similar observation can be seen in the $Mg(TFSI)_2$ electrolyte as seen in figure 4.1.2c. figure 4.12c plots the Coulombic efficiency of the $Mg(OTF)_2$ in DME and $Mg(TFSI)_2$ in DME electrolyte. From this figure, it can be seen that $Mg(OTF)_2$ in DME has the highest Coulombic efficiency. The Coulombic efficiency, nevertheless, is well below the appropriate limit for magnesium battery application. The overpotentials of the magnesium plating and stripping process in each electrolyte are also extremely high for magnesium battery application.

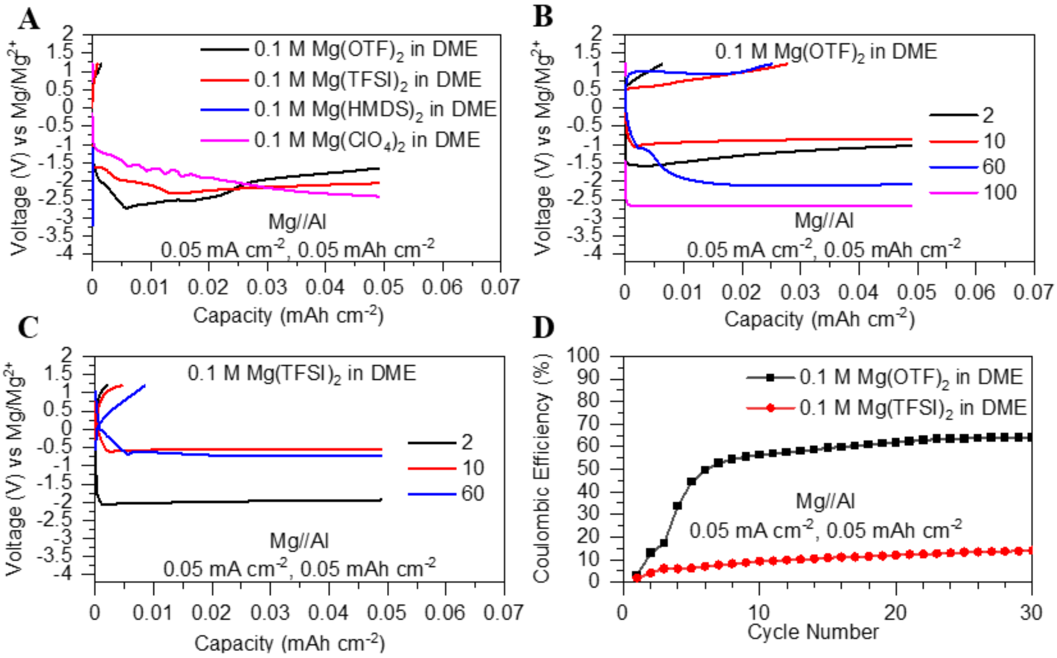

Figure 4.1.2: Galvanostatic magnesium plating and stripping process in various conventional magnesium electrolytes. (a) First plating and stripping cycle of each electrolyte. (b and c) magnesium plating and stripping process in $Mg(OTF)_2$- and $Mg(TFSI)_2$-based electrolytes across multiple cycles. (d) Coulombic efficiency of the magnesium plating and stripping process in $Mg(OTF)_2$- and $Mg(TFSI)_2$-based electrolytes.

4.2 Comparison of various magnesium salt electrolytes with borohydride and chloride-based additive

Given that the magnesium is easily passivated by the existence of a minuscule amount of moisture in the electrolyte, it is not surprising that the electrolytes shown in figure 4.2.1 show poor Coulombic efficiency and large overpotential. To reduce the passivation of the anode, tetrabutylammonium borohydride ($TBABH_4$) is added to each electrolyte. Images of the electrolyte are shown below. Visually, it is seen that both $Mg(OTF)_2$ and $Mg(ClO_4)_2$ have poor solubility. Moreover, the amount of solid precipitating in the 0.1 M $Mg(ClO_4)_2$ seems to increase upon the addition of $TBABH_4$, indicating the incompatibility between $Mg(ClO_4)_2$ and $TBABH_4$. More importantly, the 0.1 M $Mg(TFSI)_2$ solution does not separate into two liquid phases upon the addition of $TBABH_4$. Such observation is also seen in other $Mg(TFSI)_2$ solutions which were mixed with other additives such as TBAOTF or TBACl (figure A1). The origin of a two phases separation in $Mg(TFSI)_2$DME solution was previously investigated by Chen *et al.*[2] It was suggested in their study that the stability of the liquid phase in $Mg(TFSI)_2$

in DME solution is determined by the electrostatic interaction between Mg^{2+} ions in the solution. Thus, the addition of other salts might disrupt the stability of one of the phases in the solution.

The ionic conductivities of the electrolytes are shown in figure 4.2.1 b. Upon the addition of $TBABH_4$, a significant increase in the ionic conductivity of each electrolyte is observed. The increased ionic conductivity is likely due to the increase in ion concentration due to the contribution of $TBABH_4$ salt. The introduction of TBA^+ ions into the solution may also increase the dissociation of the magnesium salts in the electrolytes. Overall, the $Mg(TFSI)_2$-based electrolyte has the highest ionic conductivity 0.74 mS/cm, followed by $Mg(HMDS)_2$-based electrolyte with an ionic conductivity of 0.42 mS/cm, $Mg(OTF)_2$-based electrolyte with an ionic conductivity of 0.21 mS/cm and $Mg(ClO_4)_2$-based electrolyte with an ionic conductivity of 0.12 mS/cm. Surprisingly, the $Mg(HMDS)_2$-based electrolyte has a higher ionic conductivity than $Mg(OTF)_2$ and $Mg(ClO_4)_2$. Potentially, this observation indicates that $TBABH_4$ forms ion clusters when it is added to the $Mg(OTF)_2$ and $Mg(ClO_4)_2$. It is well known that BH_4^- strongly bonds with Mg^{2+}.[3, 4] The coordination between BH_4^- and Mg^{2+} in $Mg(OTF)_2$ and $Mg(ClO_4)_2$-based solution may cause the ion concentrations in $Mg(OTF)_2$ and $Mg(ClO_4)_2$ solutions to be lower than the ion concentrations in $Mg(HMDS)_2$-based electrolyte.

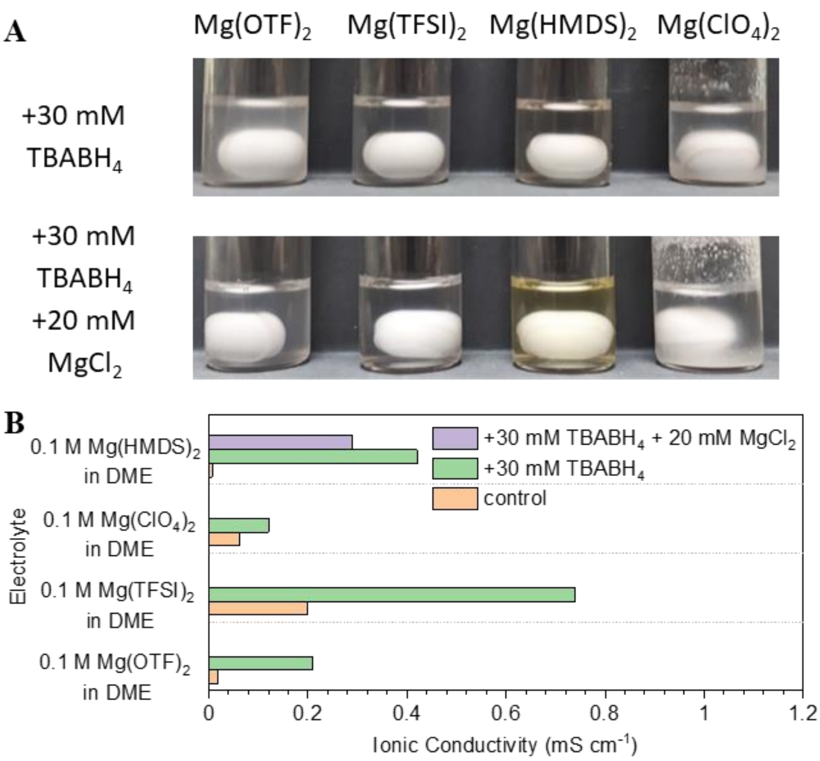

Figure 4.2.1: Visual images of various magnesium electrolytes with borohydride additives and their ionic conductivity. (a) From left to right, images of 0.1 M $Mg(OTF)_2$, 0.1 M $Mg(TFSI)_2$, 0.1 M $Mg(HMDS)_2$ and 0.1 M $Mg(ClO_4)_2$ in DME with the addition of 30 mM $TBABH_4$ in each electrolyte. (b) Ionic conductivities of 0.1 M $Mg(HMDS)_2$ in DME, 0.1 M $Mg(ClO_4)_2$ in DME 0.1 M $Mg(OTF)_2$ in DME, 0.1 M $Mg(TFSI)_2$ in DME and 0.1 M $Mg(OTF)_2$ in DME with 30 mM $TBABH_4$. All electrolytes were stirred at 40 °C for 2 days. The white oval substance in each vial is a stir bar.

Figure 4.2.2 a,b,c, and d show the galvanostatic profile of various magnesium salts in DME with the addition of 30 mM $TBABH_4$. Comparing the potential profile of the first cycle, it can be observed that except for 0.1 M $Mg(ClO_4)_2$, all the electrolytes allow for reversible magnesium deposition and dissolution. Moreover, even though the cells are cycled at an increased current density of 0.5 mA cm^{-2}, the Coulombic efficiencies of plating and stripping in most electrolytes improved. Furthermore, the overpotentials of the plating and stripping processes in each electrolyte were also reduced (as compared to the electrolyte in figure 4.1.1 a). This indicates that electrode passivation by electrolyte impurities is a major problem in the conventional electrolytes previously tested in §4.1. $TBABH_4$ salt is also shown to be an effective additive to circumvent the issue. It is worth noting that the $Mg(ClO_4)_2$-based electrolyte seems to passivate the magnesium anode despite the addition of $TBABH_4$ into the electrolyte, as seen from figure 4.2.2a.

In the first cycle of the magnesium plating and stripping process, $Mg(OTF)_2$-based electrolyte shows the highest plating and stripping Coulombic efficiency. This may indicate that other salts such as $Mg(TFSI)_2$ and $Mg(HMDS)_2$ have much more passivating impurities. Figures 4.2.2 b, c and d show the cycling profile of each electrolyte in subsequent cycles. As the half-cell cycling progresses, the Coulombic efficiency of the cells containing Mg $(HMDS)_2$-based electrolyte increases significantly reaching up to more than 99%. The average Coulombic efficiency of the $Mg(HMDS)_2$-based electrolyte is also the highest amongst other electrolytes (98.61%). Although the plating and stripping overpotential of $Mg(HMDS)_2$ based electrolytes is larger than other electrolytes (overpotential of 0.6 V), it reduces to 0.45 V in the subsequent cycle. This behavior contrasts with other electrolytes salts that also show reversible magnesium plating and stripping processes. The initial Coulombic efficiency of $Mg(OTF)_2$-based electrolyte is the highest within the cell lifetime (95.71%) and it subsequently reduces to lower than 90% within 4 cycles. The average Coulombic efficiency of the electrolyte is 88.6%, significantly lower than $Mg(HMDS)_2$-based electrolyte. Simultaneously, the plating and stripping overpotential of magnesium metal in the $Mg(OTF)_2$-based electrolytes also does not stabilize and increases with each cycle. Similar to $Mg(OTF)_2$-based electrolytes, the Coulombic efficiency of the $Mg(TFSI)_2$-based electrolytes reduces with each cycle and is subsequently shorted (average CE of 17.78%). The plating and stripping overpotential in the $Mg(TFSI)_2$-based electrolyte also grows with each cycle. Nevertheless, it is important to note that the overpotential growth and Coulombic efficiency degradation in $Mg(TFSI)_2$ are exacerbated as compared to $Mg(OTF)_2$-based electrolyte. To summarize the interpretation of figure 4.2.2, the magnesium salt stability against magnesium metal heavily influences the magnesium cell lifetime, plating and stripping overpotentials, and Coulombic efficiency. With a non-passivating salt such as $Mg(HMDS)_2$, high Coulombic efficiency, stable plating, and stripping overpotential, and long cell lifetime can be maintained. However, when a passivating salt is used, poor magnesium plating and stripping Coulombic efficiency, high overpotential, and short cell lifetime are to be expected.

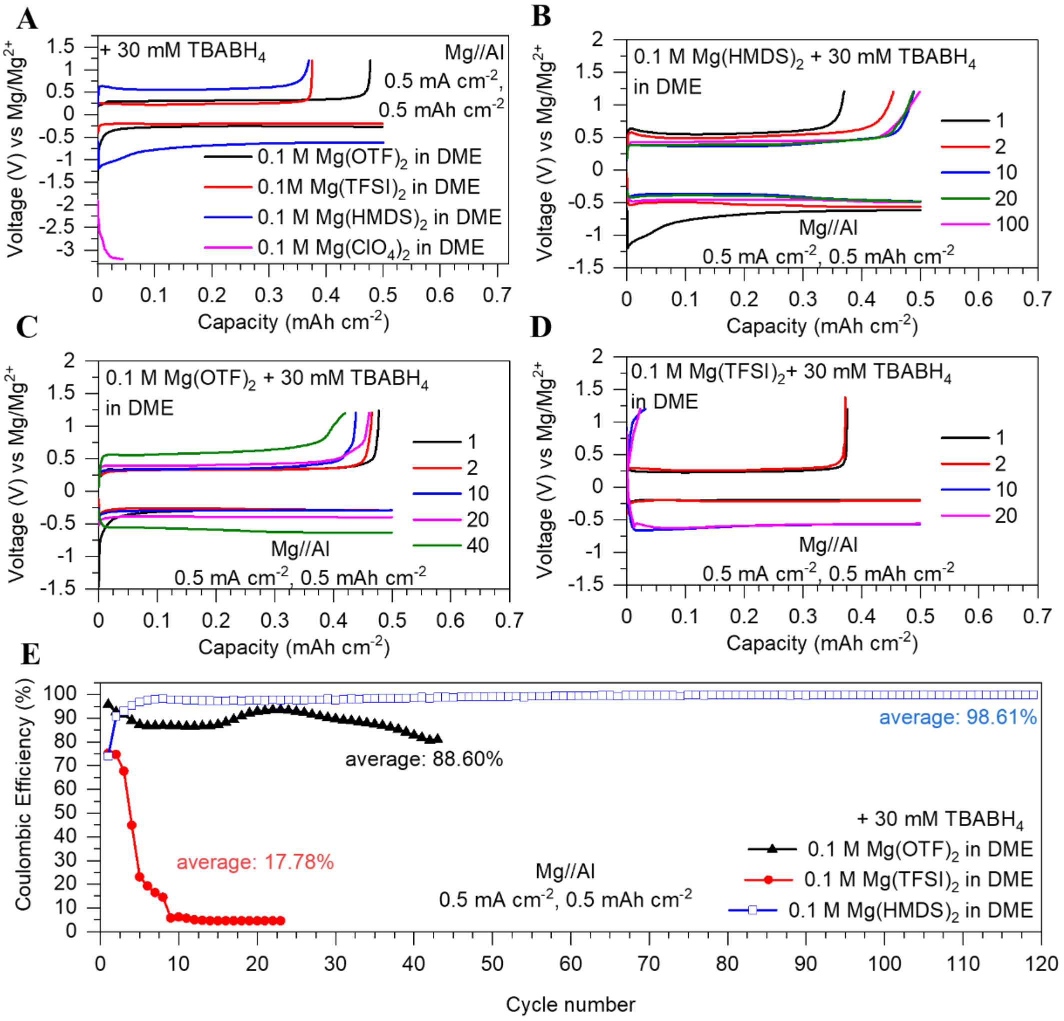

Figure 4.2.2: Galvanostatic magnesium plating and stripping using various conventional salts with $TBABH_4$ additive. (a) The first cycle of all electrolytes tested. (b, c, and d) Cycling profiles $Mg(HMDS)_2$-, $Mg(OTF)_2$-, and ($Mg(TFSI)_2$ based electrolytes respectively. (e) Coulombic efficiency of each electrolyte for magnesium plating and striping.

Another additive that was also explored is $MgCl_2$. Chloride-based additives are often used in conventional magnesium electrolytes to improve the magnesium plating and stripping overpotential (as discussed in chapter 2). However, as chloride is known to induce corrosion on the cathode current collector, the amount of chloride in the electrolytes was kept at a low concentration of 40 mM (20 mM $MgCl_2$). Although the chloride content in the electrolytes was low, it was found that the additive effectively improves the magnesium plating and stripping overpotentials in each electrolyte, except for $Mg(ClO_4)_2$-based electrolyte which is too passivating (figure 4.2.3a).

In the case of $Mg(HMDS)_2$-based electrolyte (figure 4.2.3 b), $MgCl_2$ significantly reduces the overpotential of the cell in the cell's early cycling progression. The first plating and stripping overpotential of the $Mg(HMDS)_2$-based electrolyte reduces significantly from 0.6 V to 0.35 V due to the addition of $MgCl_2$. As the cell-cycling progressed, the magnesium plating and stripping overpotential of the $Mg(HMDS)_2$-based electrolyte was further reduced to ~0.24 V. Due to the non-passivating nature of $Mg(HMDS)_2$, the $Mg(HMDS)_2$-based electrolyte has a Coulombic efficiency of which is close to 100%. Thus, $MgCl_2$ could not provide a large improvement to the plating and stripping overpotential for the electrolyte (from 98.61% to 98.91%). A general increase in the maximum cell-cycling number was also seen, indicating that $MgCl_2$ suppresses the formation of short-circuit connections. This means that $MgCl_2$ prevents dendrite from growing from the magnesium metal, or that it homogenizes the magnesium plating process on the anode.

Similar to what is observed in the $Mg(HMDS)_2$-based electrolyte, the addition of $MgCl_2$ into $Mg(OTF)_2$- and $Mg(TFSI)_2$- based electrolytes improved the Coulombic efficiency and reduces the overpotentials of the magnesium plating and stripping reaction. $MgCl_2$ provides a significant benefit for $Mg(OTF)_2$-based electrolytes, increasing the average Coulombic efficiency from 88.4% to 94.6%. On the other hand, the performance of $Mg(TFSI)_2$-based electrolyte was not significantly improved upon the addition of $MgCl_2$. In particular, $MgCl_2$ could not prevent the severe Coulombic efficiency degradation associated with $Mg(TFSI)_2$. It can be concluded, therefore, that the effectiveness of the $MgCl_2$ additive is dependent on the main magnesium salt utilized in the electrolyte. In particular, highly unstable salts such as $Mg(TFSI)_2$ and $Mg(ClO_4)_2$ are not compatible with the magnesium anode even if $MgCl_2$ is added to the electrolyte (higher $MgCl_2$ concentration may be needed to create a magnesium anode compatible electrolyte). Less passivating salts such as $Mg(OTF)_2$ showed a significant improvement upon a small addition of $MgCl_2$. However, the additive does not prevent passivation and cell failure from happening. Rather, it suppresses the negative effect of the passivating anion. Thus, it is seen in this study that the combination of $Mg(HMDS)_2$, $TBABH_4$, and $MgCl_2$ in the electrolyte allows for high Coulombic efficiency and low plating and stripping overpotential, making the electrolyte highly desirable in terms of its anode compatibility. The symmetric Mg||Mg cell test (Figure 4.2.3f) further confirms the benefit of $MgCl_2$ in reducing the cell overpotential. It is worth noting, however, that this effect is short-termed to several cycle numbers.

Evidence of the $MgCl_2$ effect on Mg/Mg^{2+} charge transfer resistance is also shown in the Nyquist plot of figure A2. The graph shows the effect of the conditioning process in $Mg(HMDS)_2$ + 30 mM $TBABH_4$ in DME electrolyte which reduces the charge transfer resistance of the magnesium electrode with each cycle. In contrast, the general trend of the Nyquist plots of $Mg(OTF)_2$ + 30 mM $TBABH_4$ in DME and $Mg(TFSI)_2$ + 30 mM $TBABH_4$ in DME does not show any conditioning process to be happening in the electrolytes. In general, the charge transfer resistance of $Mg(HMDS)_2$ + 30 mM $TBABH_4$ in DME is lower than of $Mg(OTF)_2$ + 30 mM $TBABH_4$ in DME, which in turn is also lower than $Mg(TFSI)_2$ + 30 mM $TBABH_4$ in DME. This trend is also consistent with the stability trend of the electrolytes' anion ($HMDS^-$>OTF^->$TFSI^-$). Crucially, the Nyquist plots also show that the $MgCl_2$ additive reduces the charge transfer resistance in $Mg(HMDS)_2$- and $Mg(OTF)_2$-based electrolytes. This effect, however, was not seen in the $Mg(TFSI)_2$-based electrolyte and may indicate reduced effectiveness of $MgCl_2$ additive in this electrolyte.

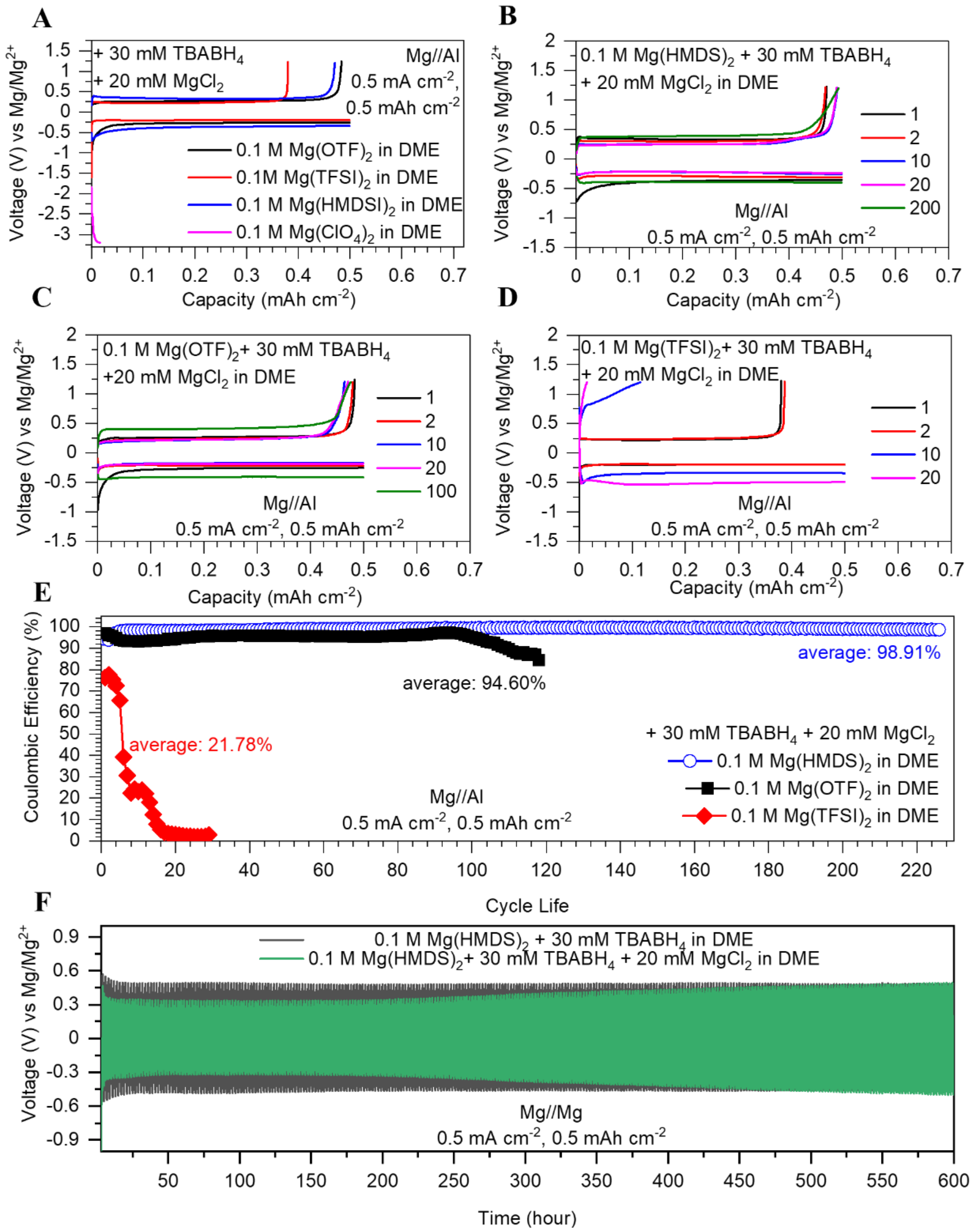

Figure 4.2.3: Galvanostatic magnesium plating and stripping using various conventional salts with $TBABH_4$ and $MgCl_2$ additives at 0.5 mA cm^{-2} and 0.5 mAh cm^{-2}. (a) The first cycle of all electrolytes tested. (b, c, and d) Magnesium plating and stripping cycle of $Mg(HMDS)_2$-based, $Mg(OTF)_2$-based and $Mg(TFSI)_2$-based electrolytes respectively. (e) Coulombic efficiency of the electrolytes. (f) Mg//Mg Symmetric cell potential profile of $Mg(HMDS)_2$-based electrolytes with and without 20 mM $MgCl_2$ in the electrolyte.

4.3 Magnesium deposit elemental analysis and interphase study

To study how each magnesium salt affects the electrochemically deposited magnesium morphology and its chemical composition. Electron microscopy and EDS elemental analysis of each magnesium deposit from the electrolytes were conducted. The electrochemical deposition was conducted using asymmetric Mg//Al-C half-cell. Figure 4.3.1 shows the lateral and cross-section image of the magnesium deposits on carbon-coated aluminum electrodes.

The figures show that the magnesium salt used in each electrolyte affects the magnesium deposit size, porosity, growth type, and distribution on the aluminium electrode. In the $Mg(TFSI)_2$ + 30 mM $TBABH_4$ in DME electrolyte, magnesium was observed to grow into hemispherical deposits at the applied current density of 0.5 mA cm^{-2} (figures 4.3.1 a and d). This is consistent with publications under similar plating condition.[5, 6] $MgCl_2$ does not seem to change the morphology of the magnesium deposits in the $Mg(TFSI)_2$- based electrolyte (figures 4.3.1 g and j), but it seems to affect how the distribution of the magnesium deposit on the electrode. Generally, it is seen that the magnesium globules are distributed more closely toward each other when $MgCl_2$ was added to the electrolyte.

On the other hand, the magnesium deposition morphology from the $Mg(OTF)_2$ + 30 mM $TBABH_4$ in DME electrolyte is unsuitable for magnesium battery application (figures 4.3.1 b and e). The magnesium deposits from the electrolyte are shown to be made of interconnected magnesium granules forming a thick and porous deposit on the aluminium electrode. The bulk magnesium mass in this deposit, therefore, has poor electrical contact with the current collector. This may partly explain the low Coulombic efficiency of the electrolyte. Moreover, dendrites (shown in figure A3) are also shown to grow in certain parts of the electrode. However, $MgCl_2$ additives reduce the thickness and porosity of the anode (figures 4.3.1 h and k).

Amongst the electrolytes discussed, the $Mg(TFSI)_2$ + 30 mM $TBABH_4$ in DME electrolyte produces the best magnesium morphology suitable for battery application (figures 4.3.1 c and f). As seen in the images, the magnesium film is thin, densely packed, and is evenly distributed on the aluminium substrate. The deposit, therefore, has good electrical contact with its substrate and is unlikely to cause a short circuit during battery cycling. The addition of $MgCl_2$ into the electrolyte does not seem to change the deposition morphology of the $Mg(HMDS)_2$-based electrolyte (figures 4.3.1 i and l).

Figure 4.3.2 shows the EDS elemental analysis of each sample (point analysis is used to quantify the magnesium percentage of the deposit more accurately). The elemental analysis of each point shows magnesium as the primary component of every sample analyzed. This confirms that magnesium electrochemical deposition was successfully conducted in the $Mg(TFSI)_2$, $Mg(OTF)_2$, and $Mg(HMDS)_2$-based electrolytes. In the case of $Mg(OTF)_2$ and $Mg(TFSI)_2$ derived samples, fluorine and sulfur impurities are observed on the samples (figures 4.3.2 a and b). This observation shows that $TFSI^-$ and OTF^- are reduced when they are in contact with the magnesium metal. Generally, higher concentrations of fluorine and sulfur were detected on the $Mg(TFSI)_2$-derived samples than on the $Mg(OTF)_2$ derived samples. This confirms that OTF^- is more stable than the $TFSI^-$ ion. Additional EDX analysis of the sample in figure 4.3.2 A (figure A4) further indicates that the magnesium to impurity ratio in some samples is relatively high, indicating that the decomposition rate of $TFSI^-$ is higher on certain magnesium deposits.

The addition of $MgCl_2$ into the electrolyte reduces the concentration of both F and S in the spectrum of each sample (figures 4.3.2 d and e). Thus, it is shown that $MgCl_2$ prevents the decomposition of $TFSI^-$ and OTF^- ions. On the other hand, $Mg(HMDS)_2$-derived sample does not show any sign of $Mg(HMDS)_2$ salt decomposition in its spectrum (figures 4.3.2 c and f). These observations confirm that $Mg(HMDS)_2$-based electrolyte is more stable as compared to $Mg(TFSI)_2$-based and $Mg(OTF)_2$-based electrolyte. Hence, the morphological study and elemental analysis of the magnesium samples affirms that $Mg(HMDS)_2$ is most suitable for rechargeable battery electrolytes. Specifically, the electrolyte creates a homogenous and non-passivated magnesium film during the plating process. This allows for a highly reversible magnesium anode plating and stripping process in the electrolyte.

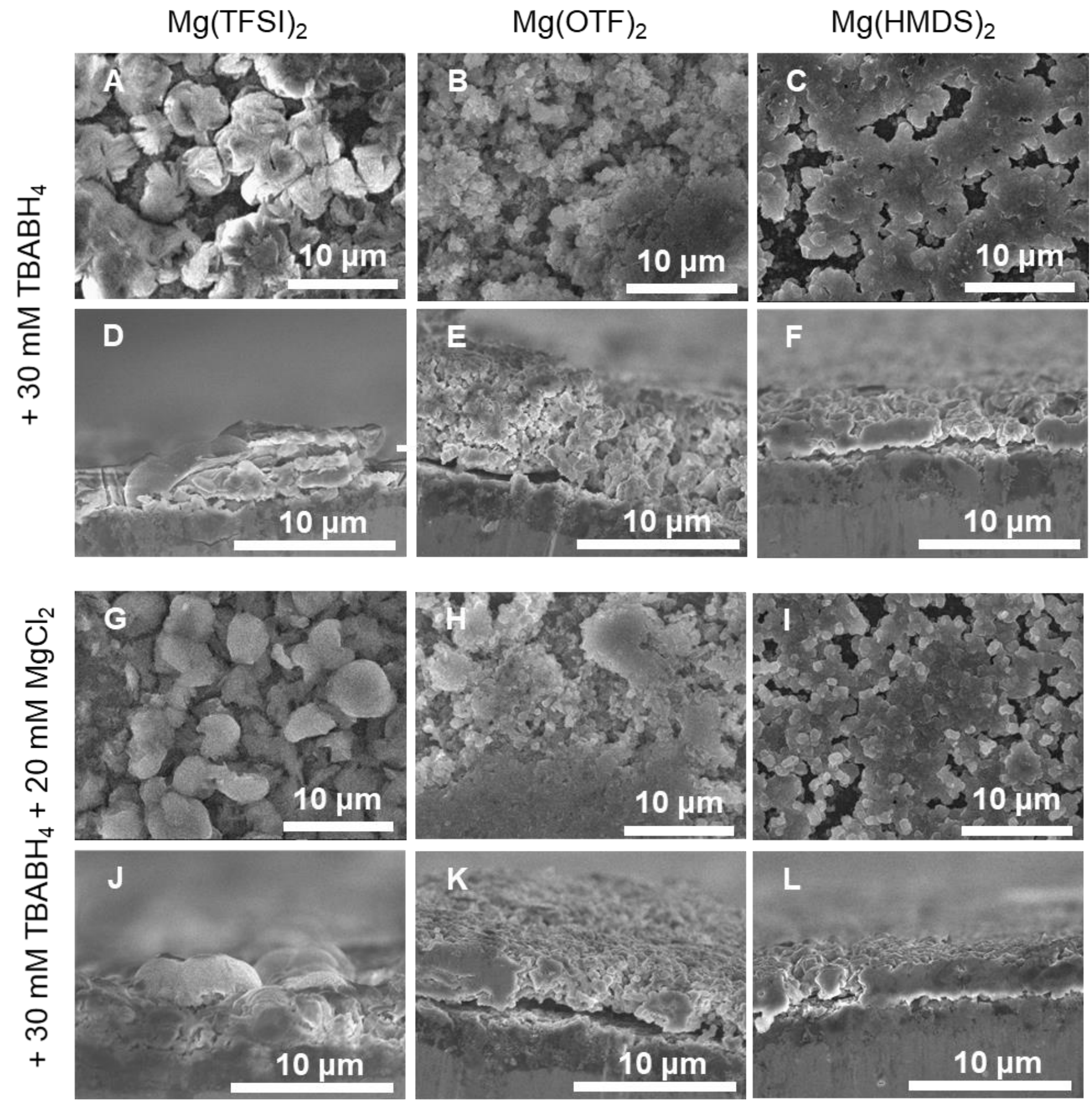

Figure 4.3.1: Electron microscopy image of various magnesium deposits (plating current density of 0.5 mA cm^{-2} and areal capacity of 0.5 mAh cm^{-2}). Electrolyte sources: (a and d) 0.1 M $Mg(TFSI)_2$ + 30 mM $TBABH_4$ in DME, (b and e) 0.1 M $Mg(OTF)_2$ + 30 mM $TBABH_4$ in DME, (c and f) 0.1 M $Mg(HMDS)_2$ + 30 mM $TBABH_4$ in DME, (g and j) 0.1 M $Mg(TFSI)_2$ + 30 mM $TBABH_4$ + 20 mM $MgCl_2$ in DME, (h and k) 0.1 M $Mg(OTF)_2$ + 30 mM $TBABH_4$ + 20 mM $MgCl_2$ in DME, (i and l) 0.1 M $Mg(HMDS)_2$ + 30 mM $TBABH_4$ + 20 mM $MgCl_2$ in DME.

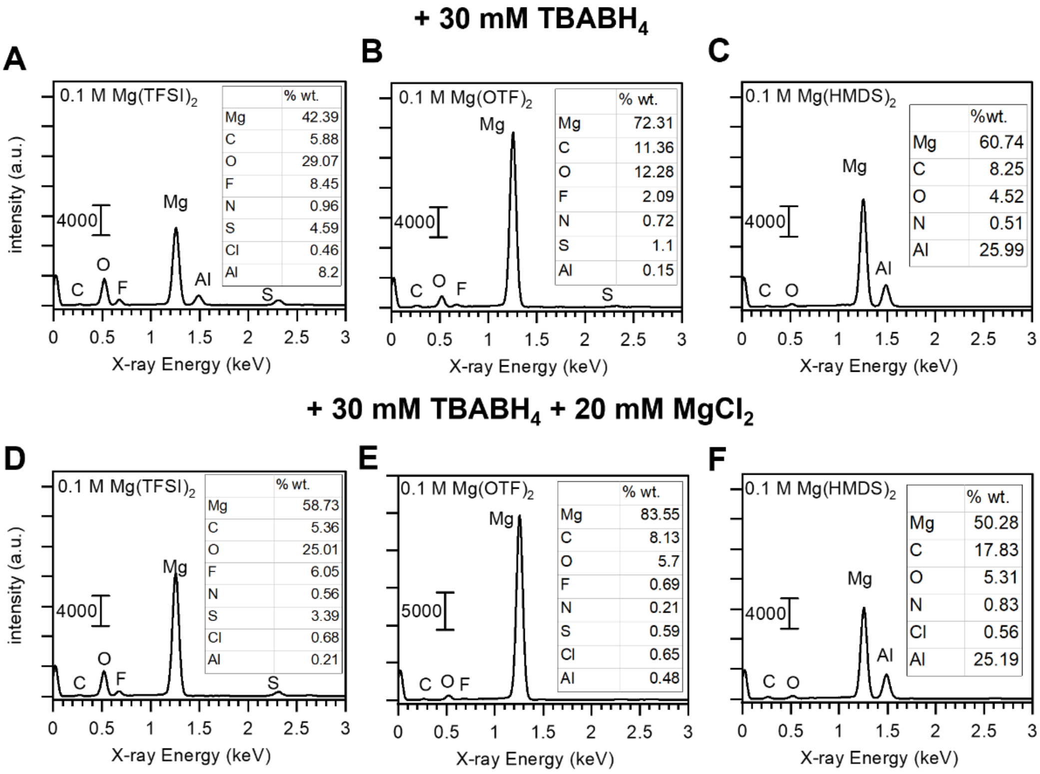

A

	% wt.
Mg	42.39
C	5.88
O	29.07
F	8.45
N	0.96
S	4.59
Cl	0.46
Al	8.2

B

	% wt.
Mg	72.31
C	11.36
O	12.28
F	2.09
N	0.72
S	1.1
Al	0.15

C

	%wt.
Mg	60.74
C	8.25
O	4.52
N	0.51
Al	25.99

D

	% wt.
Mg	58.73
C	5.36
O	25.01
F	6.05
N	0.56
S	3.39
Cl	0.68
Al	0.21

E

	% wt.
Mg	83.55
C	8.13
O	5.7
F	0.69
N	0.21
S	0.59
Cl	0.65
Al	0.48

F

	% wt.
Mg	50.28
C	17.83
O	5.31
N	0.83
Cl	0.56
Al	25.19

Figure 4.3.2: EDX elemental analysis of the electrochemically deposited magnesium from each sample in figure 4.3.1. (Aluminium peak originated from the aluminium substrate)

4.4 Performance study of $Mg(OTF)_2$-based electrolyte with increased borohydride and chloride additives

The previous section shows that $Mg(HMDS)_2$-based electrolytes exhibited the best compatibility with the magnesium anode. Nevertheless, $Mg(OTF)_2$-based electrolyte could also achieve a Coulombic efficiency above that of 90% (with the addition of $MgCl_2$). Since $Mg(OTF)_2$ salt is relatively cheaper than $Mg(HMDS)_2$, optimizing the magnesium salt compatibility with the magnesium metal could reduce the rechargeable battery manufacturing cost. Hence additional experimentation is conducted to find the appropriate magnesium salt and additive concentration to achieve plating and stripping efficiency that is competitive against $Mg(HMDS)_2$.

To further increase the capability of $Mg(OTF)_2$-based electrolytes, a higher amount of additives has to be added. Figure 4.4.1 shows the performance of $Mg(OTF)_2$-based electrolytes (0.125 to 0.25 M $Mg(OTF)_2$) with the addition of $TBABH_4$ (10 to 128 mM) and $MgCl_2$ (0 to 31 mM) additives. The solutions are not fully dissolved and excess undissolved $Mg(OTF)_2$ is let to settle before the solution is used for cell cycling. It is interesting to note that the solubility of $Mg(OTF)_2$ salt improves significantly with the addition of a high amount of $TBABH_4$ (figure A5).

Figures 4.4.1 a, b, and c indicate, firstly, that without $MgCl_2$ additive, the $TBABH_4$ concentration has to be as high as 128 mM to create a long life-cycle cell. Several problems occur when the $TBABH_4$ concentration is low. First, the anode passivation process by OTF^- anion occurs at a higher rate. As seen in Figures 4.4.1 a, b, and c, the overpotential of the magnesium plating and stripping process grows with each cycle. $TBABH_4$ seems to suppress the passivation growth in the electrolyte. As $TBABH_4$ suppresses the passivation of the anode, the average Coulombic efficiency of the magnesium plating and stripping process also increases when more $TBABH_4$ is added to the electrolyte (figure 4.4.1 g). Moreover, the maximum cycle number of each cell seems to correlate negatively with the passivation rate of its anode. This likely indicates that another side effect of the anode passivation is that the magnesium deposition process becomes less homogenous[6, 7] and eventually results in the build-up of short-circuit connection between the electrodes. A potential explanation for the passivation suppressing effect of BH_4^- is that it replaces OTF^- from the solvation shell of Mg^{2+}, thereby preventing OTF^- from decomposing upon contact with the magnesium anode. This was suggested in a previous study of the $Mg(TFSI)_2$-$Mg(BH_4)_2$ system by Wang *et al.*[8] They proposed that the $Mg\text{-}BH_4^+$ ion clusters preferentially adsorb on the magnesium anode during the deposition process. This phenomenon prevents side reactions between the passivating $TFSI^-$ anion and the magnesium metal. A similar mechanism may have also occurred in the $Mg(OTF)_2$-based electrolyte reported in this thesis. Supporting this hypothesis is the fact that the ratio of OTF^- and BH_4^- seems to be crucial even at high $TBABH_4$ of 128 mM. This can be seen by comparing the behavior of cells containing 0.125 M $Mg(OTF)_2$ versus those which contain 0.25 M of $Mg(OTF)_2$. When the $Mg(OTF)_2$ concentration in the electrolyte is doubled, passivation of the anode seems to increase as indicated by the reduced Coulombic efficiency (93.39 to 91.17%, figure 4.4.1 g), shorter cell lifetime, and faster overpotential growth rate (figure 4.4.1 c and e). Since a high amount of $TBABH_4$ was added to the electrolyte (128 mM), the moisture concentration in the electrolytes was likely to be minuscule. Hence, the increased passivation in the electrolyte is likely to be due to an increased OTF^- concentration.

As mentioned in §4.2, $MgCl_2$ seems to be a crucial additive. Just by adding a minuscule amount of 31 mM $MgCl_2$, the cell lifetime and Coulombic efficiency of the electrolyte improve drastically. By controlling the concentration of $Mg(OTF)_2$, $TBABH_4$, and $MgCl_2$, a highly magnesium-compatible electrolyte can be created. Particularly, 0.125 M $Mg(OTF)_2$ with the addition of 128 mM of $TBABH_4$ and 31 mM of $MgCl_2$ shows a stable and small magnesium plating and stripping overpotentials of 0.17 V for at least 250 cycles (figure 4.4.1 d). Furthermore, the electrolyte exhibits an average Coulombic efficiency of 96.87% (figure 4.4.1 g). This means that $Mg(OTF)_2$ based electrolyte can be quite compatible with the magnesium anode if a high concentration of $TBABH_4$ and $MgCl_2$ are mixed into the electrolyte.

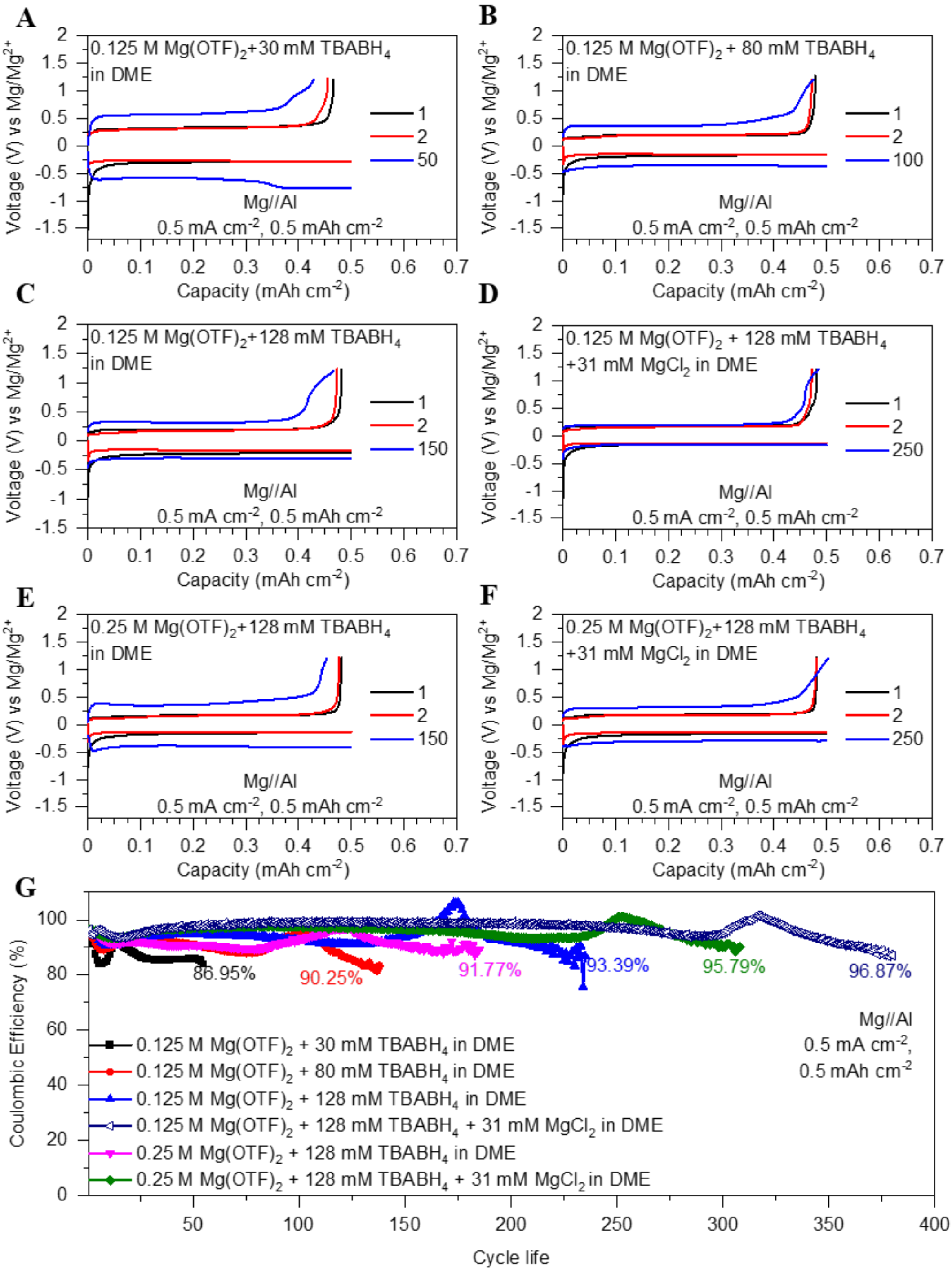

Figure 4.4.1: Performance of $Mg(OTF)_2$-based electrolytes.(a, b, c) Capacity-potential profile of 0.125 M $Mg(OTF)_2$ with various $TBABH_4$ concentration of 30 to 128 mM $TBABH_4$. (d) Capacity-potential profile of 0.125 M $Mg(OTF)_2$-based electrolyte with 128 mM $TBABH_4$ and 31 mM $MgCl_2$. (e) Capacity-potential profile of 0.25 M $Mg(OTF)_2$-based electrolyte with 128 mM $TBABH_4$. (f) Capacity-potential of 0.25 M $Mg(OTF)_2$-based electrolyte with 128 mM $TBABH_4$ and 31 mM $MgCl_2$. (g) Coulombic efficiency of $Mg(OTF)_2$-based electrolyte.

However, the addition of these additives severely reduces the anodic decomposition onset potential of the electrolyte. Figure 4.4.2 a shows, for example, that the anodic decomposition onset potential of the electrolyte reduces with increasing $TBABH_4$ concentration. With the addition of 128 mM $TBABH_4$ (the amount used to optimize the $Mg(OTF)_2$-based electrolyte performance), the onset of anodic decomposition of the electrolyte is at 2.25 V vs Mg/Mg^{2+} on stainless-steel electrode, and lower when tested against aluminium electrode. (figure 4.4.2 b)

Although the LSV data does not show any obvious change in the electrolyte oxidation potential upon the addition of $MgCl_2$ to the electrolyte (figure 4.4.2 b), the chronoamperometry measurements of both electrolytes show otherwise (figure 4.4.2 c and d). When the stainless-steel electrode potential is at 2.25 V vs Mg/Mg^{2+} or lower, the anodic current stays relatively low and stable for both electrolytes. However, at an increased potential of 2.375 V vs Mg, a clear difference in the decomposition current is observed. In particular, the anodic current shows an increasing trend when $MgCl_2$ is added to the electrolyte. Starting from ~3 μA cm^{-2}, the current density during the measurement increases up to 17.2 μA cm^{-2} after measurement. In contrast, when the electrolyte does not contain chloride, the anodic current at 2.375 V which flows through the electrolyte stays stable for 20 minutes. The increasing trend of the anodic current at 2.375 V in the chloride-containing electrolyte likely indicates that the corrosion process is happening on the Stainless-steel electrode.

To summarize this subsection, several limitations of using $Mg(OTF)_2$-based electrolytes have been established. Primarily, the performance of $Mg(OTF)_2$-based electrolyte heavily depends on the concentration of the additive in the electrolyte. To achieve a long cell lifetime and to suppress the passivating effect of $Mg(OTF)_2$, a high concentration of $TBABH_4$ (up to 128 mM) has to be added to the electrolyte. Moreover, a chloride-based additive is also necessary to improve the Coulombic efficiency of the electrolyte. Problematically, both $TBABH_4$ and $MgCl_2$ reduce the potential window of the electrolyte. Particularly, the high content of $TBABH_4$ causes the potential window of the electrolyte to be limited to about 2.375 V vs Mg (against stainless-steel electrode). The inclusion of even a minuscule amount of $MgCl_2$ further causes corrosion on the non-noble current collector. Creating a wide-potential window electrolyte with the $Mg(OTF)_2$ salt, therefore, is challenging, and thus, more focus is put on exploring

$Mg(HMDS)_2$ based electrolyte. Similar to what is observed in the $Mg(OTF)_2$-based electrolyte. The addition of $MgCl_2$ into the $Mg(HMDS)_2$ + 30 mM $TBABH_4$ in DME electrolyte seems to induce corrosion as shown by the LSV curve in figure 4.4.3. In particular, the anodic limit of the electrolyte reduces from ~2.75 V and ~2.6 V on stainless-steel and aluminium electrodes to ~2.3 V and ~1.5 V on stainless-steel and aluminium electrodes respectively after the addition of $MgCl_2$ to the electrolyte.

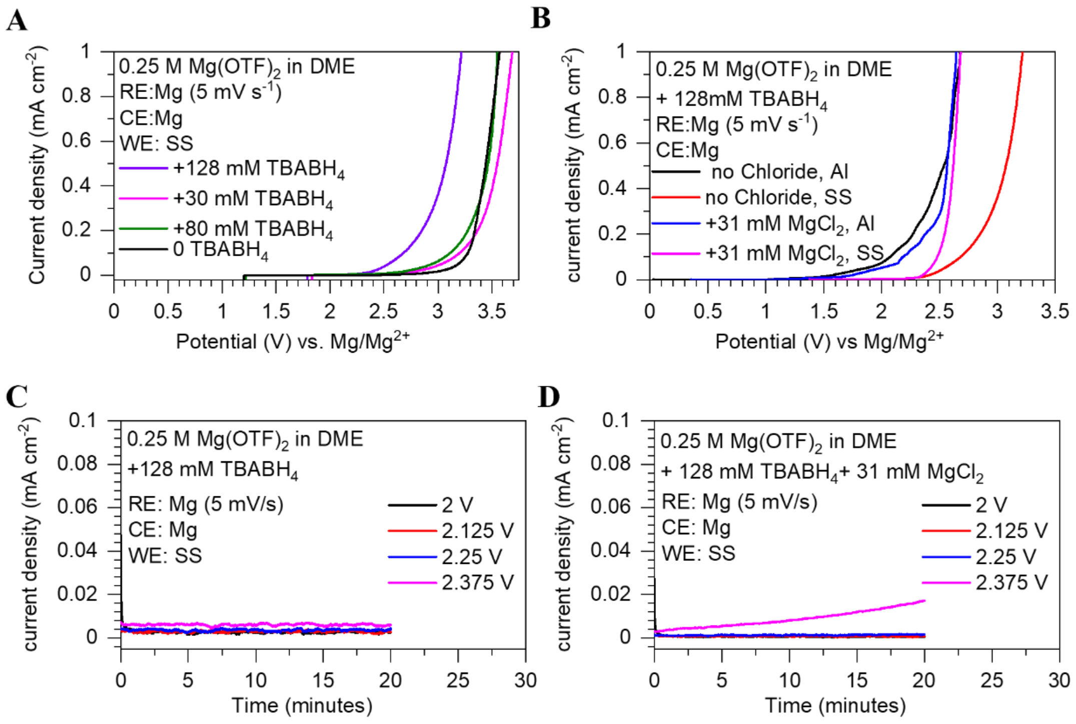

Figure 4.4.2: Anodic stability of $Mg(OTF)_2$-based electrolyte. (a) LSV measurement of stainless-steel electrode in 0.25 M Mg(OTF) in DME with various $TBABH_4$ concentration. (b) LSV measurement of stainless-steel and aluminium electrodes in 0.25 M $Mg(OTF)_2$ in DME with 128 mM $TBABH_4$. (c) Chronoamperometry measurement of a stainless-steel electrode in 0.25 M $Mg(OTF)_2$ in DME with 128 mM $TBABH_4$. (d) Chronoamperometry measurement of a stainless-steel electrode in 0.25 M $Mg(OTF)_2$ in DME with 128 mM $TBABH_4$ and 31 mM $MgCl_2$.

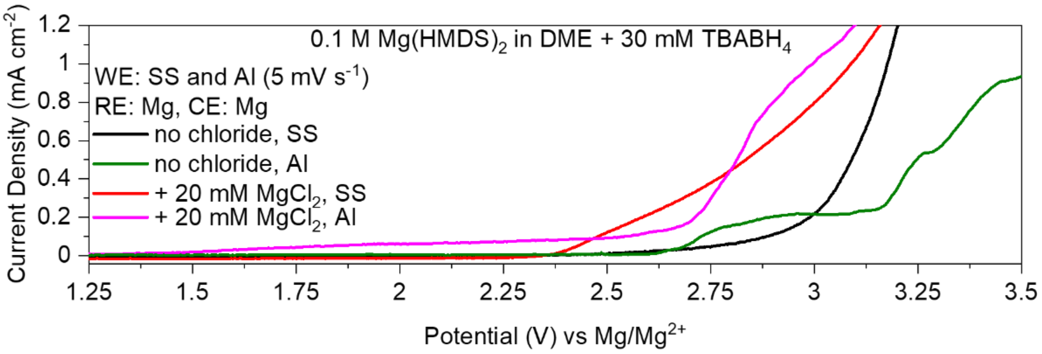

Figure 4.4.3: LSV measurement of stainless-steel electrodes in Mg(HMDS)$_2$-based electrolytes (with and without MgCl$_2$).

4.5 Conclusion

Based on the comparative study of various salts, it is seen that each commercial magnesium salt has a differing degree of compatibility with the magnesium anode. This resulted in varying degrees of magnesium plating and stripping reversibility depending on the magnesium salt used in the electrolyte. Moreover, it is found that Mg(HMDS)$_2$-based electrolyte provides the highest magnesium plating and stripping Coulombic efficiency (~99%). The major drawback of the electrolyte, however, is its high magnesium plating and stripping overpotential. As shown in the latter part of this chapter, the passivation effect of the magnesium salt anion is crucial. In particular, high concentrations of TBABH$_4$ and MgCl$_2$ must be added to the electrolyte to alleviate the passivation effect. These additives, however, reduce the potential window of the electrolyte severely. Hence, to create a wide potential window electrolyte, Mg(HMDS)$_2$ salt, which is the most stable salt studied, will be most suitable.

References

1. Salama, M.; Shterenberg, I.; Gizbar, H.; Eliaz, N. N.; Kosa, M.; Keinan-Adamsky, K.; Afri, M.; Shimon, L. J. W.; Gottlieb, H. E.; Major, D. T.; Gofer, Y.; Aurbach, D., Unique Behavior of Dimethoxyethane (DME)/Mg(N(SO$_2$CF$_3$)$_2$)$_2$ Solutions. *J. Phys. Chem. C* **2016,** *120*, 19586-19594.

2. Chen, Y.; Jaegers, N. R.; Wang, H.; Han, K. S.; Hu, J. Z.; Mueller, K. T.; Murugesan, V., Role of Solvent Rearrangement on Mg2+ Solvation Structures in Dimethoxyethane Solutions using Multimodal NMR Analysis. *J. Phys. Chem. Lett.* **2020,** *11*, 6443-6449.

3. Mohtadi, R.; Tutusaus, O.; Arthur, T. S.; Zhao-Karger, Z.; Fichtner, M., The metamorphosis of rechargeable magnesium batteries. *Joule* **2021,** *5*, 581-617.

4. Xu, H.; Zhang, Z.; Li, J.; Qiao, L.; Lu, C.; Tang, K.; Dong, S.; Ma, J.; Liu, Y.; Zhou, X.; Cui, G., Multifunctional Additives Improve the Electrolyte Properties of Magnesium Borohydride Toward Magnesium–Sulfur Batteries. *ACS Appl. Mater. Interfaces* **2018,** *10*, 23757-23765.

5. Eaves-Rathert, J.; Moyer, K.; Zohair, M.; Pint, C. L., Kinetic- versus Diffusion-Driven Three-Dimensional Growth in Magnesium Metal Battery Anodes. *Joule* **2020,** *4*, 1324-1336.

6. Ding, M. S.; Diemant, T.; Behm, R. J.; Passerini, S.; Giffin, G. A., Dendrite Growth in Mg Metal Cells Containing Mg(TFSI)2/Glyme Electrolytes. *J. Electrochem. Soc.* **2018,** *165*, A1983-A1990.

7. Yoo, H. D.; Han, S.-D.; Bolotin, I. L.; Nolis, G. M.; Bayliss, R. D.; Burrell, A. K.; Vaughey, J. T.; Cabana, J., Degradation Mechanisms of Magnesium Metal Anodes in Electrolytes Based on $(CF_3SO_1)_2N^-$ at High Current Densities. *Langmuir* **2017,** *33*, 9398-9406.

8. Wang, H.; Feng, X.; Chen, Y.; Liu, Y.-S.; Han, K. S.; Zhou, M.; Engelhard, M. H.; Murugesan, V.; Assary, R. S.; Liu, T. L.; Henderson, W.; Nie, Z.; Gu, M.; Xiao, J.; Wang, C.; Persson, K.; Mei, D.; Zhang, J.-G.; Mueller, K. T.; Guo, J.; Zavadil, K.; Shao, Y.; Liu, J., Reversible Electrochemical Interface of Mg Metal and Conventional Electrolyte Enabled by Intermediate Adsorption. *ACS Energy Lett.* **2020,** *5*, 200-206.

Chapter 5

Optimization Study on $Mg(HMDS)_2$-Based Electrolyte

After validating the $Mg(HMDS)_2$ as an appropriate magnesium source for the rechargeable battery electrolyte, this chapter focused on the optimization of the electrolyte composition. The chapter begins by evaluating the effect of $TBABH_4$ and $MgCl_2$ on various aspects of the electrolyte. Mainly, it is argued that chloride-based additive must be removed from the electrolyte to avoid current collector corrosion and that a moderate amount $TBABH_4$ (20 mM) is most appropriate. Further, DME is re-validated as the most appropriate solvent for the electrolyte and data will be shown to argue that the optimum concentration of $Mg(HMDS)_2$ in the electrolyte is 0.2 M. Additional galvanostatic cycling measurements are also provided to show that the Coulombic efficiency of the electrolyte is high across various applied current density (0.1-1.5 mAh cm^{-2}) and various areal capacity (0.5-1.5 mAh cm^{-2}). The capability of the electrolyte to accommodate the plating and stripping process at high current density or high areal plating capacity is also provided. Then, characterization of the magnesium complex in the electrolyte, the chemical composition of the magnesium crystal deposited from the electrolyte, and the chemical composition of the anode-electrolyte interphase are then provided. Lastly, the electrolyte is tested against Sulfur-based and CuS cathodes. In particular, the $Mg(HMDS)_2$-based electrolytes are shown to be highly compatible with the CuS cathode at 60 °C.

*This section is published substantially as “Using a Chloride-Free Magnesium Battery Electrolyte to Form a Robust Anode-Electrolyte Nanointerface” in Nano Letters (DOI:10.1021/acs.nanolett.1c02655). Reprinted with permission. Copyright 2021 American Chemical Society.

5.1 Establishing the amount of electrolytes additive suitable for the Mg(HMDS)$_2$-based electrolyte

As previously discussed in chapter 4, Mg(HMDS)$_2$ combination with TBABH$_4$ is most suited for rechargeable magnesium battery application. Although MgCl$_2$ helps in reducing the magnesium plating and stripping overpotential in the Mg(HMDS)$_2$-based electrolyte, even a minuscule concentration of chloride reduces the electrolyte potential window. Similarly, the amount of TBABH$_4$ also affects the potential window of the Mg(HMDS)$_2$-based electrolyte. To maximize the potential window of the electrolyte, this subsection explores the effect of TBABH$_4$ and MgCl$_2$ on the potential window of the electrolyte.

Firstly, the optimum amount of TBABH$_4$ concentration is established by analyzing the magnesium plating and stripping process at various TBABH$_4$ concentrations along with the anodic decomposition potential of each electrolyte. Figures 5.1.1 a, b, and c plot the potential capacity profile of the magnesium plating and stripping process with various TBABH$_4$ concentrations from 10 mM to 30 mM. Based on the data, it is seen that with an increased amount of TBABH$_4$, the overpotential of the plating and stripping process reduces. In particular, a TBABH$_4$ content of 20 mM or higher is needed to achieve a plating and stripping process of less than 0.5 V vs Mg. The Coulombic efficiency and the lifetime of the asymmetric cell increase with more TBABH$_4$. Moreover, during the symmetric cell cycling process of 0.1 M Mg(HMDS)$_2$ + 10 mM TBABH$_4$ in DME, it is also found that short-circuit would be developed during the first magnesium plating process in the cell (figure A6). Hence, the TBABH$_4$ concentration inside the cell must be maintained at a level above 10 mM.

Turning to the optimization of the electrolyte anodic stability, LSV analysis is conducted to determine the onset of electrolyte oxidation of 0.1 M Mg(HMDS)$_2$ containing 20 mM and 30 mM of TBABH$_4$ (figure 5.1.1 e). As indicated, the potential window of the electrolytes slightly increases when the amount of TBABH$_4$ is reduced. Since 20 mM of TBABH$_4$ is sufficient to enable the plating and stripping process without causing short-circuit, 20 mM is chosen as the base amount of TBABH$_4$ needed in the formulation.

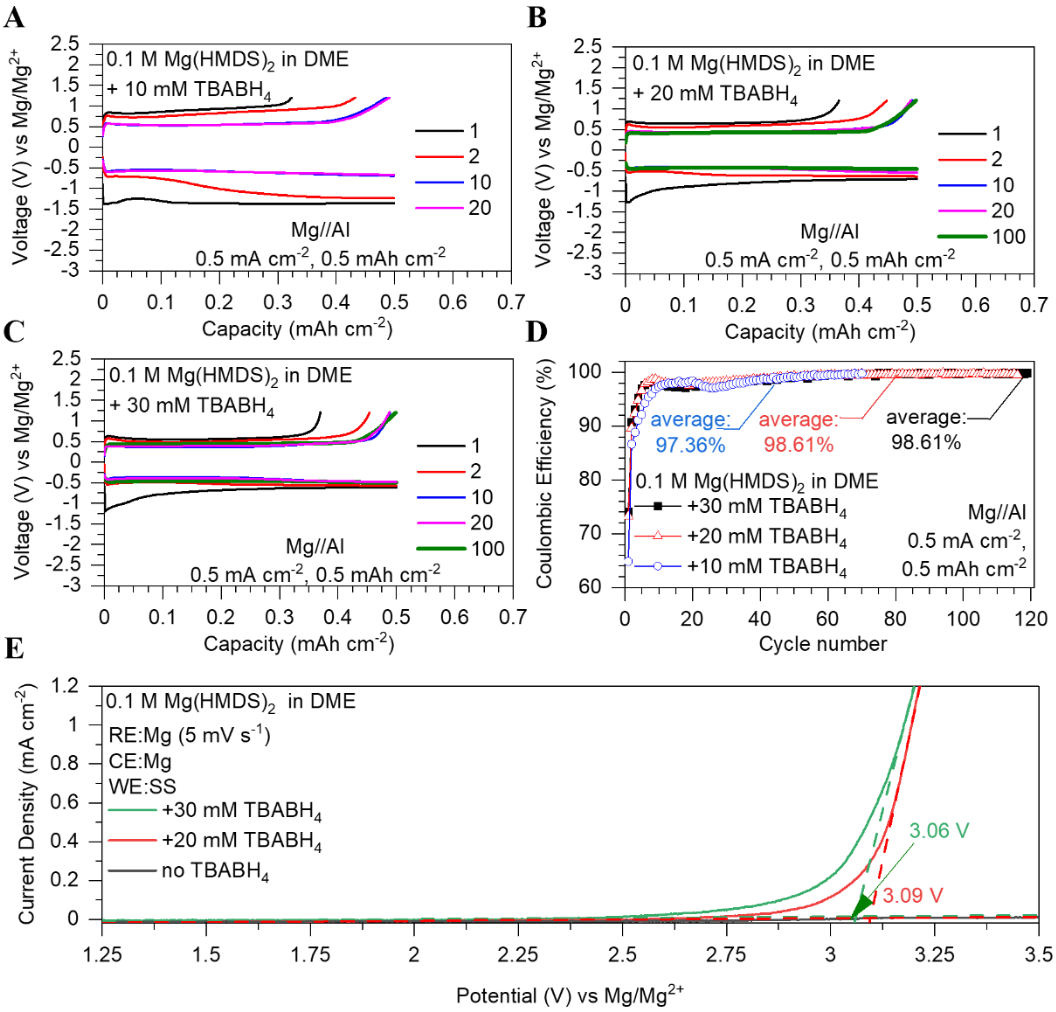

Figure 5.1.1: Magnesium Plating and stripping performance in Mg(HMDS)$_2$-based electrolyte at the varying amount of TBABH$_4$ concentration. (a, b and c) Capacity-Potential curves of 0.1 M Mg(HMDS)$_2$ in DME with 10, 20, and 30 mM of TBABH$_4$ respectively. (d) Coulombic efficiency of the electrolytes. (e) LSV measurement of stainless-steel electrode in Mg(HMDS)$_2$-based electrolyte with various concentrations of TBABH$_4$.

Furthermore, as mentioned in the previous chapter, chloride seems to induce corrosion on the non-noble current collector. In this section, it is further investigated if the corrosion process on the stainless-steel and aluminium current collector can be avoided by reducing the amount of chloride additive added to the electrolyte. For this purpose, 5 mM of $MgCl_2$ is added to the electrolyte. Although it was found previously that 30 mM of $MgCl_2$ could reduce the magnesium plating and stripping overpotential in the Mg(HMDS)$_2$-based electrolyte, a much lower concentration of 5 mM of $MgCl_2$ does not seem to produce a similar effect. As seen in figures 5.1.2 a and b, the plating and stripping overpotential and Coulombic efficiency are unchanged upon the addition of 5 mM $MgCl_2$. Thus, it can be inferred that the effectiveness of $MgCl_2$ is dependent on its concentration. Besides providing no benefit, the addition of 5 mM $MgCl_2$ is found to cause corrosion on the anode.

Figure 5.1.3 shows the LSV profile comparison of 0.1 M Mg(HMDS)$_2$ + 20 mM $TBABH_4$ in DME with and without the addition of 5 mM of $MgCl_2$. Stainless steel and aluminium electrodes are tested against each electrolyte in the experiment. The measurement indicates that on the stainless-steel electrode, the onset point of anodic current seems unchanged with the addition of 5 mM of $MgCl_2$ in the electrolyte. In contrast, the onset of the anodic current on aluminium increases ~2.56 V to ~2.75 V vs Mg/Mg^{2+}. The reason for the increased stability is unknown. This data may seem to indicate that a minuscule concentration of $MgCl_2$ does not induce corrosion. However, a more accurate determination of the anodic stability with chronoamperometry measurement shows otherwise.

Figures 5.1.3 b, c, d, e, f, and g show the chronoamperometry data. As seen in figures 5.1.3 b, the chloride-free electrolyte (0.1 M Mg(HMDS)$_2$ + 20 mM $TBABH_4$ in DME) has anodic stability of up to 2.75 V. Above 2.75 V, an anodic decomposition current flowing through the stainless-steel electrode would increase significantly. However, when the electrolyte is added with 5 mM of $MgCl_2$, it was found that the anodic current onset potential of the stainless-steel electrode would reduce significantly to 2.625 V vs Mg/Mg^{2+} (figure 5.1.3 c). This observation stands in contrast with the LSV data which indicates unchanged anodic stability on stainless steel. When the chronoamperometry duration is increased to 3 hours (figure 5.1.3 e), the anodic current in the chloride-containing electrolyte increases up to 0.2 mA cm^{-2}. Similarly, chronoamperometry tests with aluminium electrodes (figures 5.1.3 f and g) also indicate an increased anodic current in the chloride-containing electrolyte (0.1 M Mg(HMDS)$_2$ + 20 mM $TBABH_4$ + 5 mM $MgCl_2$ in DME) at 2.8 V vs Mg. The disparity in the anodic current is even higher at 3.0 V vs Mg/Mg^{2+}. This indicates that aluminium corrosion would occur in the chloride-containing electrolyte at around 2.8 V vs Mg/Mg^{2+}. It is worth noting that the low decomposition current during the chronoamperometry measurement of aluminium may be due to the surface film which develops on the aluminium electrode.

After the chronoamperometry measurement, the stainless-steel and aluminum electrodes are inspected using electron-microscopy (figure 5.1.4). It was found that corrosion pits are observed on the surface of the electrodes that were tested in the chloride-containing electrolyte. Meanwhile, the other electrode tested with the chloride-free electrolyte does not exhibit any corrosion pit on its surface. Instead, surface films are found to partly cover the electrode. This further proves that the current increase at the high potential in the chloride-based electrolyte is due to the corrosion process happening on the electrode.

To conclude the findings of this subsection, it is found that similar to the Mg(OTF)$_2$-based electrolyte, the Mg(HMDS)$_2$ in DME electrolyte performance is also affected by the concentration of TBABH$_4$ in the electrolyte. To significantly reduce the plating and stripping overpotential of the cell while maximizing the potential window of the electrolyte, the TBABH$_4$ concentration has to be in a certain sweet spot. Herein it is determined that 20 mM is the appropriate concentration. More importantly, this subsection further shows that chloride-based additive cannot be used to create a wide-potential window electrolyte (even if the amount of chloride added is minuscule). Furthermore, the data of this section also indicates that the corrosion onset potential of the current collectors cannot be accurately determined using LSV measurement. Instead, chronoamperometry measurement needs to be conducted as well to further validate the potential window of the electrolyte.

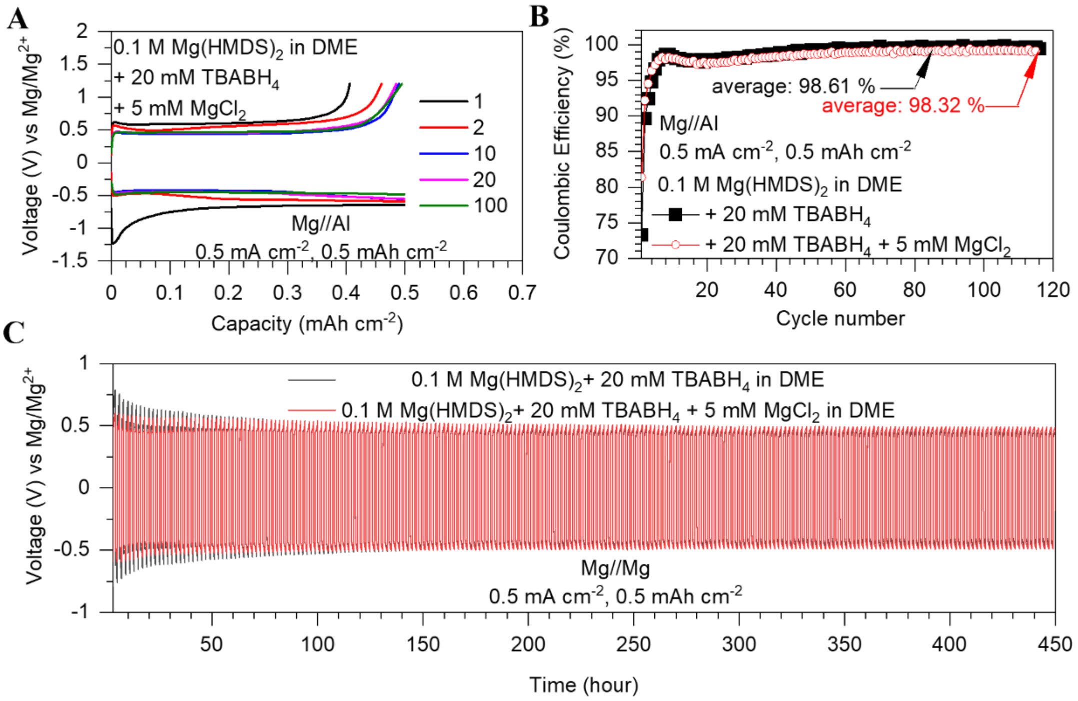

Figure 5.1.2: Magnesium plating and stripping process of Mg(HMDS)$_2$-based electrolyte with 5 mM of MgCl$_2$. (a) The Capacity-Potential curve of the electrolyte. (b) Coulombic efficiency

of the electrolyte. (c) Mg//Mg symmetric cell potential of the cell with the $Mg(HMDS)_2$-based electrolyte with 5 mM $MgCl_2$.

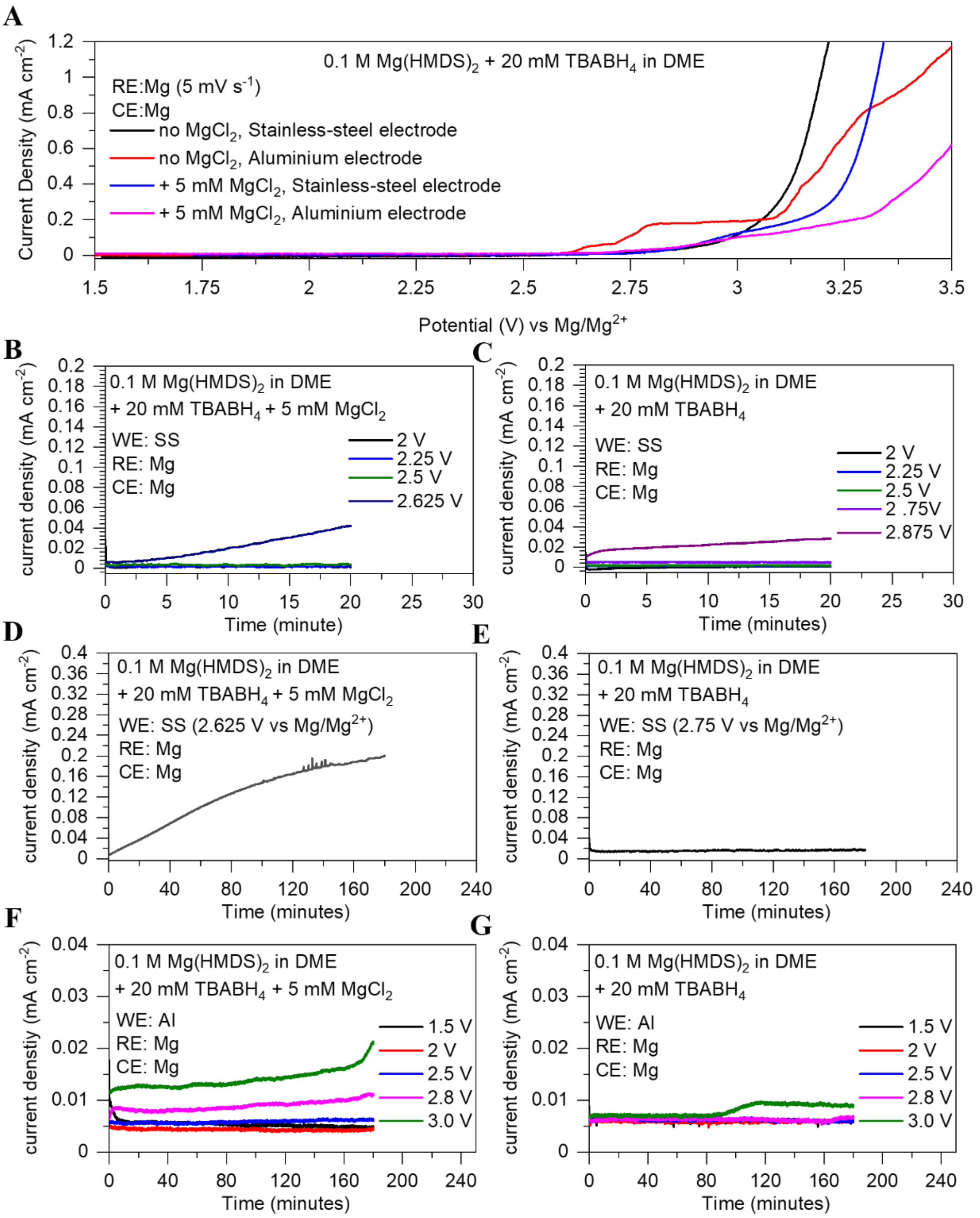

Figure 5.1.3: Anodic stability measurements of the electrolyte. (a) Linear Sweep Voltammetry of chloride-containing and chloride-free electrolytes against stainless-steel and aluminium electrodes. (b and c) Chronoamperometry of the stainless-steel electrodes at varying applied potential. (d and e) Chronoamperometry of the stainless-steel electrodes at the anodic limit of the electrolytes for 3 hours. (f and g) Chronoamperometry of the aluminium electrodes at the anodic limit of the electrolytes for 3 hours.

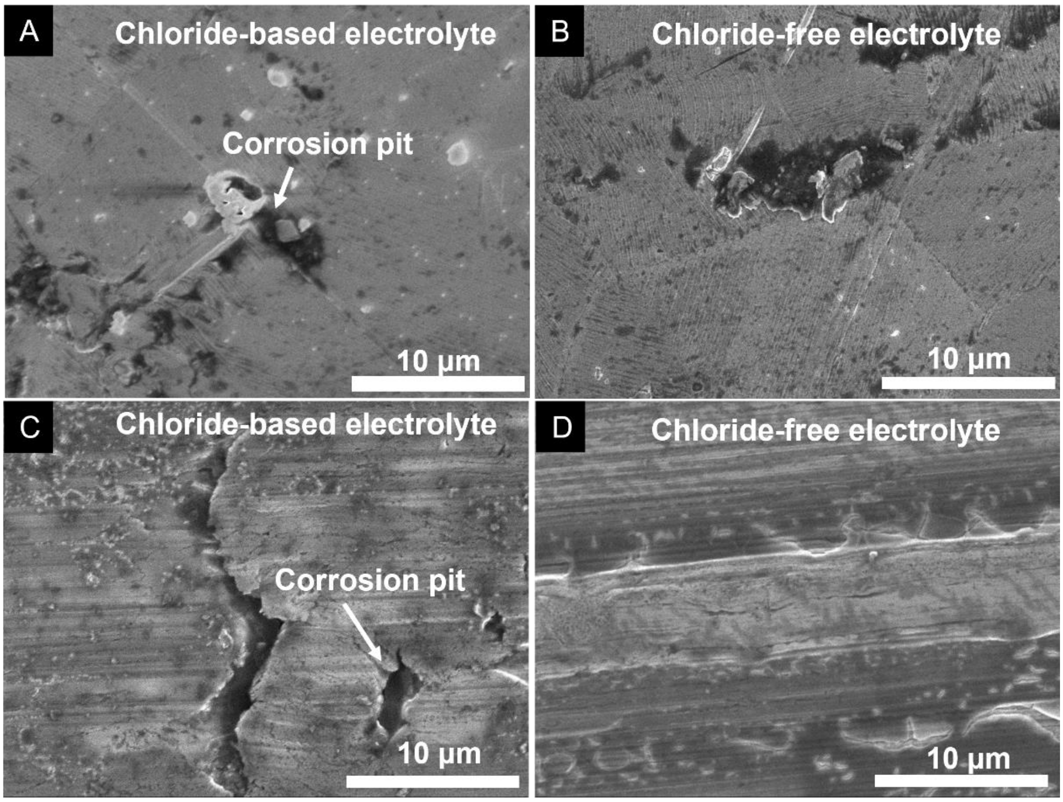

Figure 5.1.4: SEM analysis of the stainless steel and electrodes after the chronoamperometry measurement in Figures 5.1.3. (a) Corroded stainless steel in figure 5.1.3 d. (b) Stainless steel electrode in figure 5.1.3. e. (c) Corroded Aluminium electrode in figure 5.1.3. f. (d) Aluminium electrode in figure 5.1.3. g.

5.2 Establishing electrolyte solvent and appropriate Mg(HMDS)$_2$ concentration

Having determined the appropriate amount of TBABH$_4$, the study turned to a re-evaluation of the electrolyte solvent. Up until now, it has been shown that DME is a suitable solvent for Mg(HMDS)$_2$ electrolytes. However, high molecular weight ether is a more desirable solvent as these solvents have a higher boiling point and flash point than DME. Thus, if the DME solvent can be exchanged with other solvents, the thermal stability of the battery can be improved. In this section, several solvents were used as a replacement for the DME solvent. These are THF, diglyme, and high molecular weight ether such as triglyme and tetraglyme. Figure A7 shows the visual image of the electrolytes. The figure shows that the Mg(HMDS)$_2$ is well dissolved in all of these solvents at the concentration of 0.1 M. Figure 5.2.1 shows the capacity-potential profile of Mg//Al-C asymmetric half cells. Each cell consists of 0.1 M Mg(HMDS)$_2$ with 20 mM TBABH$_4$ that are dissolved in various solvents. The figure shows that all of these solvents are not suitable to create the $Mg(HMDS)_2$-based electrolyte. In general, the first magnesium plating overpotential of the $Mg(HMDS)_2$ in DME electrolyte is well below 1 V. In comparison, the plating overpotential of the electrolyte in other solvents is above that of 1 V. More importantly, short-circuit phenomena are observed in all of the cells. The observation, therefore, indicates that, unlike DME, these solvents induce non-homogenous deposition of magnesium. Figure A8, further affirms that the short-circuit occurrence is solvent-dependent. The experiment represented in the figure is the deposition process of magnesium with 0.1 $Mg(HMDS)_2$ with 80 mM $TBABH_4$ in triglyme. Despite using a high concentration of BH_4^- moisture scavenger, the experiment still indicates the formation of short-circuit during the magnesium plating process.

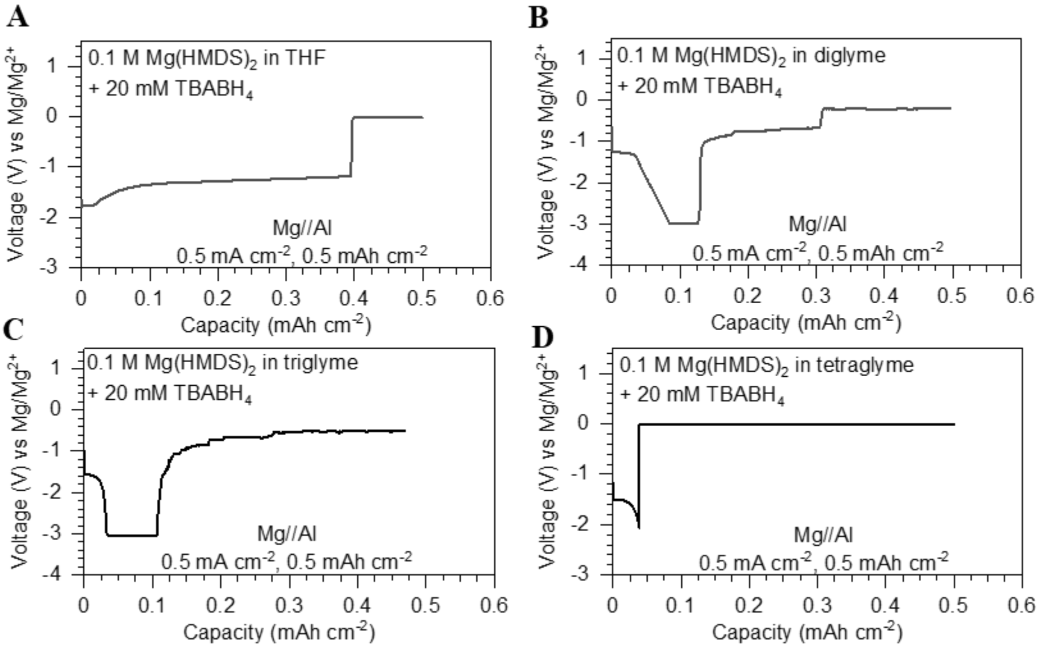

Figure 5.2.1: Magnesium plating process in 0.1 M $Mg(HMDS)_2$ electrolyte in various solvents (each with 20 mM of $TBABH_4$). Magnesium is plated in half cells with an applied current density of 0.5 mA cm^{-2}.

5.3 Further study on the $Mg(HMDS)_2$-based electrolyte

After establishing that DME is the most appropriate solvent for the electrolyte, the amount of $Mg(HMDS)_2$ in the electrolyte was varied. To further minimize the electrolyte's overpotential for magnesium plating and stripping, the concentration of the magnesium salt is increased to above 0.1 M. Figure A9 shows that $Mg(HMDS)_2$ is well dissolved in the range of 0.2 to 0.6 M. Figures 5.3.1 a, b, and c show the capacity-potential curves of 0.2, 0.4, and 0.6 M $Mg(HMDS)_2$ respectively. Generally, it was found that the plating and stripping overpotentials of the first magnesium plating and stripping cycle are independent of the $Mg(HMDS)_2$ concentration. However, the Coulombic efficiency of the first cycle decreases with the increase in $Mg(HMDS)_2$ concentration. 0.2 M $Mg(HMDS)_2$ in DME shows a first cycle CE of 68.38% while 0.4 M and 0.6 M of $Mg(HMDS)_2$ exhibited first cycle CE of 64.55% and 61.00% respectively (figure 5.3.1 d). This observation may indicate that the impurity content of the electrolyte increases with the $Mg(HMDS)_2$ (97% purity) concentration.

Upon further cycling of the half-cells, the Coulombic efficiency of the electrolytes increases for fifty cycles, as seen in figure 5.3.1 d. Furthermore, the plating and stripping overpotentials of the cells reduce with each cycle. When the plating and stripping overpotentials of the conditioned electrolytes were analyzed, it is found that the overpotentials of the magnesium half-cell reduce with increasing $Mg(HMDS)_2$ concentration. However, at high $Mg(HMDS)_2$ concentration (0.4-0.6 M), it is observed that the Coulombic efficiency of the electrolyte would decay after reaching its optimal value. The rapid CE decay at the end of the cell life causes the average Coulombic efficiency of the highly concentrated electrolyte to be low. 0.4 M $Mg(HMDS)_2$ and 0.6 M $Mg(HMDS)_2$ in DME for example have an average Coulombic efficiency of 97.04% and 97.86%.

Thus, to achieve high CE and low plating and stripping overpotential, the concentration of the $Mg(HMDS)_2$ electrolyte is fixed to 0.2 M. The optimized $Mg(HMDS)_2$ electrolyte was found to be highly compatible with the magnesium metal, allowing the symmetric magnesium half-cell to operate for up to 1000 cycles without short circuit (figure 5.3.1 e). The symmetric cell also shows a decreasing trend in the overpotential of the cell. In the first cycle of the symmetric cell, the plating and stripping overpotentials of the cell are higher than 0.5 V. This is consistent with the cell behavior in the asymmetric half-cell. After 250 cycles, the overpotentials of the plating and stripping process is 0.3 V, which is slightly higher than the cell overpotentials in the asymmetric half-cell after 150 cycles. As the cell cycling progresses to up to 1000 cycles, the plating and stripping overpotentials of the cell become 0.24 V. EIS measurement (Figure A10) of a Mg//Mg symmetric cell which was cycled in the electrolyte confirms that the charge-transfer resistance of the cell is reduced after each cycle of magnesium plating and stripping process.

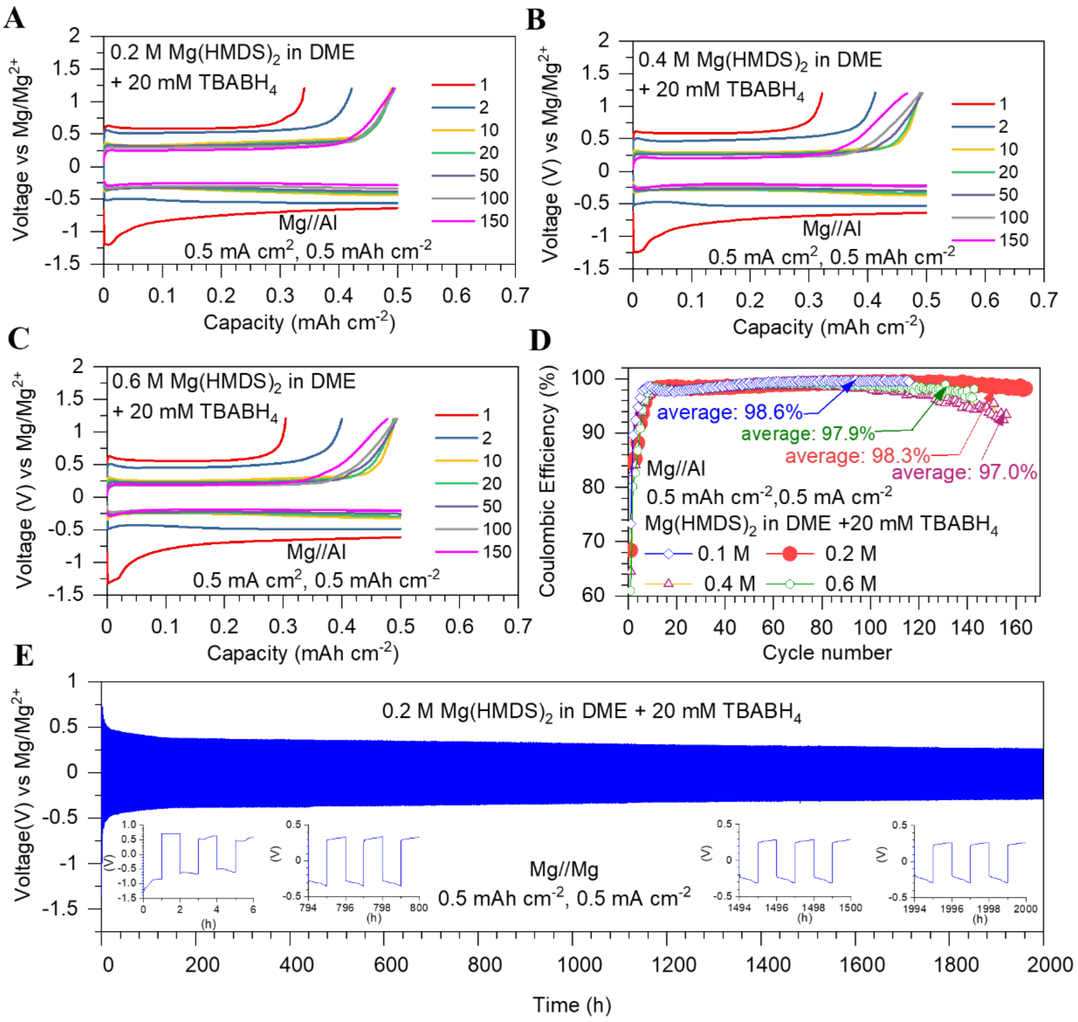

Figure 5.3.1: Magnesium plating and stripping process of 0.2 to 0.6 M Mg(HMDS)$_2$-based electrolyte. (a, b and c) Capacity-Potential profile of 0.2, 0.4 and 0.6 M Mg(HMDS)$_2$ in DME (each with 20 mM of TBABH$_4$). (d) Coulombic efficiency of the electrolytes. (e) Potential profile of Mg//Mg cell with 0.2 M Mg(HMDS)$_2$ and 20 mM TBABH$_4$ in DME.

Additional electrochemical half-cell characterization is provided in figure 5.3.2. The electrolyte is shown to be able to withstand high current density cycling wherein reversible plating and stripping could occur without any internal short-circuit within the current range of 0.1 to 1.5 mA cm^{-2} (figure 5.3.2 a). The overpotential of magnesium plating and stripping in the magnesium half-cell at various current density is as follow: 0.16 V at 0.1 mA cm^{-2}, 0.37 V at 0.5 mA cm^{-2}, 0.58 V at 1 mA cm^{-2}, and 0.91 V at 1.5 mA cm^{-2}. The Coulombic efficiency of the electrolyte in the current density range of 0.5 to 1.5 mA cm^{-2} is within the range of 97.7-98.4% after conditioning (figure 5.3.2

b). When the current density measurement is conducted in a symmetric cell, it is found that the maximum current density of the electrolyte is slightly higher than the asymmetric half-cell (Figure 5.3.2 c).

The magnesium plating and stripping process are also investigated at higher deposition capacity. Figures 5.3.2 d and e show the capacity-potential graph and Coulombic efficiency graphs of the asymmetric half-cell at various plating capacities from 0.1 to 2.0 mAh cm^{-2}. The plating capacity seems to slightly affect the magnesium plating and stripping overpotentials. Figure 5.3.2 d shows that on the 25th cycle, the magnesium plating and stripping overpotential is 0.39 V. This value is higher than the magnesium plating and stripping overpotentials of asymmetric half-cell that is cycled a lower constant plating capacity of 0.5 mAh cm^{-2} (given the same cycle number). Nevertheless, the Coulombic efficiency of the electrolyte remains high in the range of 97.4-98.4%. Across the 3 cells tested for the areal-capacity test, it is found that the minimum and maximum plating capacity before short-circuiting is 1.5 mAh cm^{-2} to 4.0 mAh cm^{-2}. To better ascertain the maximum plating capacity of the magnesium metal in the electrolyte, the plating and stripping process of the cell is conducted with increasing magnesium plating capacity in symmetric magnesium cells. From this experiment (figure 5.3.2 f), it is found that one of the cells shorted at 0.5 mAh cm^{-2}. However, the other 2 cells were able to achieve a higher plating capacity of 6.0 mAh cm^{-2} without any short-circuit. Thus, the magnesium plating capacity on magnesium metal is higher than on carbon-coated aluminium.

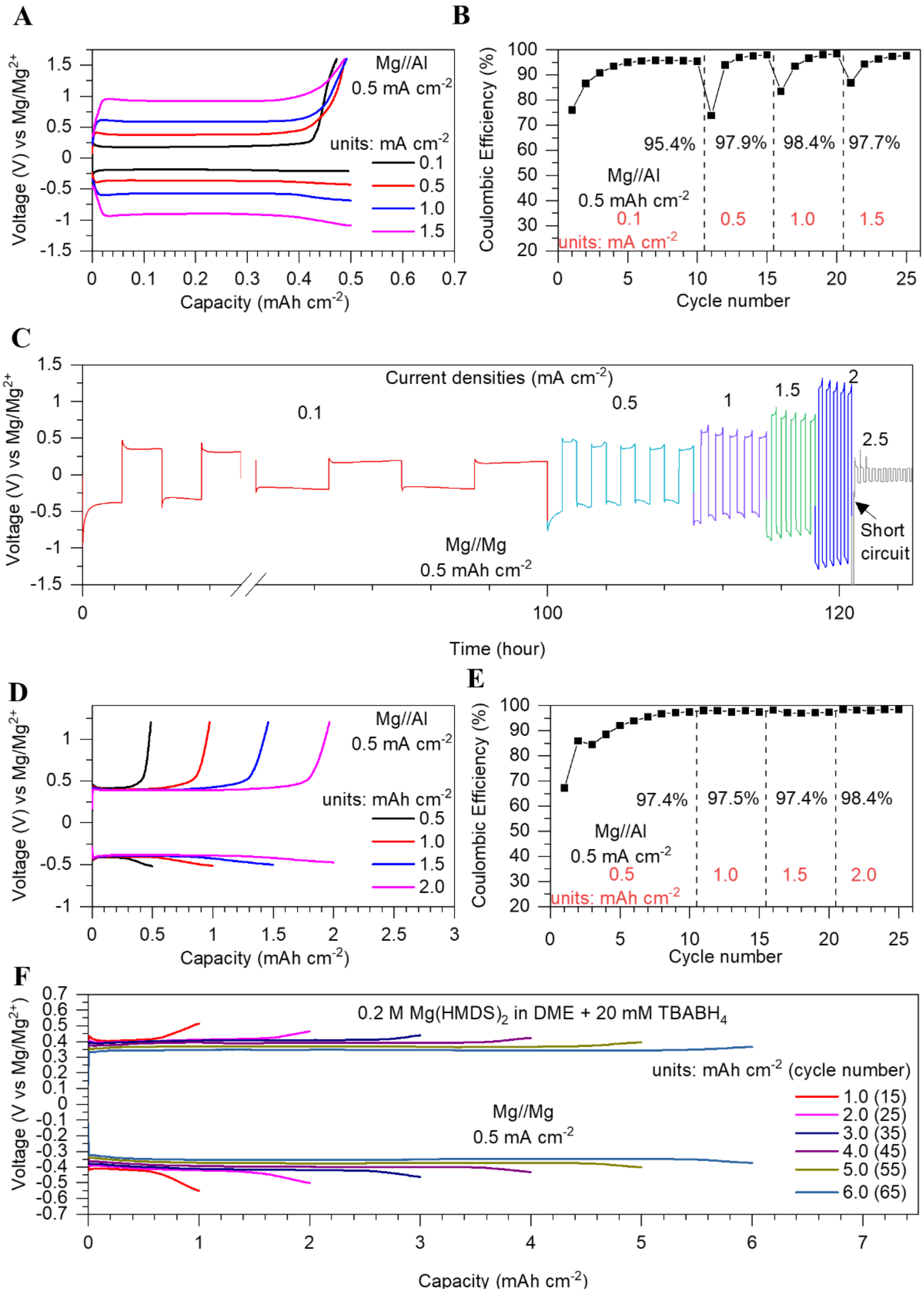

Figure 5.3.2: Further characterization of the magnesium plating and stripping process in the 0.2 M $Mg(HMDS)_2$ with 20 mM $TBABH_4$ in DME. (a) Capacity-Potential curve and (b) Coulombic efficiency of magnesium plating and stripping process in asymmetric half-cell at various applied current densities (0.1 to 1.5 mA cm^{-2}). (d) Capacity-Potential curve and (e) Coulombic efficiency of magnesium plating and stripping process in asymmetric half-cell at various areal capacities (0.5 to 1.5 mA cm^{-2}). (f) Capacity-Potential profile of Mg//Mg symmetric cell at various areal capacities from 1 to 5 mAh cm^{-2}.

5.4 Structure of the electroactive species of $Mg(HMDS)_2$ electrolyte in DME

After optimizing the $Mg(HMDS)_2$-based electrolyte formulation, the electroactive species of the electrolyte are analyzed. To ascertain the electroactive species in the electrolyte, Raman and single-crystal analysis is done on the $Mg(HMDS)_2$ in DME electrolyte. Firstly, to accurately determine the magnesium complex in the electrolyte. A highly concentrated $Mg(HMDS)_2$ in DME (1.67 M) is used to grow a single crystal of the $Mg(HMDS)_2$ complex in DME. Upon analyzing the crystal structure of the $Mg(HMDS)_2$ in the DME complex, it is found that the $Mg(HMDS)_2$ salt does not dissociate in the DME solvent (figure 5.4.1). As seen in the ball and stick representation of the $Mg(HMDS)_2$ crystal in DME, the Magnesium center atom is bonded to two $HMDS^-$ anions and the oxygen atoms of the DME molecule. The Magnesium complex, thus, exhibited tetrahedral coordination. The coordination structure of the electroactive species is also consistent with the findings of Schüler *et al.*[1], even though their crystallization process was done under a different condition.

The interaction of $Mg(HMDS)_2$ and $TBABH_4$ with DME solvent was investigated using Raman spectroscopy (Figure 5.4.2). The Raman spectrum of $Mg(HMDS)_2$ powder (Figure 5.4.2ii) shows two primary peaks at 617 cm^{-1} and 671 cm^{-1}, corresponding to one-dimensional symmetric vibration (A_{1g}) and two-dimensional representation (E_g) of Si-C bonds.[2, 3] The peak at 633 cm^{-1}, which disappears upon dissolving into solution, remains unknown due to the lack of reference data. Upon dissolving into DME, the A_{1g} and E_g symmetric vibration signals show a redshift to 614 cm^{-1} and 664 cm^{-1}, respectively. Notably, a new small peak at 869 cm^{-1} is attributed to engaging DME in the Mg^{2+} complex. It should be noted that the engaging DME in a fully dissociated Mg salt solution ($[Mg(DME)_3]^{2+}$) would show a signal at a higher wavenumber of 881 cm^{-1}.[4, 5] Hence, the signal at 869 cm^{-1} also indicates that the $Mg(HMDS)_2$ is not fully dissociated.[4] As the concentration of the $Mg(HMDS)_2$ in the solution is increased, no peaks of the Raman spectrum shifted. This indicates that the structure of the Magnesium complex remains unchanged with the salt concentration. In addition, the full Raman spectra of 0.1 M $Mg(HMDS)_2$ in DME without and with 20 mM $TBABH_4$ are unchanged (figure A11). This means that the $TBABH_4$ salt does not affect the speciation of the electroactive species in the electrolyte and merely functions as a moisture scavenger (this is likely due to the low concentration of $TBABH_4$ employed).

In previous reports, the Raman peak of the Si-C symmetric vibration would shift in position upon the dissociation of HMDS$^-$ from the Mg(HMDS)$_2$ complex to form new species.[2, 6] Given that the symmetric Si-C vibration signals of the Mg(HMDS)$_2$ are in the same position in DME or triglyme (Figure A12), it is proposed that the Mg(HMDS)$_2$ compound remains relatively undissociated in triglyme. This indicates that a general low dissociation rate of Mg(HMDS)$_2$ in various ether solvents such as THF[2], DME, or triglyme. Table A2 in the supplementary section shows the ionic conductivity of the optimum electrolyte to be 0.32 mS cm^{-1}. Given, that there is no significant difference in ionic conductivity between 0.2 M Mg(HMDS)$_2$ +20 mM TBABH$_4$ in DME and 0.1 M Mg(HMDS)$_2$ +20 mM TBABH$_4$ in DME (0.32 vs. 0.26 mS cm^{-1}), the ionic conductivity data further shows the low dissociation of Mg(HMDS)$_2$ complex in the solution.

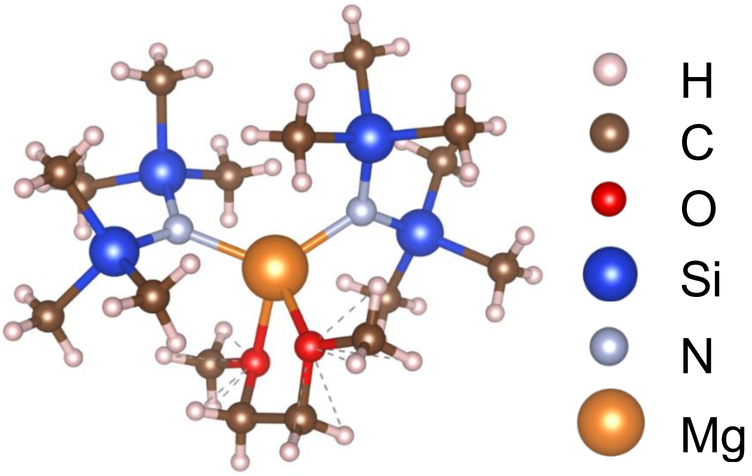

Figure 5.4.1: Structure of the magnesium complex in the Mg(HMDS)$_2$-based electrolyte.

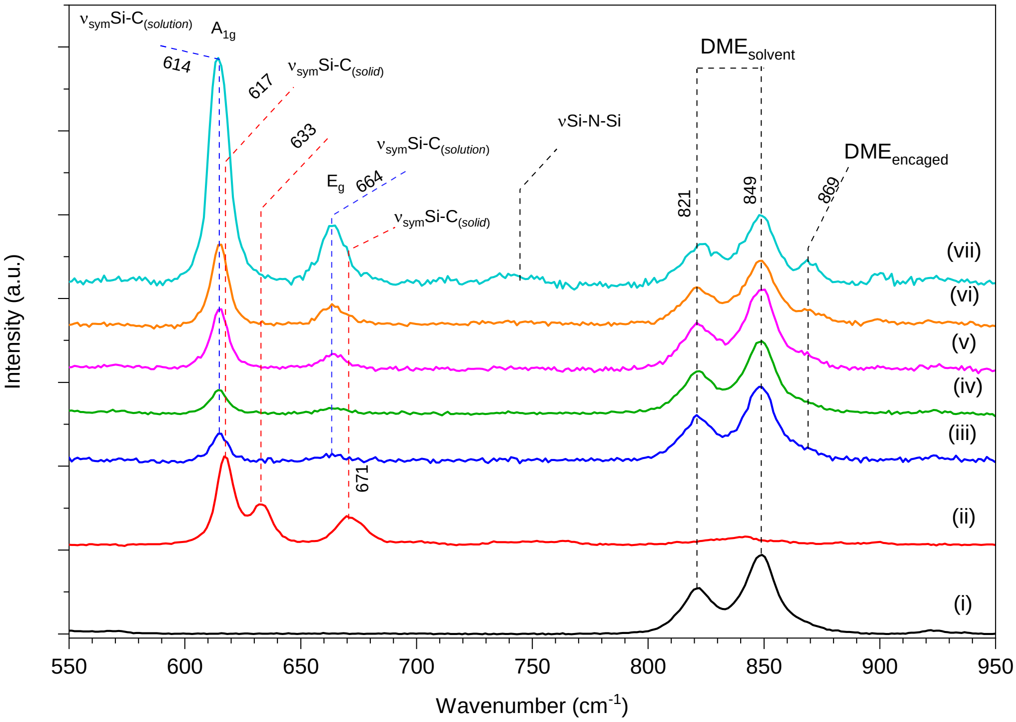

Figure 5.4.2: Raman spectroscopy of various Mg(HMDS)$_2$-based electrolyte. Raman spectroscopy of (i) pure DME, (ii) Mg(HMDS)$_2$ powder, (iii) 0.1 M Mg(HMDS)$_2$ in DME, (iv) 0.1 M Mg(HMDS)$_2$ + 20 mM TBABH$_4$ in DME, (v) 0.2 M Mg(HMDS)$_2$ in DME, (vi) 0.4 M Mg(HMDS)$_2$ in DME, (vii) 1 M Mg(HMDS)$_2$ in DME.

5.5 Chemical and morphological analysis of the electrochemically deposited magnesium from the electrolyte

To provide further additional evidence that the Mg(HMDS)$_2$-based electrolyte can deposit magnesium metal electrochemically, XRD analysis is conducted on a nickel substrate that has been deposited with magnesium in 0.2 M Mg(HMDS)$_2$ + 20 mM TBABH$_4$ in DME (plating current of 0.5 mA cm^{-2} for 5.5 hours). The XRD spectrum of the nickel substrate (figure 5.5.1 a) shows the existence of additional peaks which is attributed to the magnesium metal peak (PDF 00-001-1141). This observation further affirms that magnesium metal deposition occurs in the Mg(HMDS)$_2$-based electrolyte during the half-cell cycling tests shown before.

The morphology and chemical analysis of the electrochemically deposited magnesium from the electrolyte is also shown in figure 5.5.1 b and figure 5.5.1 c. The images show a homogeneous distribution of magnesium crystals with a non-dendritic morphology. EDS analysis of the deposit further confirms a high purity magnesium deposit (53.3-

73.1% wt.) with some carbon, oxygen, and silicon residue (figure 5.5.1 d). This likely indicates that a small amount of $Mg(HMDS)_2$ is decomposed during the cell cycling process. To further ascertain the morphology of the magnesium metal after 20 cycles of plating and stripping in the electrolyte, the cycled magnesium metal surface morphology is inspected using SEM in figure A14. Figure A14 a and figure A14 b show that the magnesium morphology on the surface of the anode is relatively flat and non-dendritic, affirming that the electrolyte is suitable for long-term cycling. It is noted, nevertheless, that some magnesium protrusion may develop on the surface of the magnesium anode after cycling in the electrolyte (figure A14 c and figure A14 d).

To identify the chemical constituent of the magnesium anode after multiple plating and stripping processes in the optimized electrolyte, XPS analysis (figure 5.5.2) was done on the cycled anode (20 cycles of plating and stripping at 0.5 mA cm^{-2} and 0.5 mAh cm^{-2}). The surface of the anodes shows the existence of Mg metal (49.8 eV[7-9]), MgO .[10-12] (Mg 2p 51.0 eV[7-9], O 1s 529.6 eV[7]), $Mg(OH)_2$ and/or $MgCO_3$ (Mg 2p 51.85 eV[9], O 1s 533.7 eV[8, 9, 13-15]), and elemental silicon (Si^0) (Si $2p_{3/2}$ 99.27 eV[7]). The O 1s peak at 531.3 eV is attributed to the existence of Oxygen vacancy in the MgO lattice.[10-12] Minor silane species can also be identified from the Si $2p_{3/2}$ peak at ~100.9 eV derived from the $Mg(HMDS)_2$ salt residue (figure A15). Further, A small peak at 283 eV and 48.6-48.2 eV also potentially indicates the existence of Mg-C bond[16] and the existence of dangling bonds on the surface of Mg-O[17], respectively. Besides these inorganic species, the C 1s spectrum also indicates the existence of organic species on the interphase, as indicated by the existence of C-O (285.8 eV[7, 18]), C=O (287.4 eV[7]), and C-C bonds (284.4 eV[7]). A small peak at 290.3 eV in the C 1s spectrum can potentially be assigned to $C_2O_4^{2-}$ and $MgCO_3$[7].

Analysis of the XPS spectra indicates that the anode-electrolyte interphase seems to be stratified into layers consisting of various components. Based on the XPS analysis presented, it is inferred that the anode-electrolyte interphase consists of two layers (figure 5.5.2 h). First, directly on top of the Magnesium crystal is the inorganic layer consisting of the native oxide and $Mg(OH)_2$, along with byproduct of $Mg(HMDS)_2$ decomposition (i.e. Si and Si-C). Between the first interphase layer and the electrolyte, lies the organic surface layer which is made from the decomposed DME solvent. Figure 5.5.2 e shows this to be true as evolution in the composition of the magnesium surface is observed upon argon etching. Mainly, it can be observed that the carbon concentration reduces significantly from 28.39% to 4.77%. This indicates that the top surface layer of the interphase consists mainly of organic species. Moreover, a clear increase in magnesium concentration from 27.87% to 47.22% upon surface etching is consistent with the removal of surface species and an increase in the signal from the Magnesium metal itself. The shift in organic to mainly inorganic constituents is also observed in the evolution of the O 1s spectrum wherein the peaks attributed to C-O or C=O bonds reduce while the intensity of MgO and $Mg(OH)_2$ peaks increases with etching time. An increase in the inorganic Si-based inorganic species was also found on the deeper part of the anode electrolyte interphase, as shown by the increase in the silicon content from 4.15 % to 8.04%. It is worth noting that the concentration of oxygen and silicon does not seem to reduce even after 60 minutes of argon etching. This indicates that inorganic species such as MgO, $Mg(OH)_2$, and elemental silicon are well incorporated with the electrochemically deposited magnesium.

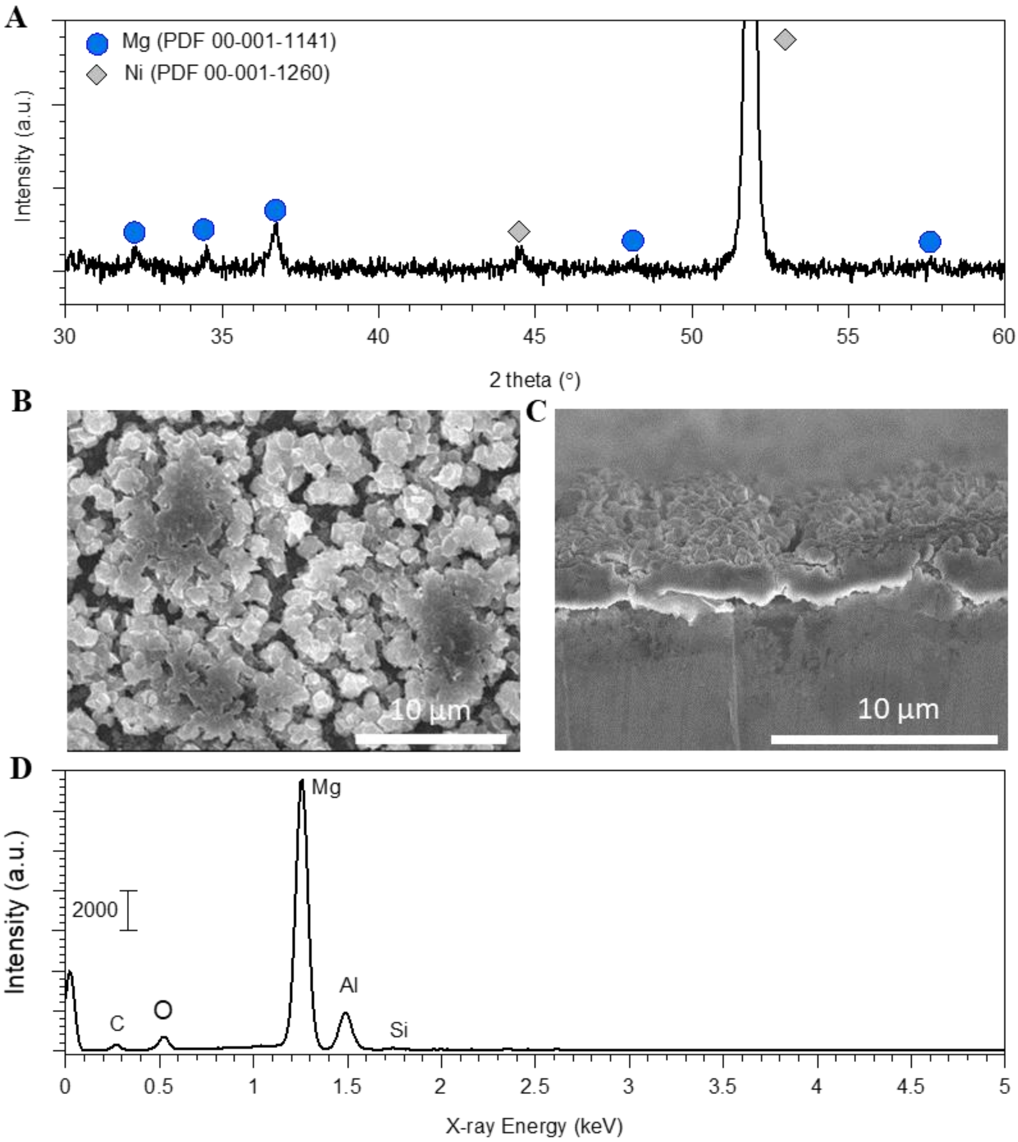

Figure 5.5.1: Characterization of the magnesium deposit from the magnesium plating process in the Mg(HMDS)$_2$-based electrolyte. (a) XRD signal of the Mg film on Nickel foil. (b and c) Lateral and cross-section image of the magnesium crystal deposited from the Mg(HMDS)$_2$-based electrolyte. (d) EDS spectrum of the magnesium crystal.

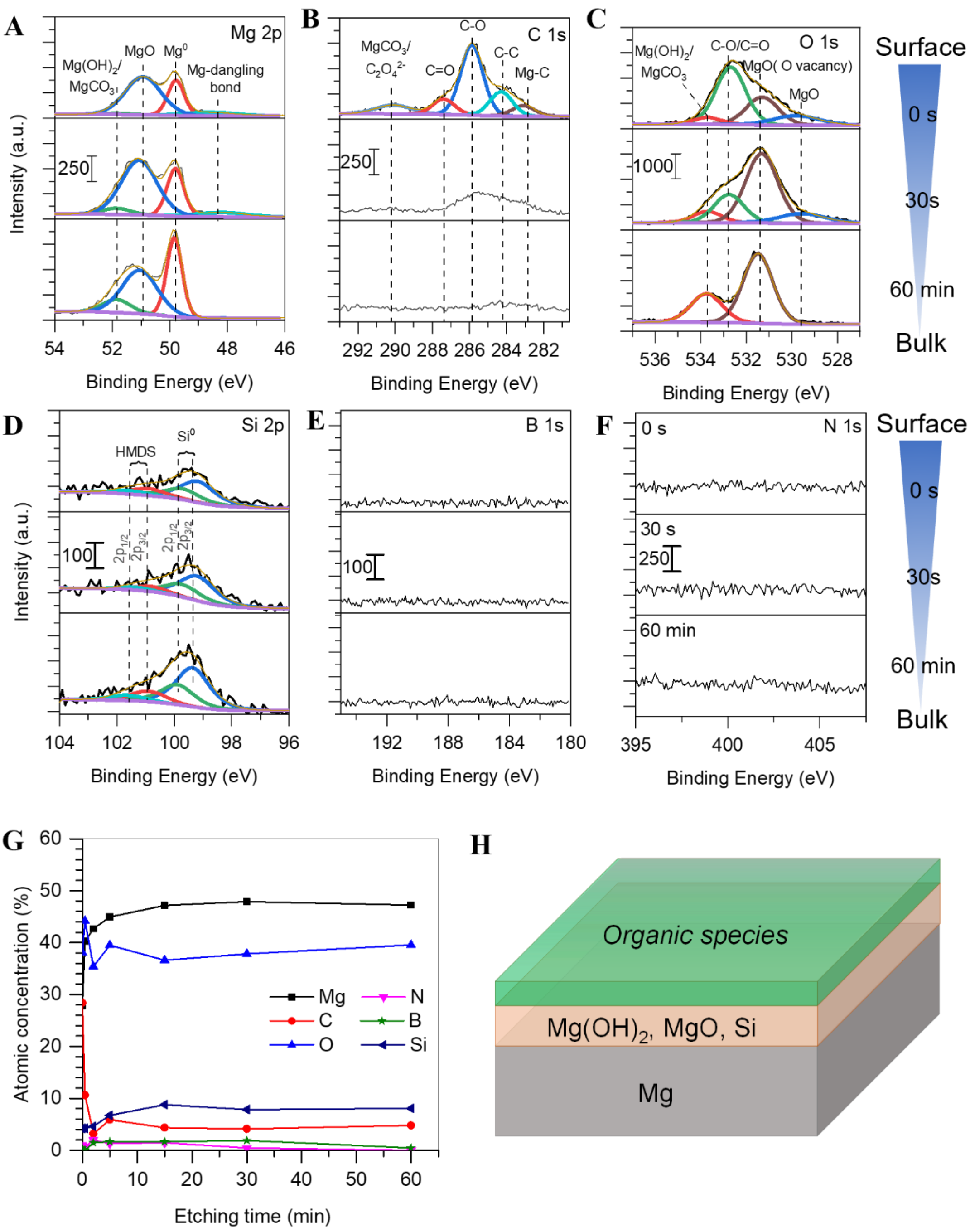

Figure 5.5.2: XPS analysis of the anode surface after several cycles of magnesium plating and stripping process. (a) Mg 2p, (b) C 1s, (c) O 1s, (d) Si 2p, (e) B 1s, (f) N 1s binding energy spectrum. (g) Quantitative analysis of the element concentrations on the magnesium anode at various levels of etching (h) Anode-electrolyte interphase on the surface of the magnesium anode. Time indication on the right side of the XPS spectra indicates various etching time used on the samples.

5.6 Anodic stability of the electrolyte

Before testing the compatibility of the electrolyte with various cathode materials, the anodic stability of the electrolyte has to be ascertained. In this section, the anodic stability of the electrolyte against stainless steel and aluminum is characterized by using linear sweep voltammetry and chronoamperometry. Based on the linear sweep voltammetry in figure 5.6.1a, it was found that the anodic current of the electrolyte is high on stainless steel and aluminium. Using the linear fit method[19] to determine the anodic decomposition onset potential, the anodic limit of the electrolyte on platinum, stainless steel and aluminium are determined to be 1.98 V, 3.18 V, and 2.54 V vs Mg respectively. It is worth noting, nevertheless, that a significant oxidation process occurs on Al after `~3 V.

Further, current leak measurements were also conducted to observe the current which indicates the decomposition rate of the electrolyte at various potential levels (vs. Mg/Mg^{2+}) over a long duration of time. It is observable that at an electrode potential of 2.8 V vs. Mg/Mg^{2+} or lower, the anodic decomposition current of the electrolyte on aluminium is maintained at a low level of lower than 10 µA cm^{-2} (figure 5.6.1 b). Similarly, against the stainless-steel electrode, the decomposition current of the electrolyte is maintained below 20 µA cm^{-2} at an electrode potential of 2.7 V vs. Mg/Mg^{2+} or lower (figure 5.6.1 c). The SEM image of the stainless-steel and aluminium foil after the chronoamperometry measurements (5.6.1 d and e) show that the electrodes are covered with a surface film originating from the decomposed electrolyte. The surface of the electrode also does not show signs of corrosion process occurring on the anode and the measurements indicate the high anodic stability of the electrolyte.

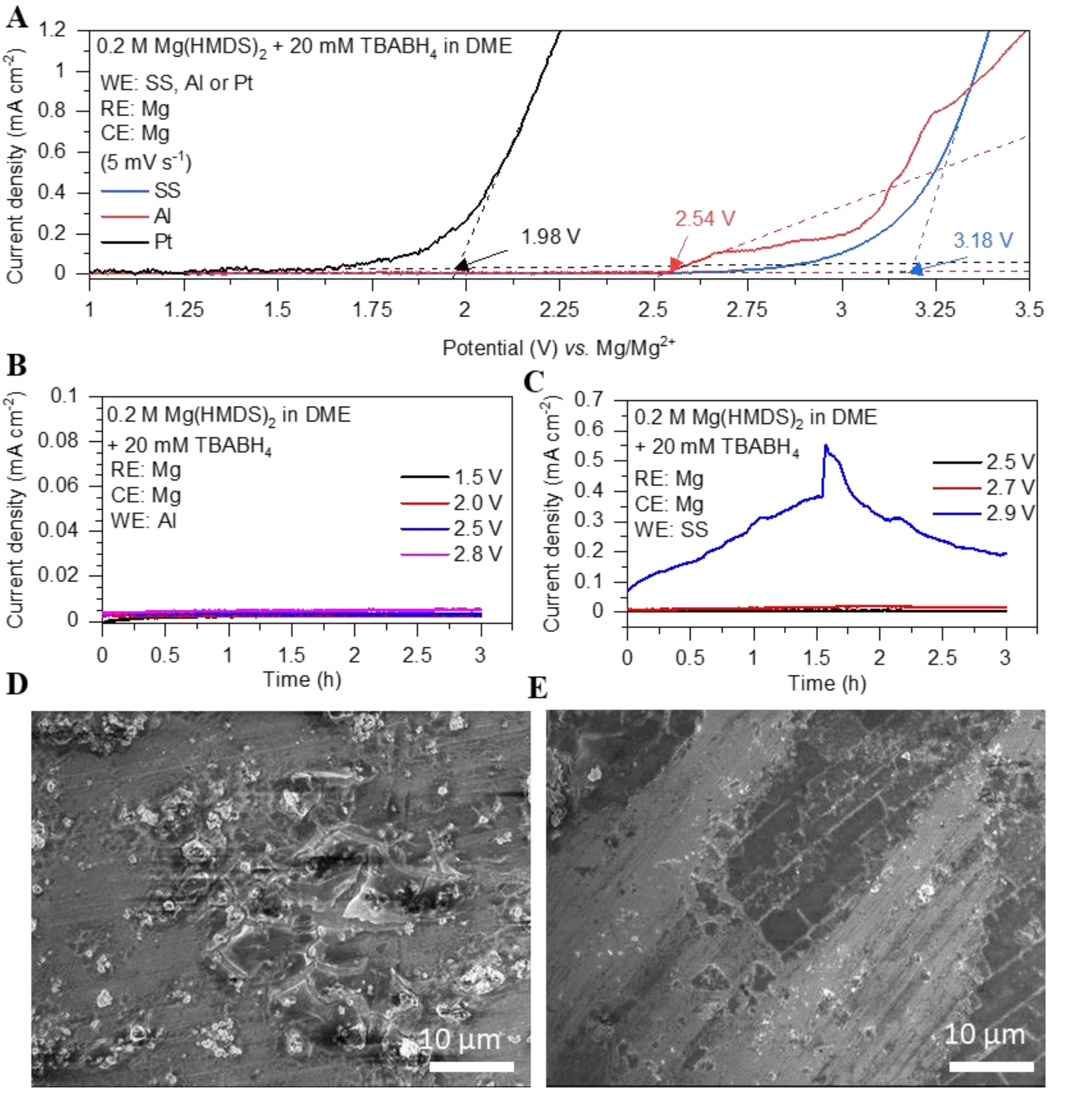

Figure 5.6.1: Anodic stability analysis of the 0.2 M $Mg(HMDS)_2$-based electrolyte. (a) LSV measurement of platinum, stainless steel, and aluminium electrodes in the electrolyte. (b and c) Chronoamperometry measurement of aluminium (b) and stainless-steel (c) electrodes at various potentials for 3 hours. (d and e) SEM analysis of the surface of aluminium (d) and stainless-steel (e) electrodes after the chronoamperometry measurements.

5.7 Full-cell cycling of the optimized electrolyte

To show the suitability of the electrolyte for battery application, this chapter discusses two prototypical magnesium batteries with several types of cathodes (S/MC, S-PAN, and CuS cathode). Sulfur-based cathodes such as short-chain sulfur in microporous carbon (S/MC) and S-PAN cathode are tested due to their high gravimetric capacity. In the experiments shown below (figure 5.7.1 a,b,c, and d), these cathodes are cycled at a low C-rate of 0.05 C for S/MC cathode and 0.01 C for S-PAN cathode.

The S/MC (figures 5.7.1 a and b) cathode shows the lowest discharge capacity (~2.5 mAh g^{-1} on the first cycle) although it has the best capacity retention. The low discharge capacity of S/MC likely indicates the low reactivity between the Mg(HMDS)$_2$.DME complex and the short-chain sulfur species. This observation is consistent with the sluggishness of the solid-state reaction between Magnesium ions with short-chain sulfur.[20] The high capacity retention of the S/MC cathode could be attributed to the low utilization of sulfur which allows for most of the active material to be unused in each discharge-charge cycling. This minimizes the capacity reduction as the parasitic reaction in the discharge and charge cycle does not affect most of the active material. The S-PAN cathode, on the other hand, shows higher discharge capacity (~56 mAh g^{-1} on the first cycle) with the magnesium electrolyte but exhibited a higher capacity degradation rate (figure 5.7.1 c and d). The discharge capacity of the S-PAN cathode may also be affected by the reactivity of the Mg(HMDS)$_2$.DME complex. Since the theoretical capacity of sulfur is 1672 mAh g^{-1},[20] The capacity utilization of the S/MC cathode and S-PAN cathode are too low for practical application.

Mo_6S_8, a common cathode known to conduct highly reversible magnesium intercalation/de-intercalation,[21] was also found to be incompatible with the Mg(HMDS)$_2$-based electrolyte. As seen in figure 5.7.1g, the discharge capacity of the Mo_6S_8 cathode is way higher than the maximum intercalation capacity of Mg^{2+} in Mo_6S_8 (129 mAh g^{-1}).[22] The over-discharge phenomenon may indicate that conversion reaction had occurred during the discharge process. Moreover, the charging plateau of the electrolyte Mg//Mo_6S_8 is also lower than 1 V. As the working potential of Mo_6S_8 is ~1 V vs Mg/Mg^{2+},[23, 24] the relatively low charge plateau potential is likely to be not related to Mo_6S_8 deintercalation. Instead, it may indicate an electrolyte decomposition process. Experiments had also been conducted on the cycling process of Mg//Mo_6S_8 in

0.1 M $Mg(HMDS)_2$ + 20 mM $TBABH_4$ in DME (figure A16). Despite being cycled at a low C-rate of 0.05 C, the cell seems to show poor discharge capacity. This indicates a general incompatibility of the $Mg(HMDS)_2$ electrolyte for Mo_6S_8 intercalation. A previous study by Attias *et al* shows the importance of chloride-based species in the intercalation process of the Mo_6S_8.[25] Given that Mo_6S_8 performs well chloride-containing $Mg(HMDS)_2$-based electrolytes,[26] the low performance of Mo_6S_8 in the chloride-free $Mg(HMDS)_2$-electrolyte indicates high activation energy barrier for the charge transfer process of Mo_6S_8 in the electrolyte.[25]

Only CuS cathode is shown to exhibit a good initial discharge capacity at 60 °C (figures 5.7.1 e and f). Nevertheless, overcharging seems to occur on the first cycle of the battery and the capacity of the cathode on the subsequent cycle reduces significantly. This overcharging behaviour could potentially be attributed to CuS dissolution during the charging process and increased electrolyte decomposition rate due to high cathode surface area. [27, 28] Previous publications indicate that CuS may produce polysulfide species that could potentially dissolve into the electrolyte and cause capacity fading.[29, 30] Previously, Feng *et al.* had incorporated reduced Graphene oxide into the composition of the CuS electrode. This modification was found to prevent CuS shuttling. The functional groups of Graphene oxide have also been shown to bind to polysulfide species and may prevent cathode dissolution in the electrolyte.[31] Moreover, Graphene oxide is known to be chemically reduced upon contact with BH_4^-, as indicated in several reports[32, 33]. Given that electrolyte decomposition may also be the possible failure mechanism for the cell, graphene oxide may be an effective component to combat the issue.

Taking inspiration from previous publications, a small amount of Graphene oxide is added to the surface of the glass fiber separator. By adding graphene oxide on the interphase between the glass fiber separator and the CuS cathode, an improvement in the cell discharge capacity was achieved (figure 5.7.2). With the application of graphene oxide on the separator, the cell was able to achieve an initial discharge capacity of 261.5 mAh g^{-1} (46.7% of the cathode theoretical capacity, 560 mAh g^{-1}). Importantly, the overcharge behaviour in the first cycle is reduced even though the charging cut-off potential has been increased to 2.0 V. This corroborates the effectiveness of graphene oxide in reducing cell overcharge. Figure A17 shows other CuS replicate cells which also shows even lower overcharge behaviour.

There are several possible working mechanisms of the graphene oxide layer in the cell. Given that the cell is also allowed to rest for 6 hours at 60 °C, it is likely that the BH_4^- moieties in the $Mg(HMDS)_2$ based electrolyte reacts with graphene oxide on the separator during the cell resting stage. As a consequence, the concentration of BH_4^- in the electrolyte would be reduced and the anodic decomposition of BH_4^- during the cell-charging stage will be inhibited. Thus, the cell overcharging behavior in the Mg-CuS cell becomes less severe when the graphene oxide coating is used. The graphene oxide layer may also act as a conductive framework which increases the discharge capacity of the cell and prevents CuS dissolution, thereby reducing the cathode capacity fade.[29] Nevertheless, large capacity degradation is still exhibited by the CuS cell. This issue may arise from several phenomena commonly find in conversion cathodes such as cathode pulverization and the dissolution of the active material into the electrolyte. [27, 34-36] To improve the cell performance, future works may focus on better CuS cathode engineering such as size reduction[37], using nanocage CuS nanomaterial to accommodate for the volumetric expansion during the battery discharge[38], or the incorporation of graphene oxide into the CuS cathode composite[29].

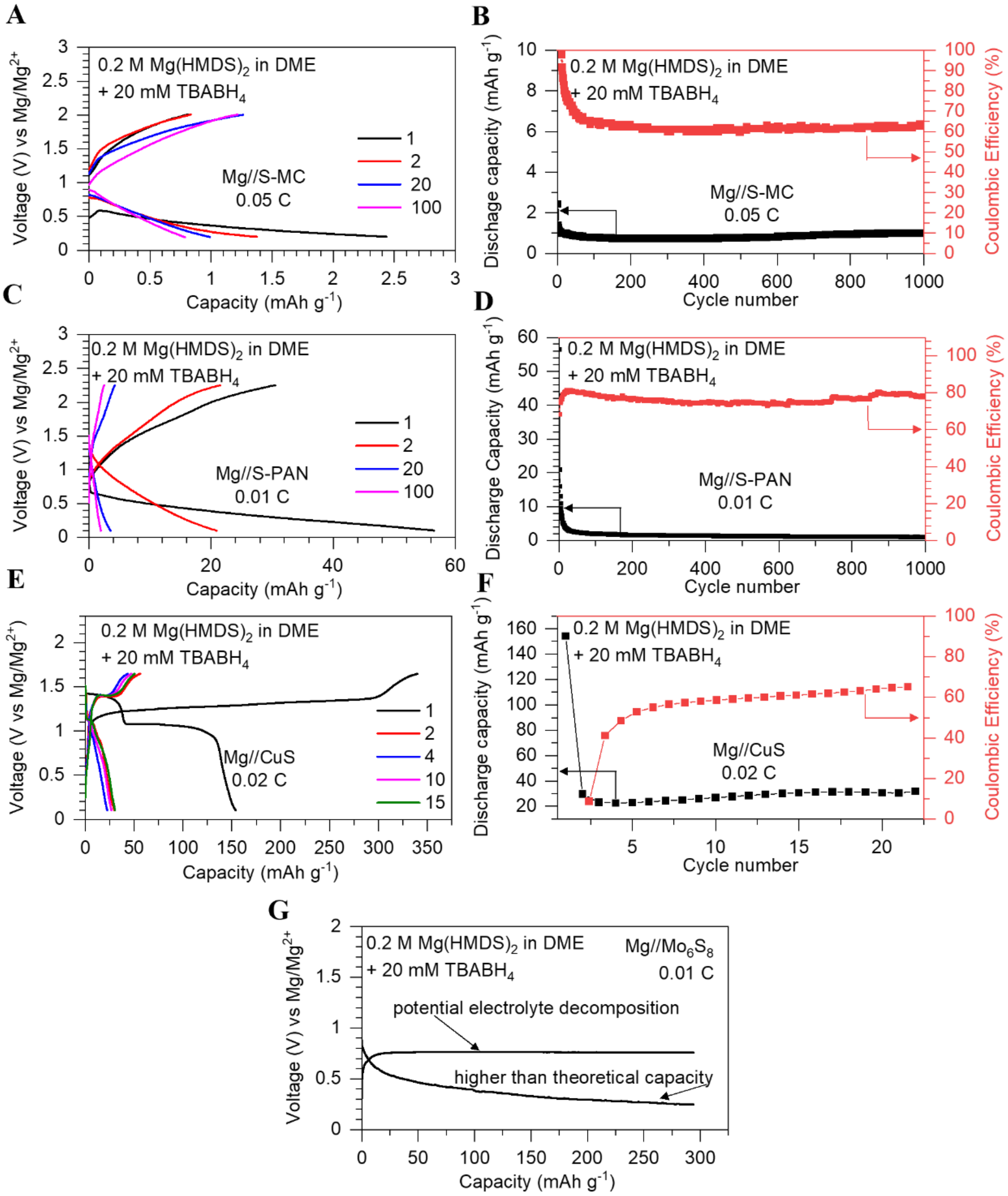

Figure 5.7.1: Full cell performance of various cathodes in 0.2 M Mg(HMDS)$_2$ + 20 mM TBABH$_4$ in DME. (a and b) Capacity-Potential profile graph and Discharge capacity plot of S-MC cathode respectively. (c and d) Capacity-Potential profile graph and Discharge capacity plot of S-PAN cathode respectively. (e and f) Capacity-Potential profile graph and Discharge capacity plot of CuS cathode respectively. (g) Capacity-Potential profile graph of Mo$_6$S$_8$ cells. Each cathode film was coated on carbon-coated aluminium film.

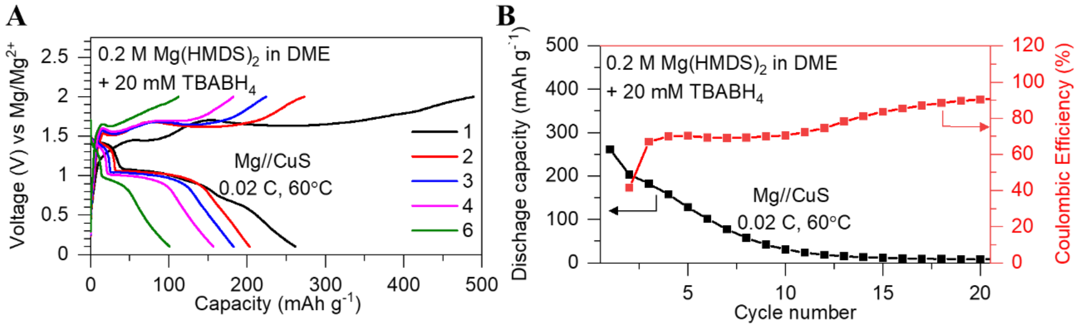

Figure 5.7.2: Mg//CuS cycling performance with graphene oxide coated separator. (a) Capacity-Potential profiles of the cell for 6 cycles. (b) Discharge capacity and Coulombic efficiency of the cell for 20 cycles. The cathode was coated on carbon-coated aluminium foil.

5.8 Conclusion

After studying the appropriate concentration of additives, salt, and type of solvent, it was established that 0.2 M Mg(HMDS)$_2$ dissolved in DME with the addition of 20 mM TBABH$_4$ is the optimum formulation of chloride-free Mg(HMDS)$_2$-based electrolyte. The electrolyte exhibit an average Coulombic efficiency of 98.3% (at 0.5 mA cm^{-2}, 0.5 mAh cm^{-2}) and was able to cycle for 1000 cycles without short-circuiting. Moreover, the electrolyte enables short-circuit free battery cycling up to an applied current density of 2.0 mA cm^{-2} (at 0.5 mA cm^{-2}) and an applied areal capacity of 6 mAh cm^{-2} (at 0.5 mA cm^{-2}).

Analysis of the magnesium complex structure in the electrolyte show that the Mg(HMDS)$_2$ salt does not dissociate in the electrolyte. This observation is consistent with the electrolyte's low ionic conductivity (0.32 mS cm^{-1}). The TBABH$_4$ concentration in the electrolyte is also relatively low to establish any change in the Raman spectrum of the electrolyte. Thus, the TBABH$_4$ does not seem to cause changes in the chemical speciation of the magnesium complex. The morphology of the electrochemically deposited magnesium crystal is established to be non-dendritic and homogenous magnesium deposition can also be obtained from the electrolyte. Moreover, it was further established that Mg(HMDS)$_2$ is relatively stable as little sign of Mg(HMDS)$_2$ decomposition is observed from the magnesium anode after several cycles of plating and stripping. The structure of the magnesium-electrolyte interphase has also been investigated with XPS and it was discovered that the interphase consists of an organic surface layer with an inorganic layer consisting of MgO, Mg(OH)$_2$, Si, and silane underneath the organic layer.

The anodic stability of the electrolyte was found to be 2.7 and 2.8 V vs Mg on stainless steel and aluminium, respectively. Crucially, the application of the Mg(HMDS)$_2$-based electrolyte for a full cell application has been investigated for Mg//S and Mg//CuS cells. This test indicates that good compatibility between CuS cathode and Mg(HMDS)$_2$ can be expected, at least in a high-temperature environment of 60°C.

References

1. Schüler, P.; Görls, H.; Westerhausen, M.; Krieck, S., Bis(trimethylsilyl)amide Complexes of s-Block Metals with Bidentate Ether and Amine Ligands. *Dalton Trans.* **2019,** *48*, 8966-8975.
2. Merrill, L. C.; Schaefer, J. L., Electrochemical Properties and Speciation in Mg(HMDS)$_2$-Based Electrolytes for Magnesium Batteries as a Function of Ethereal Solvent Type and Temperature. *Langmuir* **2017,** *33*, 9426-9433.
3. E. A. ROBINSON, K. H., The Vibrational Spectra and Structures of Hexachlorodisilazane and Hexamethyldisilazane. *Sci. Bull. Fac. Educ, Nagasaki Univ.,* **1972,** *23*, 69-73.
4. Salama, M.; Shterenberg, I.; J.W. Shimon, L.; Keinan-Adamsky, K.; Afri, M.; Gofer, Y.; Aurbach, D., Structural Analysis of Magnesium Chloride Complexes in Dimethoxyethane Solutions in the Context of Mg Batteries Research. *J. Phys. Chem. C* **2017,** *121*, 24909-24918.
5. Nguyen, D.-T.; Eng, A. Y. S.; Ng, M.-F.; Kumar, V.; Sofer, Z.; Handoko, A. D.; Subramanian, G. S.; Seh, Z. W., A High-Performance Magnesium Triflate-Based Electrolyte for Rechargeable Magnesium Batteries *Cell Rep. Phys. Sci.* **2020**.
6. Kim, S. S.; See, K. A., Activating Magnesium Electrolytes through Chemical Generation of Free Chloride and Removal of Trace Water. *ACS Appl. Mater. Interfaces* **2021,** *13*, 671-680.
7. Naumkin, A. V.; Kraut-Vass, A.; Gaarenstroom, S. W.; Powell, C. J. NIST X-ray Photoelectron Spectroscopy Database. https://srdata.nist.gov/xps/Default.aspx (accessed 22 August 2021).
8. Burke, P. J.; Bayindir, Z.; Kipouros, G. J., X-Ray Photoelectron Spectroscopy (XPS) Investigation of the Surface Film on Magnesium Powders. *Appl. Spectrosc.* **2012,** *66*, 510-518.

9. Christ, B. V., *Handbook of Monochromatic XPS Spectra: The Elements and Native Oxides*. XPS International: Salem (OR), 1999; Vol. 1, p 511.

10. Vasilyeva, I. G.; Vikulova, E. S.; Morozova, N. B.; Pochtar, A. A.; Igumenov, I. K., Invisible Surface Oxygen Vacancies in a Thin MgO Film: Impacts on the Chemical Activity and Secondary Electron Emission. *Inorg. Chem.* **2020,** *59,* 17999-18009.

11. Li, J.-M.; Hu, Y.-B., O_2 Atmospheric Annealing-Tunable Defects in Ionic Oxide MgO Nanoribbons. *Appl. Phys. Lett.* **2019,** *114,* 203101.

12. Jiang, G.; Liu, A.; Liu, G.; Zhu, C.; Meng, Y.; Shin, B.; Fortunato, E.; Martins, R.; Shan, F., Solution-Processed High-K Magnesium Oxide Dielectrics for Low-Voltage Oxide Thin-Film Transistors. *Appl. Phys. Lett.* **2016,** *109,* 183508.

13. Peng, X. D.; Barteau, M. A., Characterization of Oxide Layers on Mg(0001) And Comparison of H_2O Adsorption on Surface and Bulk Oxides. *Surf. Sci.* **1990,** *233,* 283-292.

14. Yao, H. B.; Li, Y.; Wee, A. T. S., An XPS Investigation of the Oxidation/Corrosion of Melt-Spun Mg. *Appl. Surf. Sci.* **2000,** *158,* 112-119.

15. Casey, P.; Hughes, G.; O'Connor, E.; Long, R. D.; Hurley, P. K., Growth and Characterisation of Thin MgO Layers on Si(100) Surfaces. *J. Phys. Conf. Ser.* **2008,** *100,* 042046.

16. Yoo, H. D.; Han, S.-D.; Bolotin, I. L.; Nolis, G. M.; Bayliss, R. D.; Burrell, A. K.; Vaughey, J. T.; Cabana, J., Degradation Mechanisms of Magnesium Metal Anodes in Electrolytes Based on $(CF_3SO_1)_2N^-$ at High Current Densities. *Langmuir* **2017,** *33,* 9398-9406.

17. Kamarulzaman, N.; Chayed, N. F.; Badar, N.; Kasim, M. F.; Mustaffa, D. T.; Elong, K.; Rusdi, R.; Oikawa, T.; Furukawa, H., Band Gap Narrowing of 2-D Ultra-Thin MgO Graphene-Like Sheets. *ECS J. Solid State Sci. Technol.* **2016,** *5,* Q3038-Q3045.

18. Blanco, A. A. G.; Rocha, J. V.; Múnera, J. F.; Nazzarro, M.; Zgrablich, G.; Sapag, K., A Study of the Adsorption Properties of Single Walled Carbon Nanotubes Treated with Nitric Acid. *Adsorpt. Sci. Technol.* **2011,** *29,* 705-722.

19. Mousavi, M. P.; Dittmer, A. J.; Wilson, B. E.; Hu, J.; Stein, A.; Bühlmann, P., Unbiased Quantification of the Electrochemical Stability Limits of Electrolytes and Ionic Liquids. *J. Electrochem. Soc.* **2015,** *162,* A2250.

20. Nguyen, D.-T.; Horia, R.; Eng, A. Y. S.; Song, S.-W.; Seh, Z. W., Material Design Strategies to Improve the Performance of Rechargeable Magnesium−Sulfur Batteries. *Mater. Horiz.* **2021,** *8,* 830-853.

21. Song, J.; Sahadeo, E.; Noked, M.; Lee, S. B., Mapping the Challenges of Magnesium Battery. *J. Phys. Chem. Lett.* **2016,** *7,* 1736-1749.

22. Canepa, P.; Sai Gautam, G.; Hannah, D. C.; Malik, R.; Liu, M.; Gallagher, K. G.; Persson, K. A.; Ceder, G., Odyssey of Multivalent Cathode Materials: Open Questions and Future Challenges. *Chem. Rev.* **2017,** *117,* 4287-4341.

23. Thöle, F.; Wan, L. F.; Prendergast, D., Re-examining the Chevrel phase Mo6S8 cathode for Mg intercalation from an electronic structure perspective. *PCCP* **2015,** *17,* 22548-22551.

24. Liu, F.; Wang, T.; Liu, X.; Fan, L. Z., Challenges and Recent Progress on Key Materials for Rechargeable Magnesium Batteries. *Adv. Energy Mater.* **2020,** *11,* 2000787.

25. Attias, R.; Chae, M. S.; Dlugatch, B.; Oliel, M.; Goffer, Y.; Aurbach, D., The Role of Surface Adsorbed Cl– Complexes in Rechargeable Magnesium Batteries. *ACS Catal.* **2020,** *10,* 7773-7784.

26. Zhao-Karger, Z.; Zhao, X.; Fuhr, O.; Fichtner, M., Bisamide Based Non-Nucleophilic Electrolytes for Rechargeable Magnesium Batteries. *RSC Adv.* **2013,** *3,* 16330-16335.

27. Duffort, V.; Sun, X.; Nazar, L. F., Screening for Positive Electrodes for Magnesium Batteries: A Protocol for Studies at Elevated Temperatures. *Chem. Commun.* **2016,** *52,* 12458-12461.

28. Lipson, A. L.; Han, S.-D.; Pan, B.; See, K. A.; Gewirth, A. A.; Liao, C.; Vaughey, J. T.; Ingram, B. J., Practical Stability Limits of Magnesium Electrolytes. *J. Electrochem. Soc.* **2016,** *163,* A2253-A2257.

29. Feng, C.; Zhang, L.; Yang, M.; Song, X.; Zhao, H.; Jia, Z.; Sun, K.; Liu, G., One-Pot Synthesis of Copper Sulfide Nanowires/Reduced Graphene Oxide Nanocomposites with Excellent Lithium-Storage Properties as Anode Materials for Lithium-Ion Batteries. *ACS Appl. Mater. Interfaces* **2015,** *7,* 15726-15734.

30. Wu, M.; Zhang, Y.; Wu, H.; Qin, A.; Li, X.; Shen, J.; Chen, Z.; Cao, S.-a.; Li, T.; Xu, F., Cu9S5 Nanoflower Cathode for Mg Secondary Batteries: High Performance and Reaction Mechanism. *Energy Technology* **2019,** *7,* 1800777.

31. Ji, L.; Rao, M.; Zheng, H.; Zhang, L.; Li, Y.; Duan, W.; Guo, J.; Cairns, E. J.; Zhang, Y., Graphene Oxide as a Sulfur Immobilizer in High Performance Lithium/Sulfur Cells. *J. Am. Chem. Soc.* **2011,** *133,* 18522-18525.

32. Shin, H.-J.; Kim, K. K.; Benayad, A.; Yoon, S.-M.; Park, H. K.; Jung, I.-S.; Jin, M. H.; Jeong, H.-K.; Kim, J. M.; Choi, J.-Y.; Lee, Y. H., Efficient Reduction of Graphite Oxide by Sodium Borohydride and Its Effect on Electrical Conductance. *Adv. Funct. Mater.* **2009,** *19*, 1987-1992.

33. Muda, M. R.; Ramli, M. M.; Isa, S. S. M.; Jamlos, M. F.; Murad, S. A. Z.; Norhanisah, Z.; Isa, M. M.; Kasjoo, S. R.; Ahmad, N.; Nor, N. I. M.; Khalid, N., Fundamental study of reduction graphene oxide by sodium borohydride for gas sensor application. *AIP Conf. Proc.* **2017,** *1808,* 020034.

34. Blanc, L. E.; Sun, X.; Shyamsunder, A.; Duffort, V.; Nazar, L. F., Direct Nano-Synthesis Methods Notably Benefit Mg-Battery Cathode Performance. *Small Methods* **2020,** *4*, 2000029.

35. Zhang, Z.; Dong, S.; Cui, Z.; Du, A.; Li, G.; Cui, G., Rechargeable Magnesium Batteries using Conversion-Type Cathodes: A Perspective and Minireview. *Small Methods* **2018,** *2*, 1800020.

36. Wu, F.; Yushin, G., Conversion Cathodes for Rechargeable Lithium and Lithium-Ion Batteries. *Energy Environ. Sci.* **2017,** *10*, 435-459.

37. Kravchyk, K. V.; Widmer, R.; Erni, R.; Dubey, R. J. C.; Krumeich, F.; Kovalenko, M. V.; Bodnarchuk, M. I., Copper Sulfide Nanoparticles as High-Performance Cathode Materials for Mg-Ion Batteries. *Sci. Rep.* **2019,** *9*, 7988.

38. Du, C.; Zhu, Y.; Wang, Z.; Wang, L.; Younas, W.; Ma, X.; Cao, C., Cuprous Self-Doping Regulated Mesoporous CuS Nanotube Cathode Materials for Rechargeable Magnesium Batteries. *ACS Appl. Mater. Interfaces* **2020,** *12*, 35035-35042.

Chapter 6

Conclusions and Recommendations

This chapter begins by summarizing the major findings of chapter 4 and chapter 5, followed by a discussion on how the research findings in this thesis could add to the RMB research field. Finally, some suggestions on the possible approach to improve the $Mg(HMDS)_2$*-based electrolyte is shown based on the issues currently exhibited by the electrolyte.*

6.1 Thesis summary

This thesis report began by investigating the compatibility of various magnesium salts against the magnesium metal anode. Two main critical findings are the need for a moisture scavenging agent to allow for reversible magnesium plating in all of the magnesium electrolytes studied and the difference in magnesium salt compatibility for the magnesium plating and stripping process. Amongst $Mg(HMDS)_2$, $Mg(OTF)_2$. $Mg(TFSI)_2$ and $Mg(ClO_4)_2$, $Mg(HMDS)_2$ was found to have the highest compatibility with the magnesium metal anode, followed by $Mg(OTF)_2$, $Mg(TFSI)_{2,}$ and $Mg(ClO_4)_2$. The stability level of each electrolyte determines the magnesium cell lifetime as well as its Coulombic efficiency. Furthermore, the magnesium salt employed determines the magnesium morphology during the electrochemical deposition process. The morphological difference of the magnesium deposit is also a key aspect of electrolyte performance. For example, although $Mg(OTF)_2$-based electrolyte could produce high Coulombic efficiency, the magnesium deposit from the electrolyte is highly porous. Furthermore, dendrite was also found on this deposit. This means that despite having high Coulombic efficiency, the cell lifetime using the $Mg(OTF)_2$-based electrolyte is likely to be short due to the potential formation of an internal short-circuit. On the other hand, $Mg(HMDS)_2$ based electrolytes exhibited high Coulombic efficiency and homogenous magnesium film on the working electrode. The cell lifetime of $Mg(HMDS)_2$-based cells tends to be the longest amongst other electrolytes used. Further, it is also found that to improve the performance of passivating electrolytes ($Mg(OTF)_2$, $Mg(TFSI)_{2,}$ and $Mg(ClO_4)_2$), chloride-based additive needs to be added. However, chloride is found to severely reduce the anodic stability of the electrolyte, even at a very low chloride concentration. Thus, to create a magnesium metal compatible electrolyte using conventional salt, a highly stable magnesium source has to be chosen. $Mg(HMDS)_2$ is the appropriate salt for this purpose. The $Mg(HMDS)_2$-based electrolyte can be optimized by careful selection of solvent, additive concentration, and salt concentration. Chapter 5 shows that the optimized electrolyte is highly compatible with the magnesium anode and enables a dendrite-free magnesium deposition process. Moreover, high compatibility with the CuS cathode has also been established.

The table below provides a comparison of the optimized electrolyte in this study against previously published data. In comparison with the chloride-containing system (No.2-

7), the chloride-free $Mg(HMDS)_2$ electrolyte (No. 1) generally has higher anodic stability on stainless steel and aluminium than these electrolytes. Moreover, the plating and stripping average Coulombic efficiency of the chloride-free $Mg(HMDS)_2$ seems relatively close to the performance of other chloride-free electrolytes (98.6%). However, the anodic stability of the electrolyte is still lower than most chloride-free electrolytes that had been reported (No.11-16). Another deficiency of the electrolyte seems to be its low ionic conductivity.

Table 6.1.1: Benchmark table of the chloride-free $Mg(HMDS)_2$-based electrolyte against other published electrolytes.

No.	Electrolyte	Galvanostatic Overpotential (V)	Coulombic Efficiency (%)	Anodic stability vs. Mg (V)	Ionic conductivity (mS cm^{-1})	Remarks
1	$Mg(HMDS)_2$-$TBABH_4$/DME (this work)	0.25 (0.5mA cm-^{2})	98.3%	**2.7 (SS),** **2.8 (Al),** 1.98 (Pt)	0.32	N.A.
2	$Mg(HMDS)_2$-$AlCl_3$/Diglyme (Ref[1])	< 0.2 (0.5 mA cm^{-2})	99	3.9 (Pt), **2.6 (SS)**	1.7	Corrosive but non-nucleophilic.
3	$Mg(OTF)_2$-$MgCl_2$-$AlCl_3$-Anthracene (Ref[2])	0.1 (0.088 mA cm^{-2})	>95 (0.088 mA cm^2), 98.5 (1 mA cm^{-2})	3.25 (Pt), **2.5 (SS),** **1.85 (Al)**	1.8	
4	$Mg(OTF)_2$-$MgCl_2$-$AlCl_3$ (Ref[3])	0.25 (0.05 mA cm^{-2})	99.1	3 (Pt), **1.75 (SS),** **2.5 (Al)**	N.A.	
5	MBA-$AlCl_3$ (Ref[4])	<0.2 [plate], < 0.1 [strip] (0.088 mA cm^{-2})	>97	2.25 (Pt), **2.35 (Al),** **2.65 (SS)**	0.947	
6	MBA-$MgCl_2$-$AlCl_3$ (Ref[5])	<0.1 (0.088 mA cm^{-2})	98	2.56 (Pt), **1.46 (Al),** **2.1 (SS)**	N.A.	
7	MMAC/DME (Ref[6])	N.A.	100	3.3 (Pt), **2.2 (SS),** **0.8 (Al)**	N.A.	
8	$Mg(CB_{11}H_{12})_2$/G4	0.25 [plate], 0.01 [strip] (1 mA cm^{-2}) (Ref[7])	99 (Ref[8]), 97 (Ref[7])	3.8-4.0 V (Al, SS, Pt) (Ref[8])	1.8	Complicated synthesis procedure.
9	$Mg(B(HFIP)_4)_2$ (Ref[9])	<0.2 (0.5 mA cm-^{2})	>98	3.5 (Pt), **4.3 (SS, Al)**	11 (Ref[10])	Commercially unavailable.
10	$Mg(B(PFPINA)_2)_2$ (Ref[11])	0.09 (1 mA cm^{-2})	95	**4.0 (SS, Al)**	3.95	
11	THFPB+MgF_2 (Ref[12])	N.A.	99.8	**>3.5 (SS),** **3.8 (Al)**	1.1	N.A.
12	THFPB+MgO (Ref[13])	<0.1 (0.05 mA cm^{-2})	N.A.	**>4.0 (SS),** **4.2 (Al)**	0.174	N.A.
13	THFPB+$Mg(BH_4)_2$ (Ref[14])		99	**2.8 (SS),** **1.6 (Al)**	3.72	N.A.

6.2 Research implication

The findings of this thesis indicate that contrary to common assumptions, some conventional chloride-free magnesium sources may be compatible with the magnesium metal anode. Consequently, the findings of this thesis suggest an alternative pathway for the future of magnesium electrolyte development. As discussed in chapter 2, a common electrolyte development pathway currently pursued is to generate new boron-based electrolytes. The practicality of the industrial production of this salt remains unclear and needs to be investigated before being applied for commercial battery application. Hence, electrolyte development by using novel magnesium salts is challenging due to the need for performance optimization and electrolyte production consideration. The development of conventional magnesium salt-based electrolytes may be more fruitful as the industrial-scale production method of the electrolyte is well established.

Furthermore, the thesis highlights the potential benefit of a chloride-free approach to improving the magnesium plating and stripping electrochemistry in less studied magnesium salts such as magnesium amides[4, 5] and magnesium alkoxides/phenoxides[15-17]. As shown in this thesis, the primary hindrance in establishing good magnesium plating and stripping reversibility could be the passivating effect of moisture and contaminants in the electrolyte. The addition of chloride-based additive is well known to suppress the passivating effect of moisture.[18] Nevertheless, this common strategy, as discussed in §2, will cause corrosion on Aluminum and stainless-steel current collectors. An alternative method such as utilizing moisture scavenger has been used previously. However, due to the passivating nature of the magnesium salt used [i.e. $Mg(TFSI)_2$] in combination with the moisture scavenger, the electrolytes' performance shown in the studies tends to be poor. Nevertheless, certain classes of commercial magnesium salts such as magnesium alkoxides, phenoxides, or amides had not been explored through this approach.

6.3 Suggestions for future works

Several drawbacks of the $Mg(HMDS)_2$-based electrolyte (0.2 M $Mg(HDMS)_2$ +20 mM $TBABH_4$ in DME) are as follows:

- (1) Low electrolyte ionic conductivity. The ionic conductivity of the optimized electrolyte is 0.32 mS cm^{-1}. This value is far below the ionic conductivity of common lithium battery electrolytes which is within the range of 3 to 11 mS cm^{-1}.[19] With the current need for fast-charging batteries for electric vehicles, the need to improve the electrolyte's ionic conductivity becomes more crucial.[20]
- (2) Low thermal stability of DME. As only DME is known to be suitable for Mg(HMDS)$_2$-based electrolytes, the electrolyte is likely to have poor thermal stability. This is because DME solvent is known to have a low boiling point (85°C) and an even lower flash point (-6°C).[21]
- (3) The use of TBABH$_4$ is likely to contribute to battery overcharging. Although it has been shown that the anodic stability of the electrolyte is relatively high on aluminum and stainless-steel current collectors (2.8 V on aluminium and 2.7 V on stainless steel). Overcharging is still observed in the full cell cycling process. This could be due to the high surface area of the cathode, which further exacerbates electrolyte decomposition, or due to reduced decomposition onset potential of BH$_4^-$ on conductive carbon or active material in the cathode.
- (4) Lack of cathode material suitable with the Mg(HMDS)$_2$-based electrolyte. As shown in chapter 5, various magnesium battery cathodes such as Mo$_6$S$_8$ and Sulfur exhibited low discharge capacity when used with the Mg(HMDS)$_2$-based electrolyte. The low discharge capacity of the Mg//S cell is particularly troubling as the sulfur cathode has a high theoretical capacity and has been the primary cathode of interest in the development of a high-energy-density magnesium battery.

To overcome these issues, various research work is suggested, such as:

- Given problems (1) and (2), the addition of ionic liquid solvent as part of the Mg(HMDS)$_2$-based electrolyte is worth exploring. Ionic liquid tends to have high ionic conductivity and high thermal stability. As magnesium plating and stripping process from the Mg(HMDS)$_2$ complex seems to be conducive from DME, the initial work could begin by mixing various ionic liquids with DME at various ratios.
- Issue (3) may potentially be resolved by extending the anodic stability of the moisture scavenger species in the electrolyte. A previous report by Hebie *et al.* shows that the anodic stability of BH$_4^-$ can be further improved by substituting

some of the hydride groups with phenol to create $B(OPh)_3H^-$ species[22]. Alternatively, as shown in chapter 5, the addition of graphene oxide on the separator seems to reduce the overcharging effect in the electrolyte. Additional future works can also seek to optimize the amount of graphene oxide inside the cell to prevent the overcharging effect from occurring.

- Lastly, the low discharge capacity of the sulfur cathode in the electrolyte (issue 4) may indicate low reaction kinetic between the $Mg(HMDS)_2.DME$ complex and the sulfur cathode (S-PAN or short-chain sulfur species). To increase the reaction rate, catalytic material known to improve the reaction rate of sulfur cathodes may be investigated in combination with the electrolyte. Materials such as TiS_2[23], sulfurized cobalt[24] are known to improve the redox reaction of the sulfur cathode in rechargeable magnesium batteries.

References

1. Zhao-Karger, Z.; Zhao, X.; Fuhr, O.; Fichtner, M., Bisamide Based Non-Nucleophilic Electrolytes for Rechargeable Magnesium Batteries. *RSC Adv.* **2013,** *3*, 16330-16335.

2. Yang, Y.; Wang, W.; Nuli, Y.; Yang, J.; Wang, J., High Active Magnesium Trifluoromethanesulfonate-Based Electrolytes for Magnesium–Sulfur Batteries. *ACS Appl. Mater. Interfaces* **2019,** *11*, 9062-9072.

3. Huang, D.; Tan, S.; Li, M.; Wang, D.; Han, C.; An, Q.; Mai, L., Highly Efficient Non-Nucleophilic $Mg(CF_3SO_3)_2$-Based Electrolyte for High-Power Mg/S Battery. *ACS Appl. Mater. Interfaces* **2020,** *12*, 17474-17480.

4. Zhao, X.; Yang, Y.; NuLi, Y.; Li, D.; Wang, Y.; Xiang, X., A new class of electrolytes based on magnesium bis(diisopropyl)amide for magnesium–sulfur batteries. *Chem. Commun.* **2019,** *55*, 6086-6089.

5. Yang, Y.; Qiu, Y.; NuLi, Y.; Wang, W.; Yang, J.; Wang, J., A novel magnesium electrolyte containing a magnesium bis(diisopropyl)amide–magnesium chloride complex for rechargeable magnesium batteries. *J. Mater. Chem. A* **2019,** *7*, 18295-18303.

6. Luo, J.; He, S.; Liu, T. L., Tertiary Mg/MgCl2/AlCl3 Inorganic Mg2+ Electrolytes with Unprecedented Electrochemical Performance for Reversible Mg Deposition. *ACS Energy Lett.* **2017,** *2*, 1197-1202.

7. Jay, R.; Tomich, A. W.; Zhang, J.; Zhao, Y.; De Gorostiza, A.; Lavallo, V.; Guo, J., Comparative Study of Mg(CB11H12)2 and Mg(TFSI)2 at the Magnesium/Electrolyte Interface. *ACS Appl. Mater. Interfaces* **2019,** *11*, 11414-11420.

8. Tutusaus, O.; Mohtadi, R.; Arthur, T. S.; Mizuno, F.; Nelson, E. G.; Sevryugina, Y. V., An Efficient Halogen-Free Electrolyte for Use in Rechargeable Magnesium Batteries. *Angew. Chem. Int. Ed.* **2015,** *54*, 7900-7904.

9. Zhao-Karger, Z.; Gil Bardaji, M. E.; Fuhr, O.; Fichtner, M., A New Class of Non-Corrosive, Highly Efficient Electrolytes for Rechargeable Magnesium Batteries. *J. Mater. Chem. A* **2017,** *5*, 10815-10820.

10. Zhao-Karger, Z.; Liu, R.; Dai, W.; Li, Z.; Diemant, T.; Vinayan, B. P.; Bonatto Minella, C.; Yu, X.; Manthiram, A.; Behm, R. J.; Ruben, M.; Fichtner, M., Toward Highly Reversible Magnesium–Sulfur Batteries with Efficient and Practical $Mg[B(hfip)_4]_2$ Electrolyte. *ACS Energy Lett.* **2018,** *3*, 2005-2013.

11. Luo, J.; Bi, Y.; Zhang, L.; Zhang, X.; Liu, T. L., A Stable, Non-Corrosive Perfluorinated Pinacolatoborate Mg Electrolyte for Rechargeable Mg Batteries. *Angew. Chem. Int. Ed.* **2019,** *58*, 6967-6971.

12. Zhang, Z.; Cui, Z.; Qiao, L.; Guan, J.; Xu, H.; Wang, X.; Hu, P.; Du, H.; Li, S.; Zhou, X.; Dong, S.; Liu, Z.; Cui, G.; Chen, L., Novel Design Concepts of Efficient Mg-Ion Electrolytes toward High-Performance Magnesium–Selenium and Magnesium–Sulfur Batteries. *Adv. Energy Mater.* **2017,** *7*, 1602055.

13. Xu, H.; Zhang, Z.; Cui, Z.; Du, A.; Lu, C.; Dong, S.; Ma, J.; Zhou, X.; Cui, G., Strong anion receptor-assisted boron-based Mg electrolyte with wide electrochemical window and non-nucleophilic characteristic. *Electrochem. Commun.* **2017,** *83*, 72-76.

14. Xu, H.; Zhang, Z.; Li, J.; Qiao, L.; Lu, C.; Tang, K.; Dong, S.; Ma, J.; Liu, Y.; Zhou, X.; Cui, G., Multifunctional Additives Improve the Electrolyte Properties of Magnesium Borohydride Toward Magnesium–Sulfur Batteries. *ACS Appl. Mater. Interfaces* **2018,** *10*, 23757-23765.

15. Herb, J. T.; Nist-Lund, C. A.; Arnold, C. B., A fluorinated dialkoxide-based magnesium-ion electrolyte. *J. Mater. Chem. A* **2017,** *5*, 7801-7805.

16. Nist-Lund, C. A.; Herb, J. T.; Arnold, C. B., Improving halide-containing magnesium-ion electrolyte performance via sterically hindered alkoxide ligands. *J. Power Sources* **2017,** *362*, 308-314.

17. Kim, I.-T.; Yamabuki, K.; Sumimoto, M.; Tsutsumi, H.; Morita, M.; Yoshimoto, N., Characteristics of tetrahydrofuran-based electrolytes with magnesium alkoxide additives for rechargeable magnesium batteries. *J. Power Sources* **2016,** *323*, 51-56.

18. Connell, J. G.; Genorio, B.; Lopes, P. P.; Strmcnik, D.; Stamenkovic, V. R.; Markovic, N. M., Tuning the Reversibility of Mg Anodes via Controlled Surface Passivation by H_2O/Cl^- in Organic Electrolytes. *Chem. Mater.* **2016,** *28*, 8268-8277.

19. Xu, K., Nonaqueous Liquid Electrolytes for Lithium-Based Rechargeable Batteries. *Chem. Rev.* **2004,** *104*, 4303-4418.

20. Logan, E. R.; Dahn, J. R., Electrolyte Design for Fast-Charging Li-Ion Batteries. *Trends Chem.* **2020,** *2*, 354-366.

21. Tang, S.; Zhao, H., Glymes as versatile solvents for chemical reactions and processes: from the laboratory to industry. *RSC Adv.* **2014,** *4*, 11251-11287.

22. Hebié, S.; Ngo, H. P. K.; Leprêtre, J.-C.; Iojoiu, C.; Cointeaux, L.; Berthelot, R.; Alloin, F., Electrolyte Based on Easily Synthesized, Low Cost Triphenolate–Borohydride Salt for High Performance Mg(TFSI)2-Glyme Rechargeable Magnesium Batteries. *ACS Appl. Mater. Interfaces* **2017,** *9*, 28377-28385.

23. Xu, Y.; Ye, Y.; Zhao, S.; Feng, J.; Li, J.; Chen, H.; Yang, A.; Shi, F.; Jia, L.; Wu, Y.; Yu, X.; Glans-Suzuki, P.-A.; Cui, Y.; Guo, J.; Zhang, Y., In Situ X-ray Absorption Spectroscopic Investigation of the Capacity Degradation Mechanism in Mg/S Batteries. *Nano Lett.* **2019,** *19*, 2928-2934.

24. Sun, J.; Deng, C.; Bi, Y.; Wu, K.-H.; Zhu, S.; Xie, Z.; Li, C.; Amal, R.; Luo, J.; Liu, T.; Wang, D.-W., In Situ Sulfurized Carbon-Confined Cobalt for Long-Life Mg/S Batteries. *ACS Appl. Energy Mater.* **2020,** *3*, 2516-2525.

APPENDIX

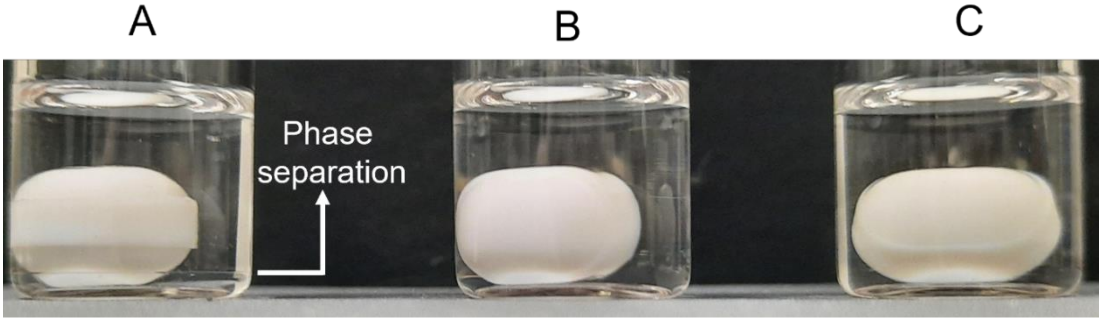

Figure A 1: Visual image of 0.1 M $Mg(TFSI)_2$ in DME. (a), 0.1 M $Mg(TFSI)_2$ + 30 mM TBAOTf in DME (b), and 0.1 M $Mg(TFSI)_2$ + 30 mM TBACl in DME (c). The white oval substance in each vial is a stir bar.

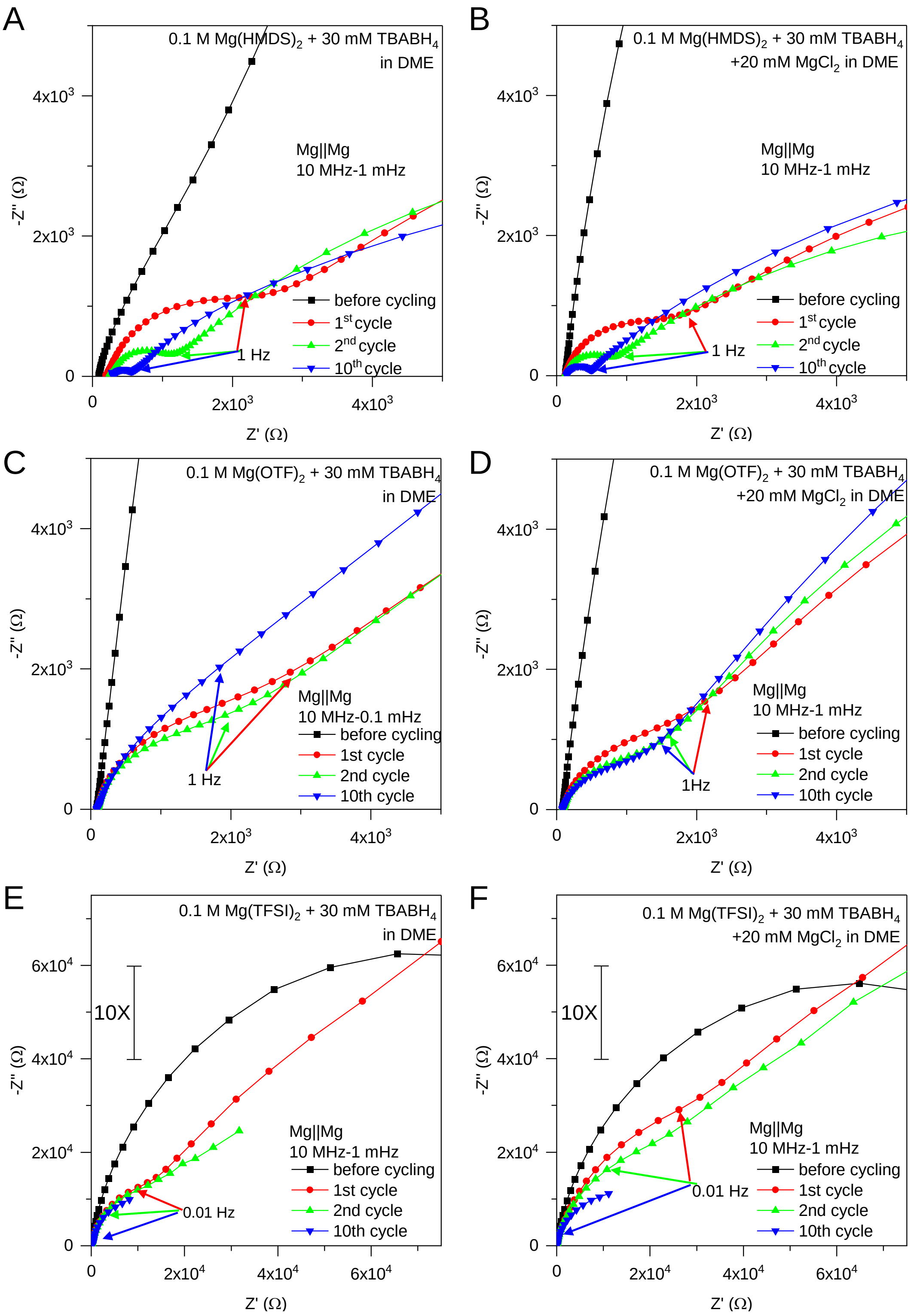

Figure A 2: Nyquist plots of Mg//Mg cells with various electrolytes. (a and b) Mg anode cycled in 0.1 M Mg(HMDS)$_2$ + 30 mM TBABH$_4$ without (a) and with (b) 20 mM of MgCl$_2$. (c and d) Mg anode cycled in 0.1 M Mg(OTf)$_2$ + 30 mM TBABH$_4$ without (c) and with (d) 20 mM of $MgCl_2$. (e and f) Mg anode cycled in 0.1 M $Mg(TFSI)_2$ + 30 mM $TBABH_4$ without (e) and with (f) 20 mM of $MgCl_2$.

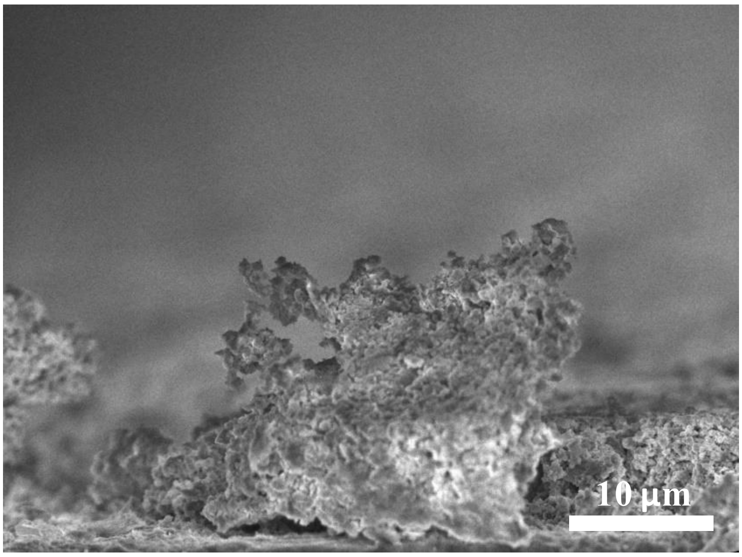

Figure A 3: Evidence of dendritic magnesium, grown from 0.1 M $Mg(OTF)_2$ + 30 mM $TBABH_4$ in DME. Magnesium is deposited on aluminum at 0.5 mA cm^{-2}.

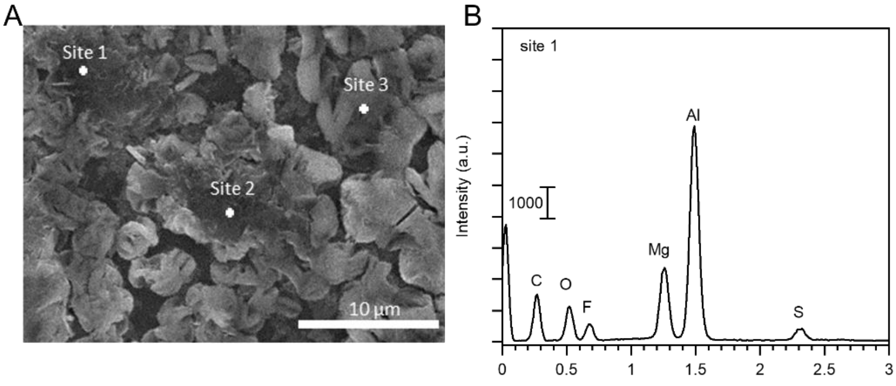

C

Site 1	% wt.	Site 2	% wt.	Site 3	% wt.
Mg	8.11	Mg	3.30	Mg	21.56
C	41.35	C	54.72	C	6.16
O	14.52	O	9.64	O	21.79
N	1.39	N	0.86	N	0.81
F	5.77	F	4.19	F	5.53
S	2.17	S	1.39	S	2.94
Al	26.69	Al	25.90	Al	41.21

Figure A 4: Electrochemically deposited substance from 0.1 M $Mg(TFSI)_2$ + 30 mM $TBABH_4$ in DME with low Magnesium content. (a) SEM image of the deposit. (b) EDX spectrum of the deposit. (c) EDX quantitative analysis of the deposits.

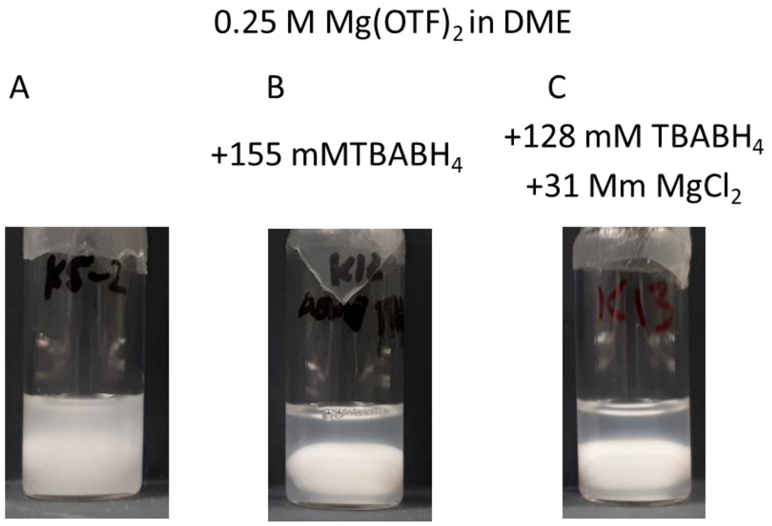

Figure A 5: Visual image of 0.25 M $Mg(OTF)_2$ solubility in DME with the addition of $TBABH_4$. The white oval substance in each vial is a stir bar.

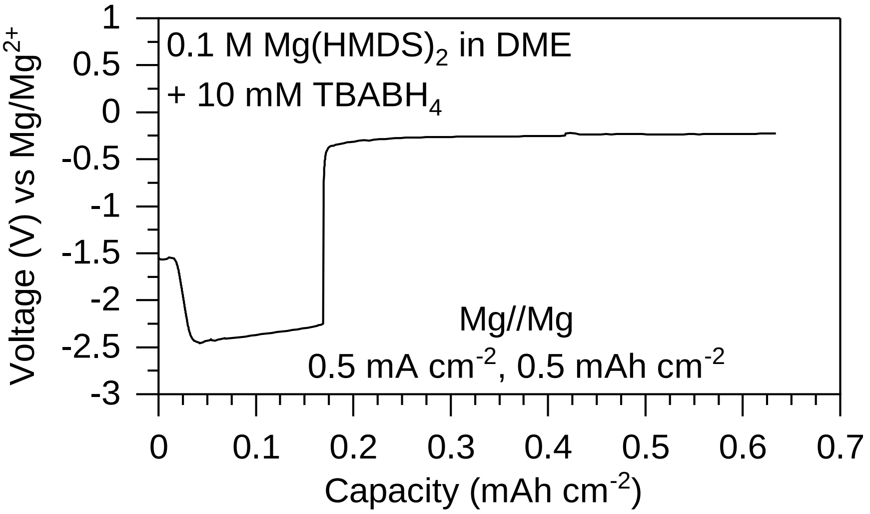

Figure A 6: Cell short-circuit in 0.1 M $Mg(HMDS)_2$ + 10 mM $TBABH_4$ in DME.

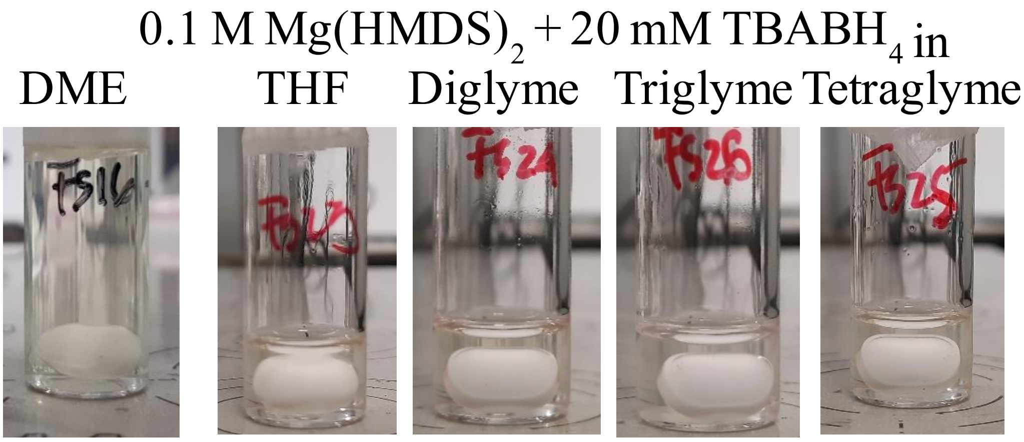

Figure A 7: Visual image of various Mg(HMDS)$_2$-based in various solvents.

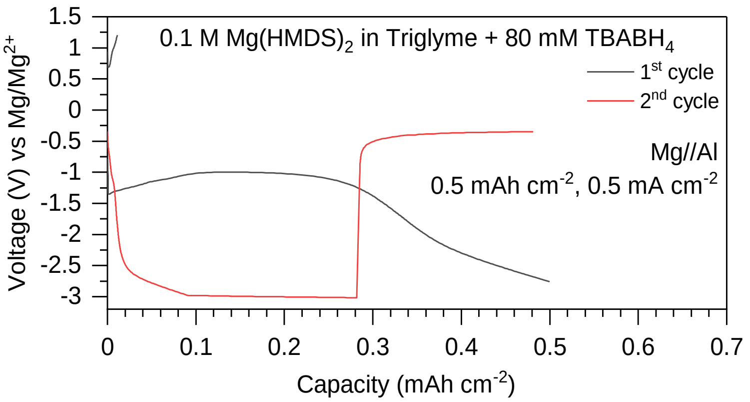

Figure A 8: Magnesium plating and stripping process with 0.1 M Mg(HMDS)$_2$ + 80 mM TBABH$_4$ in Triglyme on carbon-coated aluminium (0.5 mA cm^{-2} and 0.5 mAh cm^{-2}).

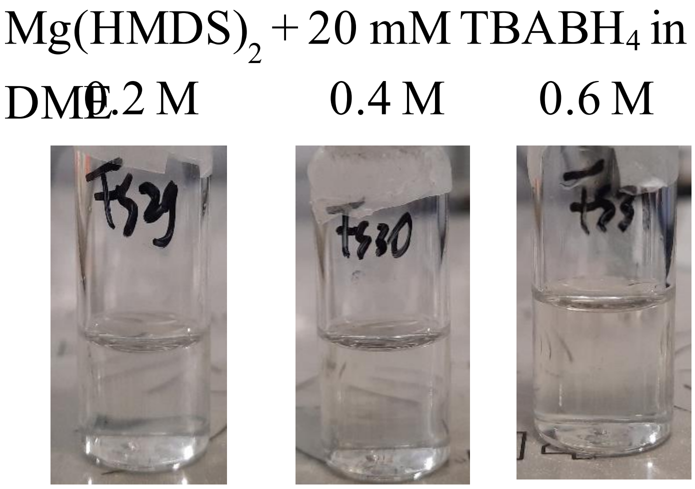

Figure A 9: Visual image of Mg(HMDS)$_2$-based electrolyte in DME (0.2 to 0.6 M).

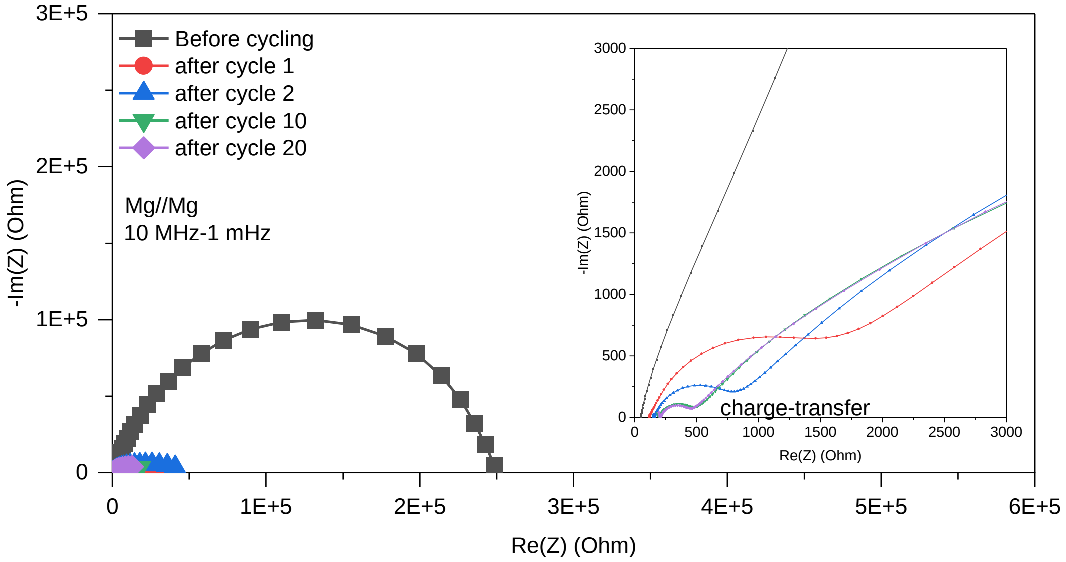

Figure A 10: Nyquist plot of Mg//Mg symmetric cell with 0.2 M Mg(HMDS)$_2$ + 20 mM TBABH$_4$/DME electrolyte. The cell is cycled by plating and stripping the working electrode at 0.5 mA cm^{-2} for 1 hour each.

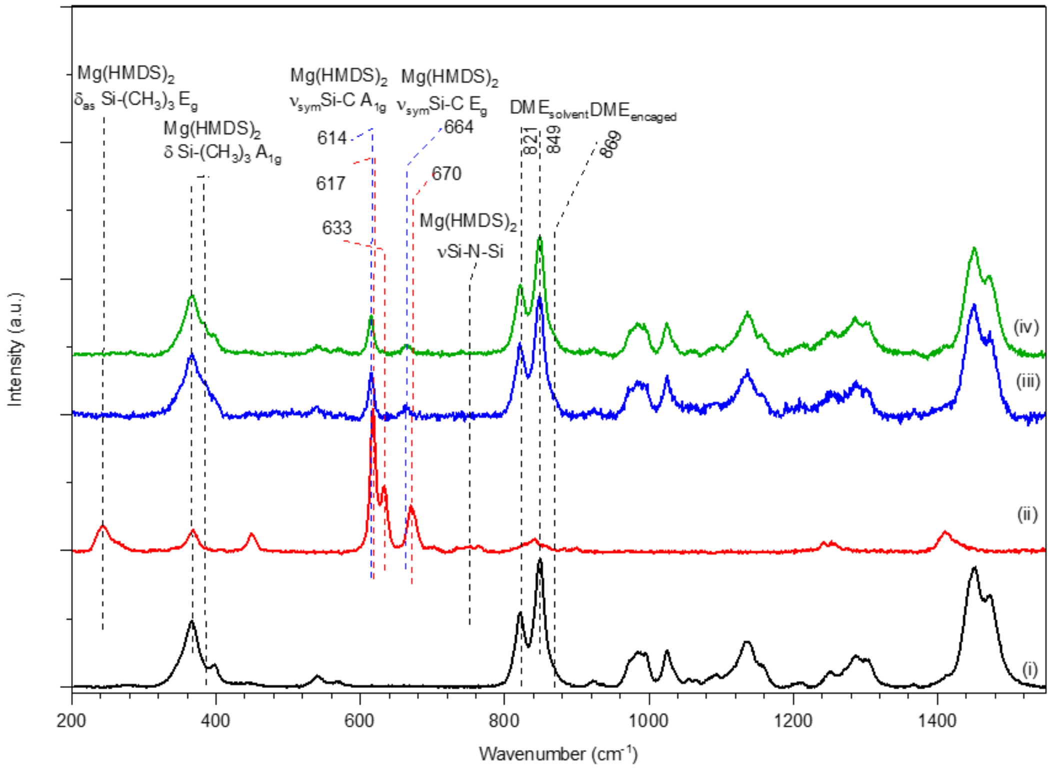

Figure A 11: Raman spectroscopy of DME based electrolyte. (i) DME solvent (ii) Mg(HMDS)$_2$ powder (iii) 0.1 M Mg(HMDS)$_2$ in DME (iv) 0.1 M Mg(HMDS)$_2$ + 20 mM TBABH$_4$ in DME.

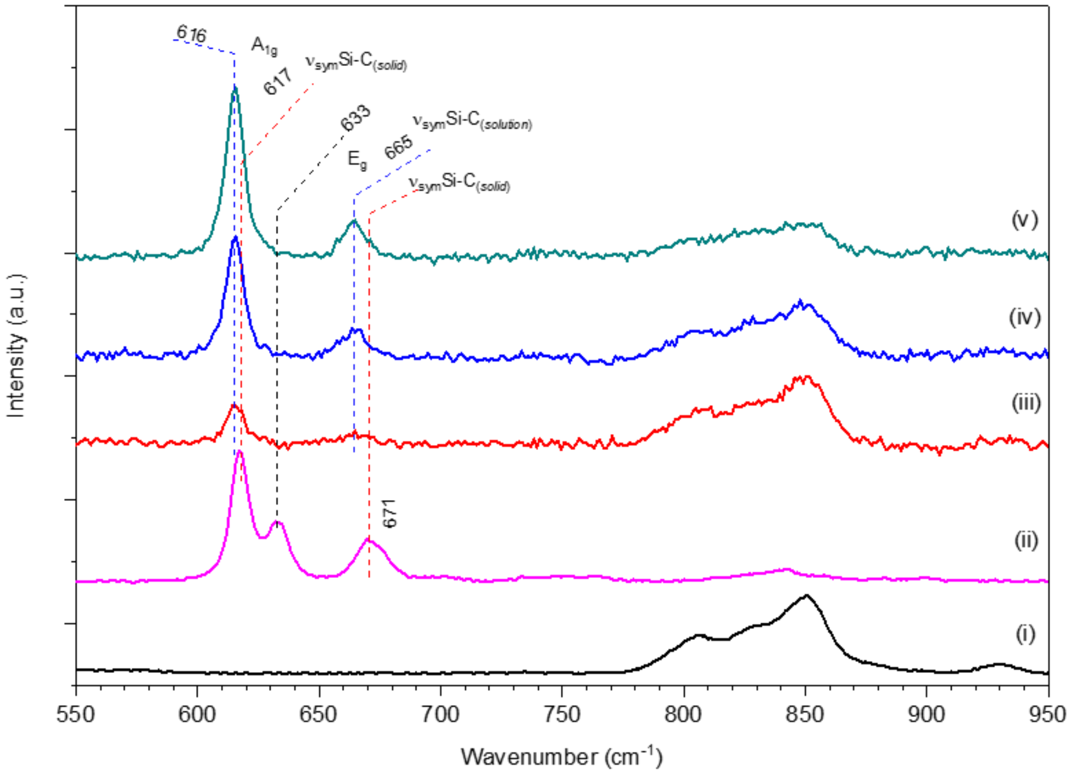

Figure A 12: Raman spectroscopy of Triglyme based electrolyte. (i) Triglyme solvent (ii) $Mg(HMDS)_2$ powder (iii) 0.1 M $Mg(HMDS)_2$ in Triglyme (iv) 0.4 M $Mg(HMDS)_2$ in Triglyme (v) 1 M $Mg(HMDS)_2$ in Triglyme.

Table A 1: Crystallographic data of $Mg(HMDS)_2$.DME complex

Chemical formula	$C_{16}H_{46}MgN_2O_2Si_4$	
Formula weight	435.22 g/mol	
Temperature	100(2) K	
X-ray Wavelength	1.54178 Å	
Crystal size	0.020 x 0.240 x 0.280 mm	
Crystal habit	colorless plate	
Crystal system	monoclinic	
Space group	P 1 21/c 1	
Unit cell dimensions	a = 8.3270(5) Å	α = 90°
	b = 34.141(2) Å	β = 100.373(4)°

	c = 19.6183(13) Å	γ = 90°
Volume	5486.2(6) Å^3	
Z	8	
Density (calculated)	1.054 g/cm^3	
Absorption coefficient	2.320 mm^{-1}	
F(000)	1920	
Total Reflection	34497	
Independent reflection	9668 (R_{int} = 5.97%, R_{sig} = 5.69%)	
Maximum angle	66.8°	

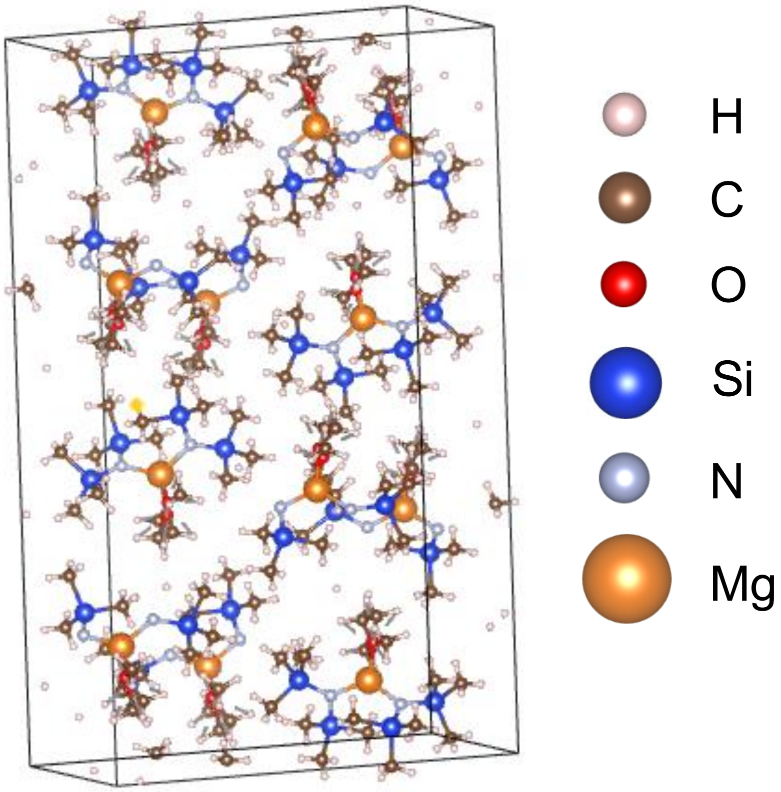

Figure A 13: Crystal unit structure of Mg(HMDS)$_2$.DME.

Table A 2: Ionic conductivity of various Mg(HMDS)$_2$-based electrolytes.

Electrolyte	**Ionic conductivity (mS cm^{-1})**	**Temperature (°C)**
0.2 M Mg(HMDS)$_2$ +20 mM TBABH$_4$/DME	0.32	24.7
0.1 M Mg(HMDS)$_2$ +20 mM TBABH$_4$/DME	0.26	25.2
0.1 M Mg(HMDS)$_2$ +30 mM TBABH$_4$ /DME	0.42	25.4
0.1 M Mg(HMDS)$_2$ /DME	0.0063	25.5

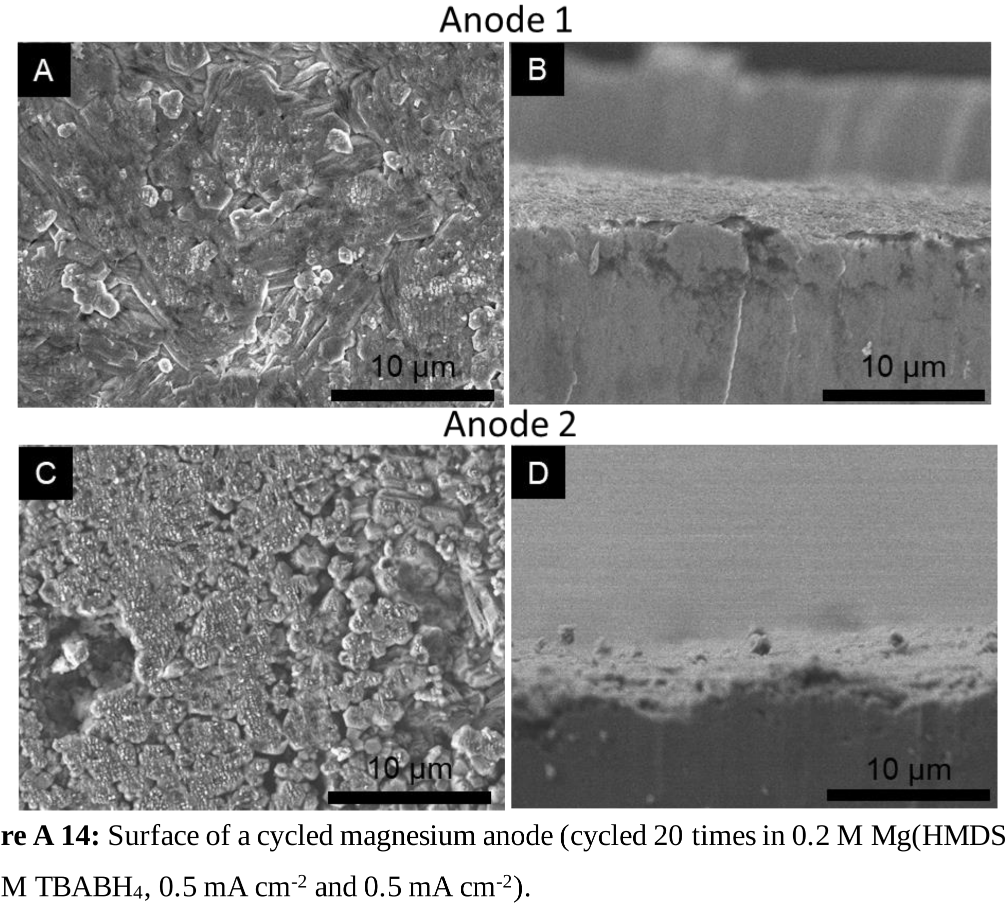

Figure A 14: Surface of a cycled magnesium anode (cycled 20 times in 0.2 M Mg(HMDS)$_2$ + 20 mM TBABH$_4$, 0.5 mA cm^{-2} and 0.5 mA cm^{-2}).

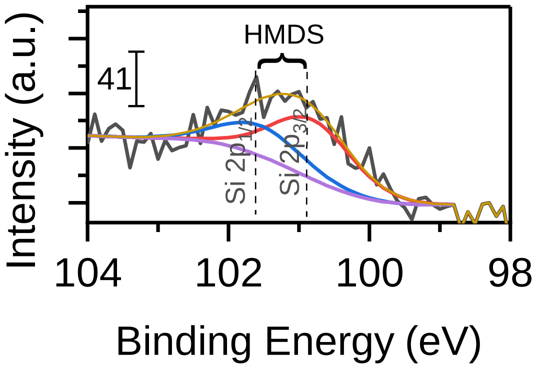

Figure A 15: Si 2p XPS analysis of drop casted Mg(HMDS)$_2$ powder.

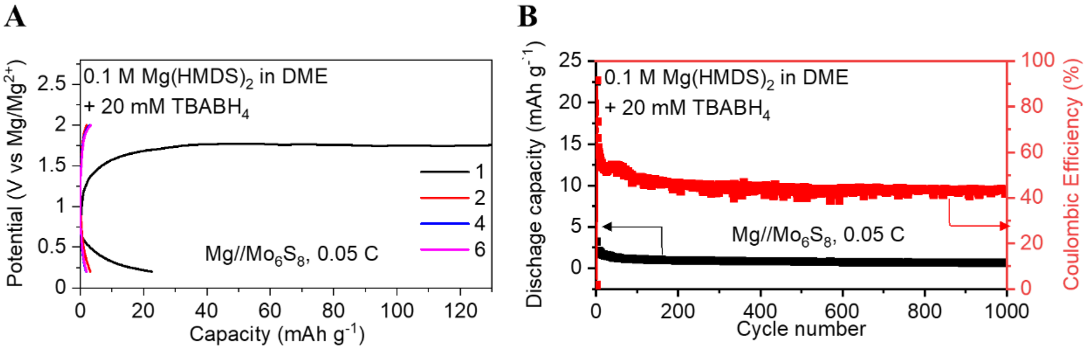

Figure A 16: Full cell cycling of Mg//Mo$_6$S$_8$ cell at room temperature using 0.1 M Mg(HMDS)$_2$ in DME. The cathode was coated on stainless steel foil.

Mg//CuS replication Cell 1

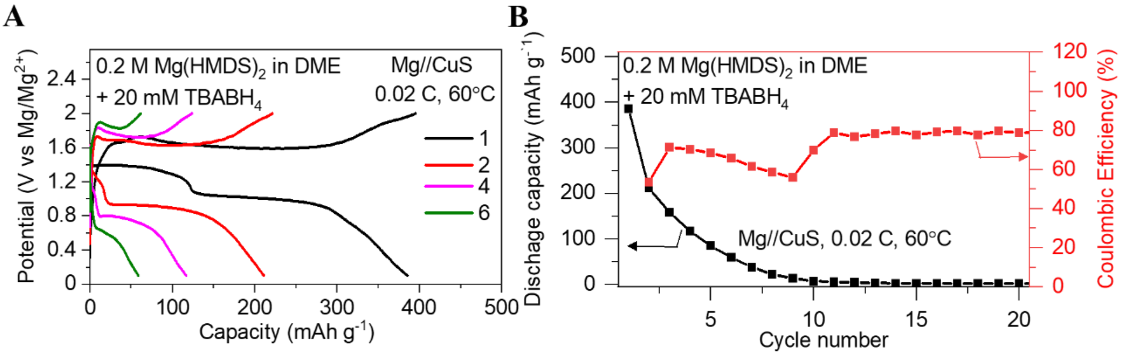

Mg//CuS replication Cell 2

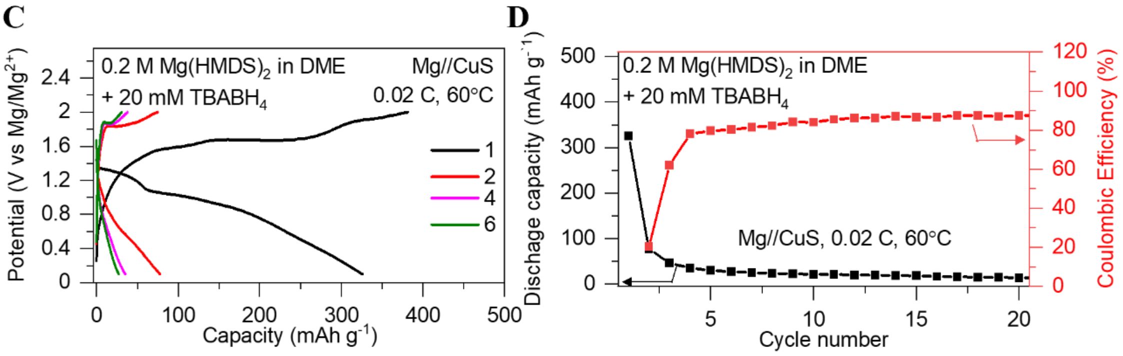

Figure A 17: Full cell cycling of Mg//CuS cells with graphene-oxide coated separator. CuS cathode coated on carbon-coated aluminium.

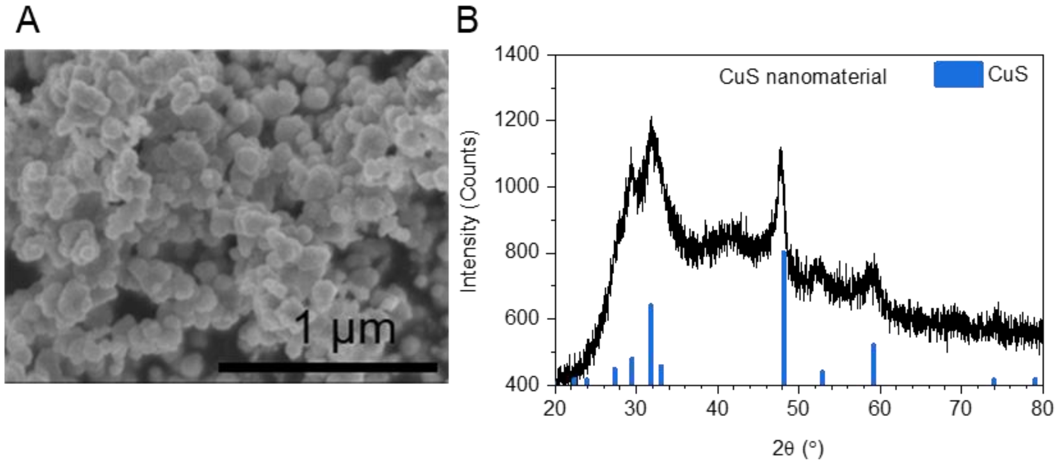

Figure A 18: CuS nanomaterial morphology and XRD spectrum.

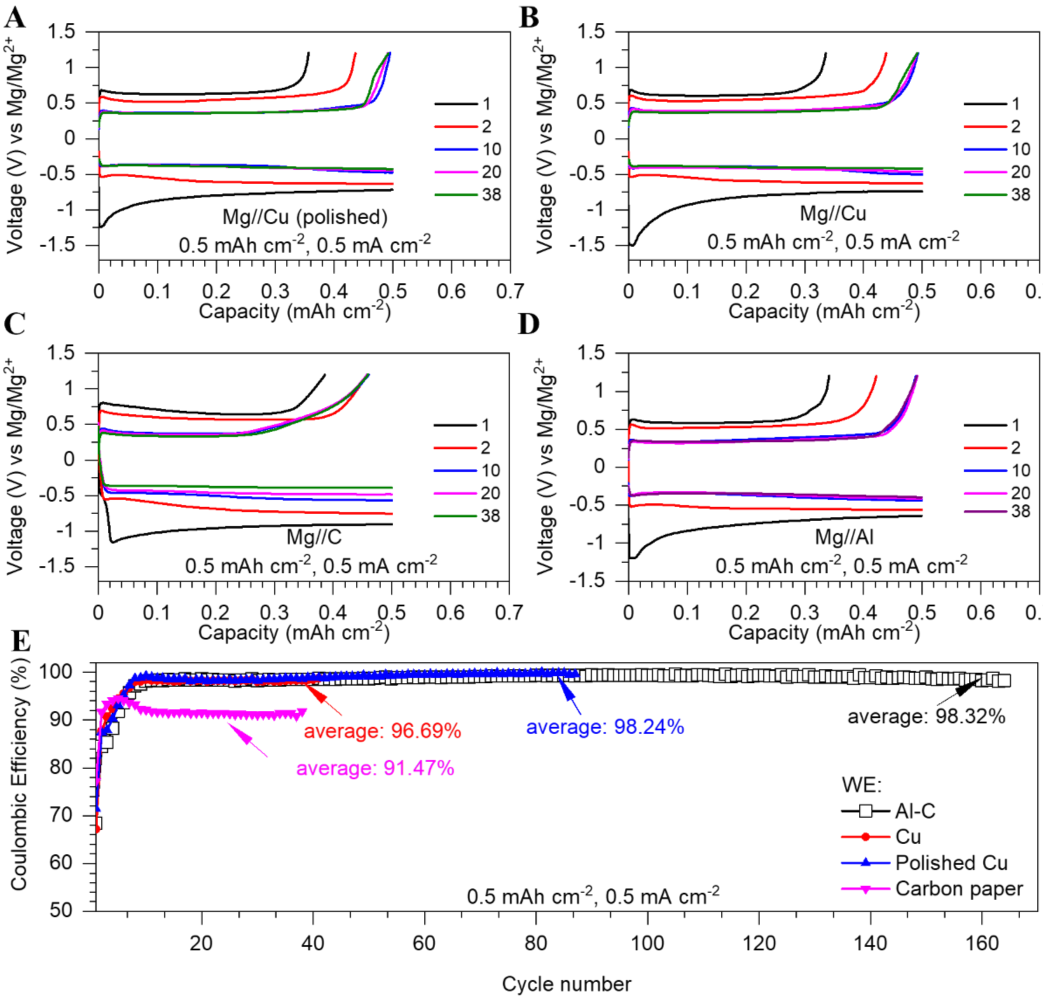

Figure A 19: Magnesium plating and stripping behavior on various working electrodes. (a) Polished copper electrode, (b) unpolished copper, (c) carbon paper, (d) carbon-coated aluminium. Electrolyte: 0.2 M Mg(HMDS)$_2$ + 20 mM TBABH$_4$ in DME.